Numerical investigation on the effect of gravitational orientation on bubble growth during flow boiling in a high aspect ratio microchannel

by

Jarryd Potgieter

Submitted in partial fulfilment of the requirements for the degree

Master's in Mechanical Engineering

in the

Department of Mechanical and Aeronautical Engineering

Faculty of Engineering, Built Environment and Information Technology

UNIVERSITY OF PRETORIA

Supervisor: Dr Mohammad Moghimi Ardekani

Co-supervisors: Prof Josua Meyer and Dr Prashant Valluri

2019

Abstract

Numerical investigation on the effect of gravitational orientation on bubble growth during flow boiling in a high aspect ratio microchannel

by

Jarryd Potgieter

Supervisor: Dr MA Moghimi

Co-supervisors: Prof JP Meyer and Dr P Valluri

Department: Mechanical and Aeronautical Engineering

University: University of Pretoria

Degree: Master's in Mechanical Engineering

Keywords: Microchannel, flow boiling, bubble growth, high aspect ratio, computational fluid dynamics, Ansys Fluent, mass transfer, adaptive mesh refinement

Recent technological developments, mostly in the fields of concentrated solar power and microelectronics, have driven heat transfer requirements higher than current heat exchangers are capable of producing. Processing power is increasing, while processor size simultaneously decreases and the heat flux requirements of concentrating solar power plants are being driven up by the high temperatures that produce the best thermal efficiency. Heat transfer in microchannels, specifically when utilising flow boiling, has been shown to produce significantly higher heat fluxes than their macro-scale counterparts and could have a large impact on many industrial fields. This high heat transfer characteristic is caused by a number of factors, including the large difference between the sensible and latent heat of the working fluid and the evaporation of a thin liquid film that forms between the microchannel walls and the vapour bubbles. These phenomena occur at incredibly small scales. Flow visualisations, temperature and pressure measurements are therefore difficult to obtain.

Many experiments that cover a wide range of microchannel sizes, shapes and orientations, and utilise different working fluids and heat fluxes have been reported. However, the correlations between confined boiling, heat flux and pressure drop have mostly been produced for macro-scale flow. Many different criteria have been developed to distinguish the macro scale from the micro scale, but the general consensus is that macro-scale heat transfer correlations do not perform well when used in the

micro scale. Heat transfer correlations are typically created by performing physical experiments over a wide range of parameters and then quantifying the effect that varying these parameters has on the performance of the system. The small scale and high complexity of microchannel-based heat exchangers make visualising the flow within them difficult and inaccurate because both the working fluid and the microchannel walls distort light. The use of numerical modelling via computational fluid dynamics software allows phenomena that occur within the channel to be simulated, which provides valuable insight into how rapid bubble growth affects the surrounding fluid, which can lead to the design of better heat exchangers.

This study focused on numerically modelling the growth of a single bubble during the flow boiling of FC-72 in a microchannel with a hydraulic diameter of 0.9 mm and an aspect ratio of 10. The numerical domain was limited to a 10 mm section of the microchannel where bubble nucleation and detachment were observed in an experimental study on a similar microchannel setup. The high cost of 3D simulations was offset by an interface-tracking mesh refinement method, which refined cells not only at the interface, but also a set distance on either side of the interface. To focus on the effects of gravity, a simplified approach is used, which isolates certain phenomena. Density gradients, material roughness and multiple bubble interaction are ignored so that the effects of buoyancy and bubble detachment can be analysed. Simulations are first performed in a 2D section through the centre of the microchannel, and then in the full 3D domain.

In both the 3D numerical and experimental cases (Meyer et al., 2020), the bottom heated case had the lowest maximum temperature and the highest heat transfer characteristics, which were influenced by the detachment of the bubble from the heated surface. This observation indicates that the gravitational orientation of the channel can have a significant effect on the heat transfer characteristics of microchannel-based heat exchangers, and that more investigation is required to characterise the extent of this effect.

Acknowledgments

Contents

List of figures

List of tables

Nomenclature

Symbols

A	Area (m^2)
c_p	Specific heat capacity (J/kg.K)
C	Nusselt number correlation constant
d	Derivative
D	Diameter (m)
D_m	Material derivative
e	Error
f	Adaption metric
F_s	GCI constant
g	Gravitational acceleration (m/s^2)
G	Mass flow rate (kg/s)
h	Heat transfer coefficient (W/m^2.K)
h_L	Latent heat capacity (J/kg)
k	Conductivity (W/m.K)
L	Length (m)
m	Mass (kg)
$\dot{m}$	Mass transfer rate (kg/m^3.s)
m_n	Nusselt number correlation constant
n	Nusselt number correlation constant
N	Normalisation factor
p	GCI value
P	Pressure (Pa)
P_r	Perimeter (m)
$\dot{q}$	Heat flux (W/m^2)
Q	Heat (J)
$\dot{Q}$	Heat flow rate (W)
r	Radius (m)
r_f	Element size ratio
r_g	Gradient volume weight
R	Resistance (K/W)
R_g	Gas constant (J/kg.mol)
S_E	Energy generation source term

S_g	Vapour mass source term (kg/m^3.s)
S_L	Liquid mass source term (kg/m^3.s)
T	Temperature (K)
t	Time (s)
v	Kinematic viscosity (m^2/s)
V	Velocity (m/s)
x	Quality

Greek symbols

α	Volume fraction
γ	Mass transfer coefficient
δ_t	Film thickness (m)
$\varDelta$	Change in property
ε	Emissivity (W/m^2)
θ	Contact angle (^{0})
μ	Dynamic viscosity (kg/m.s)
v	Kinematic viscosity (m^2/s)
π	Pi
ρ	Density (kg/m^3)
$\dot{\rho}$	Mass transfer source term (kg/m^3.s)
σ	Surface tension (N/m)
σ_s	Stephan-Boltzmann constant (W/m^2.K^4)
ω	Mass transfer coefficient
∂	Partial derivative
Ø	Scalar

Subscripts

a	Acceleration
c	Entrance contraction
cr	Critical
e	Expansion
f	Fluid
$f,1\text{-}ph$	Single-phase frictional pressure drop
f,tp	Two-phase frictional pressure drop
g	Gravitational
h	Hydraulic
H	Heated

i	Inlet
L	Liquid
m	Multiphase
o	Outlet
s	Surface
sat	Saturation
t	Liquid layer thickness
th	Thermal
to	Total
tr	Threshold
v	Vapour
w	Wall
0	Initial
1	Smeared
∞	Ambient

Superscripts

~	Vector
-	Two-fluid property

Abbreviations

CFD	Computational fluid dynamics
CFL	Courant-Friedrichs Lewy number
CHE	Compact heat exchanger
CHF	Critical heat flux
CSP	Concentrated solar power
DNI	Direct normal irradiance
GCI	Grid Convergence Index
HTC	Heat transfer coefficient
HTF	Heat transfer fluid
PISO	Pressure-Implicit with Splitting of Operators
PRESTO!	PREssure STaggered Option
PV	Photovoltaic
UDF	User-defined function
VOF	Volume of fluid

Dimensionless terms

Bo	Bond number
Ca	Capillary number
Co	Confinement number
Eö	Eotwös number
Nu	Nusselt number
Pr	Prandtl number
Re	Reynolds number
We	Weber number

1. Introduction

1.1. Background

Since the Industrial Revolution, a significant amount of human progress has occurred in a variety of fields, ranging from medicine to renewable energy. Buildings have become larger, cars faster and electronics have shrunk to a fraction of their original size. Most of this progress has happened because of the many ways that have been developed to produce, control and consume large amounts of energy.

The majority of the world's energy usage still comes from fossil fuels, which are usually converted to electrical energy in a power plant or converted to kinetic energy in a combustion engine. Both processes rely on the large amounts of heat energy that are stored in natural deposits such as coal and petroleum. The process of converting this heat energy into other, more useful forms induces environmental damage due to the largest bifactor of burning fossil fuels, CO_2.

While the power production industry struggles to convert its heat energy into electrical energy, the electronics industry struggles to prevent and control the heat energy that is produced by electronic components. Processors are simultaneously shrinking and becoming more powerful, which increases the heat output, while reducing the area to which a heat sink can be attached. This has rendered standard air-cooling systems useless because they cannot produce a heat flux high enough to stop the microchips from overheating. Liquid cooling has become relatively common in industrial and commercial computers, but, on its own, cannot quite cope with the huge heat fluxes being produced.

One of the more recent methods of improving the capabilities of compact heat exchangers (CHE) is to reduce the size of the channels through which the working fluid is pumped, which increases the heat transfer coefficient (HTC), as shown in Figure 1-1. These channels with smaller diameters are referred to as mini- or microchannels. When the scale of channel-based heat exchangers is reduced to the micro level, different physical phenomena start controlling the behaviour of both the working fluid and the heat flux. As the channels get smaller, the effects of gravity and viscosity, which govern classical fluid dynamics, become dwarfed by intermolecular forces such as surface tension. Heat exchangers that use microchannels offer much larger heat fluxes than standard heat exchangers, but also induce larger pressure drops and therefore require more pumping power.
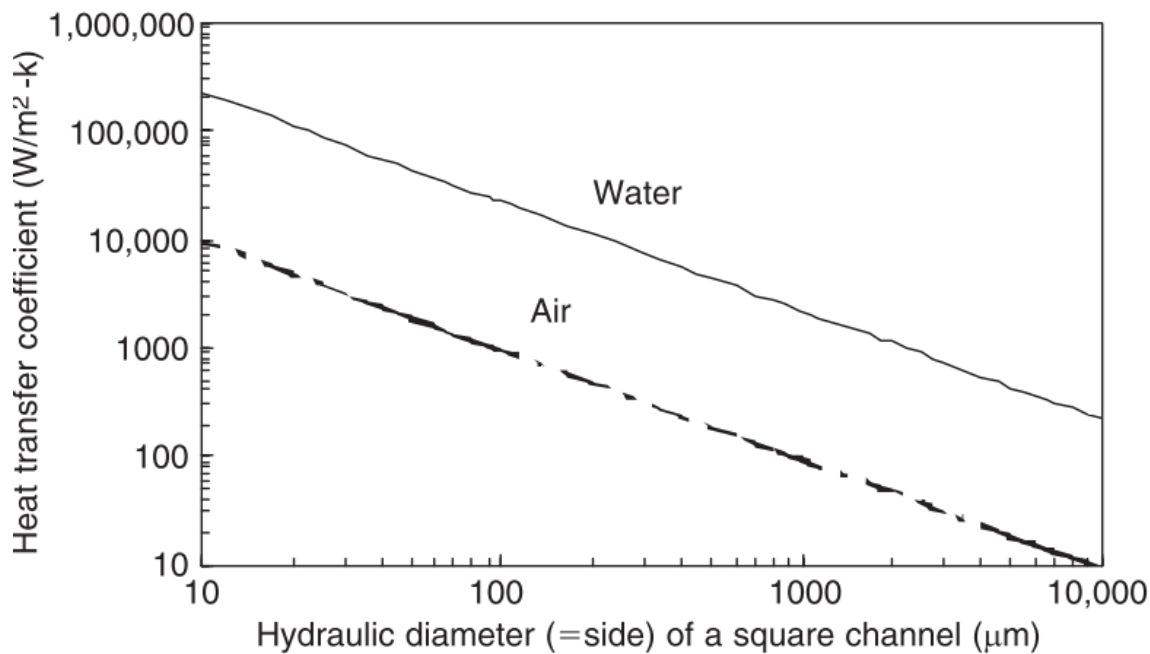
Figure 1-1: Variation of the heat transfer coefficient with channel size for fully developed laminar flow of air and water (Kandlikar et al., 2005)

The use of single-phase heat transfer in microchannels is sufficient for most applications, but some industries, such as the concentrated solar power (CSP) and microelectronics industries, can produce heat fluxes that are too high to be handled. Using a single-phase liquid relies on the sensible heat energy of the liquid to rise while it absorbs heat, which increases the temperature of the fluid and reduces the efficiency of the heat exchanger. A more volume-efficient method of increasing the amount of energy that can be absorbed is to harness both the sensible and latent energy of the fluid. This process heats the liquid to its saturation temperature, where it remains as the energy absorbed by the fluid is used to convert the fluid from a liquid to a vapour. This process is commonly referred to as flow boiling and can produce much larger heat fluxes than single-phase flow.

1.2. Motivation

Much research and experimentation has been done to find the influence of many different factors, such as the aspect ratio and geometry of the channel, on the heat transfer and pressure drop that are produced. Analysing physical phenomena becomes increasingly more difficult as the scale becomes smaller. Visualising and quantifying the effects of different parameters over wide variances is therefore difficult, expensive and tedious. This task is made significantly easier by making use of numerical investigations, which are performed using computational fluid dynamics (CFD) software.

This software allows the researcher to visualise and quantity micro-scale effects that cannot be experimentally visualised due to light diffraction, the channel surface, transparent fluids and many other factors.

Once a numerical model has been validated against experimental results, multiple changes to the setup can be made, and the effects they have on the solution can be quantified at a fraction of the time and cost. Certain phenomena can be modelled and simulated individually so that their impact on the behaviour of the system can be isolated. The results of these simulations, in conjunction with experimental results, can be used to create better heat transfer correlations that will assist in the design of better functioning CHEs.

1.3. Problem statement

Heat exchangers that utilise microchannels are becoming a promising technology in many industries, especially the CSP and microelectronics industries. The many geometrical and thermophysical requirements that can occur in industry have been a driving force for research into CHE optimisation, which has led to the development of microchannel-based CHEs. Due to the small scale of these channels, experimental studies have not managed to successfully quantify the relationship between the heat flux produced and the many variances that can be made to the geometry, orientation and other aspects of the system. Therefore, any optimisations can only be based on estimates.

Flow boiling is a highly complex process with many different phenomena influencing the behaviour of the system. Several of these phenomena, such as nucleation, departure and coalescence, are not well understood. Therefore, numerical investigations that involve these phenomena are scarce (Bi et al., 2019). This scarcity is also influenced by the 3D nature of flow boiling, which induces significantly higher computational costs than a 2D investigation would.

The effect that gravitational orientation has on bubble growth within high-aspect microchannels is not sufficiently understood, with few correlations available that dictate how bubbles grow when they are only confined in one direction, and when gravity is either forcing them against the heated surface, or are pulling them away from it. These effects will be investigated in a rectangular microchannel with a high aspect ratio. The numerical domain is shown in Figure 1-2.
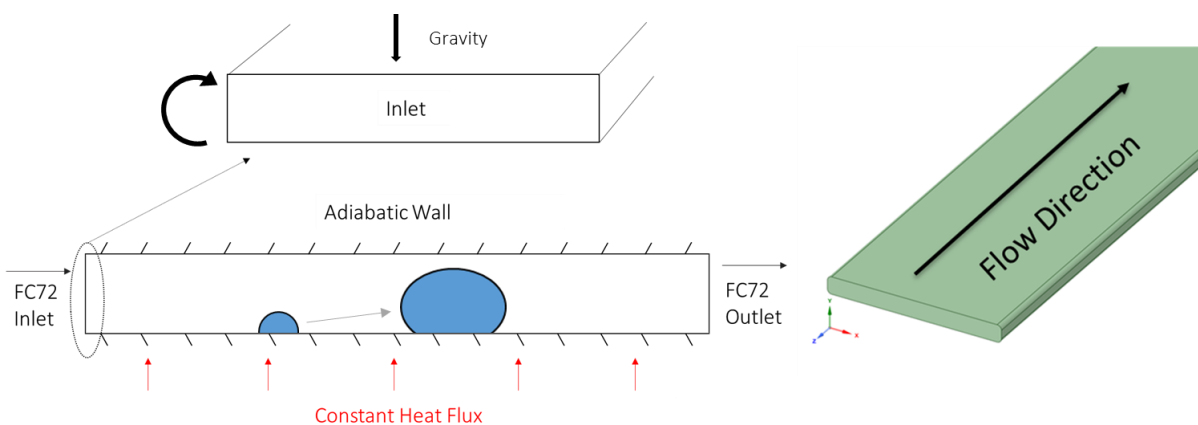
Figure 1-2: 3D numerical domain

1.4. Objective

Creating an accurate numerical model of flow boiling in a microchannel requires an in-depth understanding of the thermophysical phenomena that govern the transfer of heat and mass and the many model variations that can be implemented in Ansys Fluent 19.1F*. The microchannel in question differs from conventional numerical studies in many ways, such as the rectangular cross-section, the high aspect ratio and the inclusion of gravitational forces. The stage of boiling is also different, as few studies have strayed from simulation slug or annular flow.

The objectives of this study are as follows:

- Create a mesh refinement model that will reduce the computational cost of performing 3D simulations
- Create a mass transfer model using existing literature and implement it into Ansys Fluent using a user-defined function (UDF)
- Perform a 2D case study that will allow many variations of the contact angle and gravitational orientation to be performed
- Use the 2D case study to highlight interesting effects, and then recreate these cases in a 3D domain

In summary, the objective of this study is to give insight into the micro-scale effects that changing the gravitational orientation has on the growth of non-uniformly confined bubbles and how this results in different heat transfer characteristics.

1.5. Layout

The layout of this study is as follows.

- A thorough literature study is performed to gain insight into what research has been performed on flow boiling in microchannels and to highlight the gaps in this literature.
- An existing mass transfer model that has been used in multiple previous studies is written into the Ansys Fluent model, and several benchmark tests are performed to highlight the importance of this model.
- A mesh refinement model is developed, and several benchmark tests are performed to ensure that the model does not negatively affect the accuracy of the simulations.
- A bubble detachment model is developed based on a combination of experimental results and a 2D case study.
- Three cases are performed in a 3D domain, two of which were performed in the 2D domain and one is non-symmetric, which will highlight the effect of a channel with a high aspect ratio.
- The results of the 2D and 3D cases are analysed. A conclusion will be drawn from these results, and recommendations made for future work on the topic .

2. Literature study

2.1. Introduction

Due to their prevalence in the majority of heat exchangers used in industrial heat and fluid transfer applications, macro-scale channels have dominated the experimental and numerical studies done on the various properties that determine their performance. There is also a large disparity between experimental and numerical studies on microchannels, with experimental studies dominating the available literature (Talimi et al., 2012).

While there are many similarities between the capabilities and performance of macrochannels and microchannels, the large difference in scales means that the behaviour of the system is influenced by new factors, or it simply reacts differently to the existing factors. Surface tension, which is present in all fluid flows, but is usually neglected in macro-scale fluid flow analyses, starts to dominate the flow pattern, especially in two-phase flow (Triplett et al., 1999;Serizawa et al., 2002). The influence of surface tension has been found to render other factors, such as gravitational orientation, negligible in some cases (Triplett et al., 1999).

When two-phase flow is analysed in the micro scale, the formation and behaviour of bubbles becomes significantly more complex. The presence of these bubbles changes the flow of the fluid by decreasing the average density in the channel. At high heat fluxes, this causes an acceleration pressure drop that can be larger than the pressure drop that would exist without the presence of vapour (Kandlikar, 2002). The changes in density also cause flow patterns that are not present in most macro-scale flow boiling scenarios.

In some cases, such as two-phase flow in inclined tubes, the formed bubbles can start to flow in the opposite direction to the bulk fluid flow. When this happens, large pressure fluctuations can occur, which could potentially damage the structure of the microchannels or cause burnout (Kandlikar, 2002). This reverse flow could also damage the pumps being used, as most cannot handle two-phase flow.

This chapter presents a review of the available literature on flow boiling in microchannels. Aspects such as what is considered to be a microchannel, how two-phase flow in microchannels produces significant increases in heat transfer, how numerical investigations have been used to improve knowledge in the field, their potential applications in industry and other interesting phenomena will be investigated and discussed. The studied literature will then be used to judge where gaps in knowledge exist and how these gaps can be filled.

2.2. Engineering fundamentals and theories of microchannels

2.2.1. Channel classification

The many shapes, sizes and requirements that are present in any microchannel application make it difficult to pinpoint the exact moment that a system transitions from macro to micro scale. Simply classifying each system by channel size does not account for the difference in fluid viscosity or surface tension, and does not consider the geometry of the channel. Many researchers have proposed their own classifications. Some of these are defined in the section below.

Barber et al. (2009) proposed that the transition point from macro to micro scale should be based on the point at which classical fluid dynamics relations become less applicable than the effects of confinement. However, there were no definitive factors that could be used to obtain an exact transition point. Kandlikar (2002) based their channel classification purely on the hydraulic diameter of the channels, and proposed an intermediate category, minichannels. The ranges for these categories are above 3 mm for macrochannels, between 200 μm and 3 mm for minichannels and between 10 and 200 μm for microchannels. The region from 1 to 10 μm is a micro to nano transition region, and under 1 μm is regarded as a nanochannel.

Ong and Thome (2011) proposed new criteria for both the macro to micro threshold and flow pattern transitions. Their proposal is based on the confined bubble approach, which considers the growth of a confined bubble within small channels. They determined that the macro to micro threshold was a function of the channel confinement, surface tension, phase densities, mass velocity, viscosity, saturation temperature and flow pattern. They based the macro to micro scale threshold on the confinement number (Co), which is shown in Equation 2.11. Macro-scale behaviour is expected for a Co lower than 0.34, while micro-scale behaviour completely takes over once it is higher than 1. If the Co is between these two points, the scale is determined by the flow pattern.

Li and Wang (2003) determined the effect of channel size on two-phase flow experimentally, concluding that the transition from macro to micro scale begins at the threshold diameter (D_{tr}), and that micro-scale behaviour becomes dominant at the critical diameter (D_c). The diameters are found using the following relations:

$$D_{tr} = 1.75 \sqrt{\frac{\sigma}{g(\rho_L - \rho_v)}} \tag{2.1}$$

$$D_c = 0.224 \sqrt{\frac{\sigma}{g(\rho_L - \rho_v)}} \tag{2.2}$$

where ρ_L is the density of the liquid phase (kg/m^3), ρ_v is the density of the vapour phase (kg/m^3), g is the gravitational acceleration (m/s^2) and σ represents the interfacial tension between the phases or surface tension (N/m).

They found that the surface tension forces dominate the forces of gravity for $D < D_c$, while gravity dominated the flow behaviour for $D > D_{tr}$. The forces both influence the flow relatively evenly when $D_c < D < D_{tr}$. The threshold and critical diameters for water, glycol, R22 and R134a are shown in Table 2-1 for temperatures ranging from 283 to 450 K.

Table 2-1: Predicted threshold and critical diameters for water, glycol, R22 and R134a (Li and Wang, 2003)

Liquid	Temperature (K)	Surface tension (N/m)	D_{tr} (µm)	D_c (µm)
Water	300	0.0717	600	4 680
	350	0.0632	560	4 374
	400	0.0536	534	4 170
	450	0.0429	490	3 827
Glycol	300	0.0478	464	3 624
	330	0.0451	454	3 546
	360	0.0425	444	3 468
	373	0.0413	442	3 452
R22	283	0.0104	206	1 609
	303	0.0076	183	1 429
	323	0.0047	153	1 195
	333	0.0034	136	1 062
R134a	283	0.0103	207	1 617
	303	0.0075	183	1 429
	323	0.005	156	1 218
	333	0.0038	140	1 093

As can be seen from the many studies done, the transition point from macro to micro scale is not a definitive point and varies depending on the parameters considered. This has created many differing opinions on what is considered a microchannel. However, some terms exist that help correlate the behaviour of heat transfer systems of varying scales and properties. The methodology behind these terms and their uses will be described in the following section.

2.2.2. Dimensionless terms

Dimensionless analysis is a powerful tool that was developed to reduce the number of parameters of a system, as well as to help researchers develop better correlations and models. The terms group certain aspects of a system together so that their reliance on properties like velocity, channel diameter or viscosity are replaced with reliance on a single term. The system can then be scaled up or a property of the fluid can change without having to redo the experiments changing each parameter.

Many dimensionless terms have been developed to quantify the effects of factors such as gravity, surface tension and inertia on systems of varying scales. When considering heat transfer in microchannels, the most important of these terms are the Reynolds number (Re), the Nusselt number (Nu), the Prandtl number (Pr), the capillary number (Ca), the Weber number (We), the confinement number, the bond number (Bo) and the Eotwös number (Eö).

The most widely used term is the Re, which represents the ratio of inertial forces to viscous forces that are experienced by a fluid in motion. The Re is found using the following relation:

$$Re = \frac{V D_h}{v} \qquad (2.3)$$

where V is the free stream velocity (m/s), D_h is the hydraulic diameter (m) and v is the kinematic viscosity (m^2/s).

The transition point of the flow from laminar to turbulent is usually calculated using the Re, with the transition point of tubes with small diameters usually being around 2 300 (Çengel and Ghajar, 2015). The influence of two-phase flow has been shown to decrease this transition point, with Talimi et al. (2012) finding the transition point to be closer to 1 000. Mehendale et al. (2000) reported that fully developed turbulent flow has been achieved with significantly smaller Re than usual. Laminar-turbulent transition regions were found to occur over Re of 200 to 900, much lower than the usual 2 300.

The next term is the Nu, which is the ratio of convective to conductive heat transfer across the boundary between the solid and the liquid. The Nu is an important term for estimating heat transfer characteristics of systems with similar diameters and working fluids. The equation for the Nu is:

$$Nu = \frac{hD}{k} \qquad (2.4)$$

where h is the convective HTC (W/m^2) and k is the conductivity of the fluid (W/m).

The relation between the HTC, heat flux, temperature difference and Nu is given later in the report in Equation 2.16.

Sadeghi et al. (2010) conducted a study of the Nu relations for a series of microchannels of different cross-sectionional geometries and aspect ratios. Their model is based on the cross-sectional geometry, perimeter and polar moment of intertia. The Nu used by Sadeghi et al. (2010) is based on the square root of the cross-sectional area of the channel rather than the hydraulic diameter, and is related to Equation 2.4 by:

$$Nu_{\sqrt{A}} = \frac{P_r}{4\sqrt{A}} Nu \qquad (2.5)$$

where P_r is the perimeter (m) and A is the cross-sectional area (m^2).

Figure 2-1 shows the proposed $Nu_{\sqrt{A}}$ vs aspect ratio relations for different geometries.
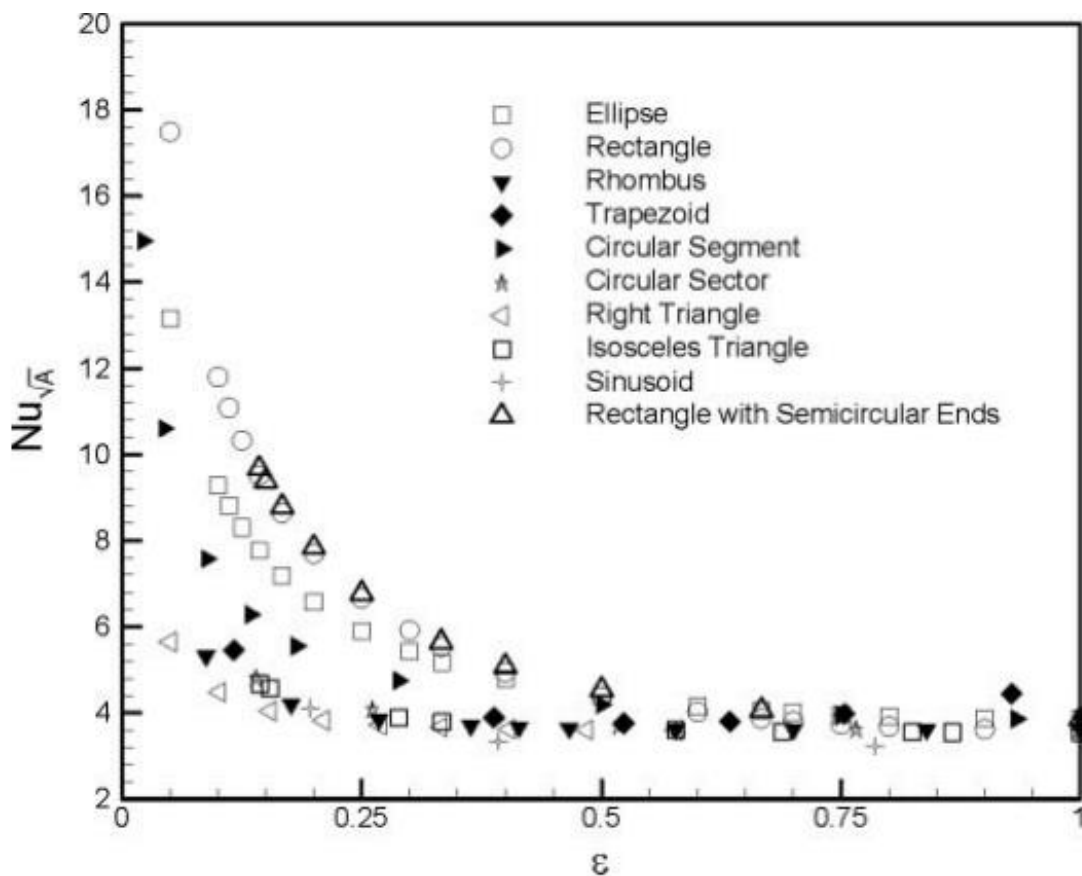
Figure 2-1: The Nusselt number for various cross-sectional geometries versus the aspect ratio (Sadeghi et al., 2010)

The Pr is the ratio of the momentum diffusion to thermal diffusion, and is defined as follows:

$$Pr = \frac{\mu c_p}{k} \tag{2.6}$$

where c_p is the specific heat capacity(J/kg.K).

The Pr, when used in conjunction with the Re, is a valuable tool used in Nu correlations for a number of different cases and geometries. For example, the average Nu for flow over cylinders of a variable cross-section is given by Çengel and Ghajar (2015):

$$Nu = C\,Re^m Pr^n \tag{2.7}$$

where C, m and n are constants determines by the Re and the cross-sectional profile of the cylinder.

The Ca is the ratio of viscous forces to interfacial tension forces, and is given as:

$$Ca = \frac{\mu V}{\sigma} \tag{2.8}$$

where μ is the dynamic viscosity (kg/m.s).

As the interfacial forces overcome the viscous forces, the layer is formed. The Ca is used as an indication of the size of this small liquid layer (Carlson and Dinh, 2007;Bretherton, 1961). Bretherton (1961) produced a thin film correlation which is 90% accurate until Ca < 5x0^{-3}:

$$\frac{\delta}{r} = 1.337 Ca^{2/3} \tag{2.9}$$

where δ is the film thickness (m) and r is the radius of the channel (m).

The We is the ratio of inertial forces to interfacial tension forces and is given by:

$$We = \frac{\rho V^2 D_h}{\sigma} \tag{2.10}$$

The We is useful in determining the maximum heat flux that a microchannel heat exchanger can produce. This correlation is shown in Equation 2.19.

Kew and Cornwell (1997) proposed a relation between the hydrodynamic properties of the fluid, as well as the diameter of the channel. This is known as the Co and is calculated using the following equation:

$$C_o = \frac{\left[\frac{\sigma}{g(\rho_L - \rho_v)}\right]^{0.5}}{D_h} \tag{2.11}$$

They concluded that the traditional flow boiling correlations only managed to predict behaviour until the Co reached above 0.5, at which point simple nucleate boiling correlations predict the behaviour of the system more accurately.

The Bo is the ratio of gravitational forces to interfacial forces between the liquid and gaseous phases (Bordbar et al., 2018). The nature of this study, which focuses on the effect of the orientation of the microchannel, ensures that the Bo is a vital aspect of the investigation. The Bo is given as:

$$Bo = \frac{(\rho_L - \rho_v)g D_h^2}{\sigma} \tag{2.12}$$

The Bo indicates the effects of buoyancy relative to surface tension and is related to the confinement number by Bo = 1/Co^2. Cheng and Wu (2006) used it as a macro- to micro-scale transition point. They based their classification on the experimental results of Li and Wang (2003). They found that the macro-scale threshold occurred at Bo > 3 and the micro-scale threshold occurred at Bo < 0.05. The intermediate region, 0.05 < Bo < 3, is defined as the meso or mini scale, and is dominated by both gravity and surface tension.

Brauner and Maron (1992) proposed the Eö, which represents the ratio of surface tension effects and gravity, to be the criterion for a shift from macro- to micro-scale physics . The Eö is given by:

$$Eö = \frac{(2\pi)^2 \sigma}{(\rho_L - \rho_v) D_h^2 g} \tag{2.13}$$

The effects of surface tension start to dominate the flow once the Eö of the system becomes greater than 1.

The dimensionless terms provided will be useful in characterising the heat transfer phenomena and flow regimes that will be present during flow boiling heat transfer. From this, meaningful heat transfer correlations can be developed, which will allow more freedom when scaling numerical models.

2.2.3. Boiling

Many industries have utilised single-phase flow in microchannels to induce a higher heat flow than can be obtained using macrochannels. However, the high heat fluxes required by some industries, such as the microelectronics industry, where heat fluxes can reach higher than 1 000 W/cm^2, render single-phase flow insufficient (Chinnov et al., 2015). To obtain higher heat fluxes, the evaporation of the working fluid is utilised in conjunction with the temperature change, which allows for a higher heat removal rate per unit mass, as well as an increased HTC during flow boiling (Kandlikar et al., 2005). Kandlikar et al. (2005) reported that the HTC obtained during two-phase flow in a 200 μm square channel can be over 10 times higher than the HTC obtained from the single-phase flow. Although boiling is the focus of the study, it is also noted that two-phase flow can be induced by adding air, another vapour or an immiscible liquid to the primary fluid prior to it entering the microchannel.

Boiling heat transfer can usually be divided into two categories: pool boiling and flow boiling. Pool boiling is when a fluid is heated without bulk fluid motion, while flow boiling encompasses this motion. While the primary focus is on flow boiling in microchannels, a solid understanding of pool boiling is needed to ensure that flow boiling is sufficiently described, because flow boiling is essentially pool boiling with a forced convective term added (Çengel and Ghajar, 2015).

Boiling starts when the fluid in contact with the heated surface has received enough energy to transition from a liquid to a vapour. Once enough vapour has accumulated, the force of buoyancy becomes stronger than the surface tension that is keeping the bubble attached to the surface. Once the bubble detaches, cooler water flows into its place, similar to the way natural convection carries heat away from the surface.

Boiling is broken down into three phases: nucleate, transition and film boiling. The respective temperature and heat flux relations of these phases are given in Figure 2-2. The first region is nucleate boiling, which is broken down into two different flows: isolated bubble and continuous flow. Isolated bubble flow takes place first when bubbles take a long time to form and are released individually into the bulk of the fluid before transferring some of their heat to the cooler liquid and collapsing. Once the frequency of bubble release is high enough, the bubbles start forming a continuous flow, which agitates the water, enhancing the convective effect and increasing the heat flux (Çengel and Ghajar, 2015).
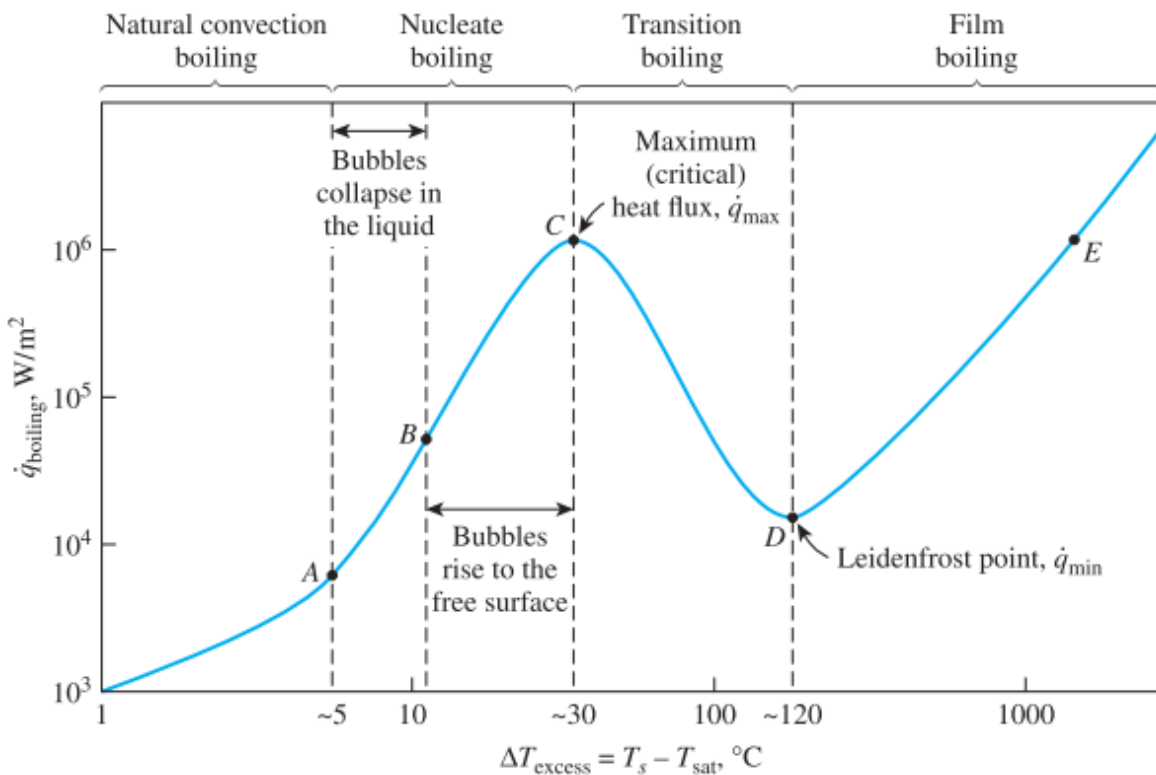
Figure 2-2: Pool boiling curve (Çengel and Ghajar, 2015)

Figure 2-2 shows that the best region for boiling to occur is the continuous nucleate boiling regime, which allows for a high heat flux at a lower temperature than transitional boiling can, as well as avoiding the extreme temperatures that are associated with film boiling. Transition boiling occurs when the vapour bubbles being formed cover a large part of the heated surface. This vapour film acts as an insulator, preventing the supplied heat from leaving the heater and forcing its temperature to rise. An increase in temperature causes a larger film to develop, and a compound effect is caused, raising the temperature until the entire heated surface is covered with a film of vapour. The temperature required to reach the same heat transfer rate as is experienced during nucleate boiling is usually higher than the melting temperature of the heater, which causes burnout (Barber et al., 2009).

The final flow regime is film boiling. This occurs when the vapour film produced by evaporation covers the entire heated surface, and the only way heat is transferred from the heated surface is by conduction through the vapour. Because the conductivity of a gas is much lower than that of a liquid, and the convection provided by the agitation is removed, a significantly higher temperature difference is required to obtain the same level of heat transfer as that obtained during the nucleate boiling regime.

Now that different flow regimes of pool boiling, as well as their corresponding heat transfer rates, have been explained, flow boiling can be examined. Flow boiling, which can be divided into internal and external flow, offers a much higher HTC than pool boiling due to the convection term added.

In external flow, the top surface of the fluid is open to the atmosphere, which allows vapour to escape and makes it much less complicated than internal flow (Çengel and Ghajar, 2015).

The second method of flow boiling, which is the focus of the current study, is internal flow boiling, or two-phase flow. This method of heat transfer has been thoroughly investigated and has been found to produce a significantly higher Nu than those obtained from other methods and flow regimes (Chinnov et al., 2015;Kandlikar et al., 2005). The relationship between temperature difference and heat transfer differs from that of pool boiling due to the convection term. Therefore, another boiling curve was produced. This is shown in Figure 2-3.
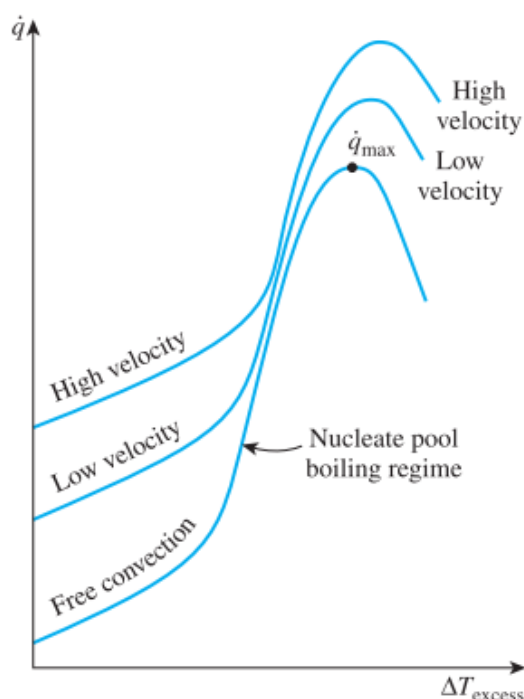
Figure 2-3: Flow boiling curve (Çengel and Ghajar, 2015)

This boiling curve shows that the heat transfer obtained is highly dependent on the velocity of the fluid, which demonstrates the importance of the Re. The HTC for single-phase flow can be determined using the known heat flux at the surface, the temperature of the wall and the local temperature of the fluid using the following equation (Wang et al., 2012):

$$h = \frac{\dot{q}}{T_W - T_L} \qquad (2.14)$$

where h is the local HTC (W/m^2.K), $\dot{q}$ is the heat flux (W/m^2), T_w is the temperature at the wall (K) and T_L is the local temperature of the liquid (K).

This local temperature is found by assuming that there is no slip at the walls, and that there is a small layer of thickness δt, which has a linear temperature distribution. The heat transfer rates via conduction and convection are then equated to obtain the following relation (Kandlikar et al., 2005):

$$\delta_t = \frac{k}{h} \tag{2.15}$$

where δ_t is the thickness of the liquid layer (m), k is the thermal conductivity of the liquid (W/m) and h is the single-phase HTC obtained prior to the onset of boiling (W/m²).

The local single-phase Nu can then be found by substituting the new HTC into Equation 2.4 to obtain:

$$Nu = \frac{\dot{q}D_h}{k(T_w - T_{L)}} \tag{2.16}$$

This relation makes the Nu much easier to calculate, because if a known heat flux and wall temperature can be applied, they can be used to calculate the HTC, which can be used later for flows where the heat flux is not known.

When analysing the HTC in two-phase flow, the local fluid temperature is replaced with the saturation temperature of the fluid (Ferrari et al., 2018):

$$h_m = \frac{\dot{q}}{T_w - T_{sat}} \tag{2.17}$$

where h_m is the two-phase local HTC.

The presence of two-phase flow makes the calculation of the Nu much more complicated, because, in the case of slug and annular flow, heat is conducted through the liquid layer into the vapour bubble, which requires the heat and mass transfer rates between the liquid and the bubble to be balanced. Researchers, such as Gupta et al. (2010) and Agostini et al. (2006), have calculated the h and Nu using the bulk temperature of the fluid rather than the local temperature, which is more appropriate for two-phase flow because the bulk temperature should be close to the saturation temperature of the fluid (Yao and Chang, 1983).

The Nu equation then becomes:

$$Nu = \frac{\dot{q}D_h}{k(T_w - T_{sat)}} \tag{2.18}$$

One of the most important aspects of a microchannel heat exchanger is the maximum heat flux that can be obtained, which is commonly referred to as the critical heat flux (CHF). This heat flux is reliant on both the channel and fluid properties. Therefore, an accurate model of exactly how these properties affect the CHF is difficult to produce. Wojtan et al. (2006), who based their study on a previous correlation by Katto and Ohno (1984), conducted experiments on the flow boiling of R-134a and R-245fa in two circular microchannels of of 0.5 mm and 0.8 mm in diameter, respectively, with uniform heat flux.

They produced the following correlations for the CHF, as well as the vapour quality at which this heat flux occurs:

$$\dot{q}_c = 0.437 \left(\frac{\rho_v}{\rho_L}\right)^{0.073} We^{-0.24} \left(\frac{L_H}{D_h}\right)^{-0.72} G h_L \tag{2.19}$$

$$x_c = \frac{4 \dot{q}_c L_H}{G(h_L + \Delta h_e) D_h} \tag{2.20}$$

where $\dot{q}_c$ is the CHF (W), x_c is the critical quality, L_H is the heated length (m), Δh_e is the inlet subcooling enthalpy and G is the mass flow rate (kg/s).

This correlation is only valid for circular microchannels with uniform heat flux, in which case it predicts the CHF with an error of 7.6%.

The fundamental nature of flow boiling, which converts a fluid to a vapour of significantly lower density, will disturb the stratified profile that is typical of laminar flow. This disturbance causes a multitude of different flow patterns, each with their own unique pressure drop and heat transfer characteristics.

2.2.4. Flow patterns

Due to the confined nature of internal flow boiling, vapour has no free surface from which to escape, and is rather forced to flow with the remaining liquid along the length of the channel. This vapour has distinctly different thermophysical properties than the liquid, and their interaction inside the channel causes some very interesting flow patterns. These two-phase flow patterns also occur when using two different liquids. This was demonstrated by Zhao et al. (2006), but the focus of this study will be on liquid-vapour two-phase flow patterns.

Many experimental and numerical studies have been performed on the different flow patterns that are produced as the quality of the working fluid increases. Some notable experimental studies were performed by Kreutzer et al. (2005) and Barber et al. (2009). Studies by Zhuan and Wang (2012), Bordbar et al. (2018), Guo et al. (2016) and many others focused on numerically simulating the behaviour of the various flow regimes.

Each of these regimes has its own unique behaviour, which results in different flow rates, pressure drops, heat transfer capabilities and instabilities (Bogojevic et al., 2009). These flow patterns can be divided into four major categories: bubbly flow, slug flow, churn flow and annular flow. A transitional region, which has combined properties, also exists between each of the various regimes.

Figure 2-4 gives a visual representation of each of the flows. Flows (a) and (b) represent bubbly flow; flows (c) and (d) show slug flow; flow (e) shows the transition from slug to churn flow; flow (f) shows churn flow; and flow (h) is annular flow. Flow (g) represent film flow, which occurs in vertical channels, where the liquid flows down the walls while the vapour flows in the opposite direction (Kreutzer et al., 2005).
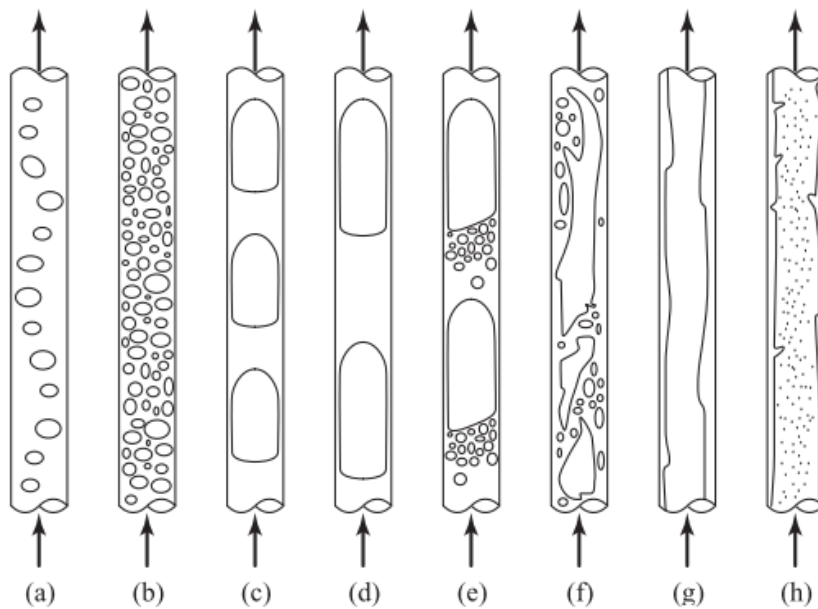
Figure 2-4: Different two-phase flow regimes (Kreutzer et al., 2005)

Once a subcooled liquid enters a heated microchannel, small bubbles start to form on the heated surface, which grow bigger as more heat is added and the vapour quality of the flow increases. Once these bubbles are large enough, they detach from the wall and form part of the flow, creating bubbly flow. This flow starts off with isolated bubbles flowing along with the liquid. As even more heat is added, the bubbles start to flow together. This is known as coalescent bubbly flow. These phases are synonymous with the isolated and coalescent nucleate boiling regimes that occur during pool boiling.

As more and more bubbles are formed and rise to the top of the channel, they coalesce. The diameters of the bubbles then start to reach the diameter of the tube, and their radial growth is stunted, forcing them to grow in the axial direction. This regime is known by many names, such as slug flow, Taylor flow, plug flow and segmented flow (Bordbar et al., 2018). Slug flow generally occurs when the vapour quality reaches around 11% (Zhuan and Wang, 2012). The slug flows relatively close to the centre of the channel, with a thin liquid layer between the bubble and the walls.

This thin liquid layer acts differently, depending on the geometry of the channel. The film is relatively uniform in circular channels, but the corners that are present in rectangular microchannels cause a build-up of liquid due to the increased surface area, which magnifies the shear stresses. Slug flow also demonstrates inner-bubble vapour circulation, which occurs when vapour flows along the axis of the microchannel (Che et al., 2013). Once the vapour reaches the liquid boundary, the flow is forced away from the axis along the curve of the bubble. This is demonstrated in Figure 2-5.
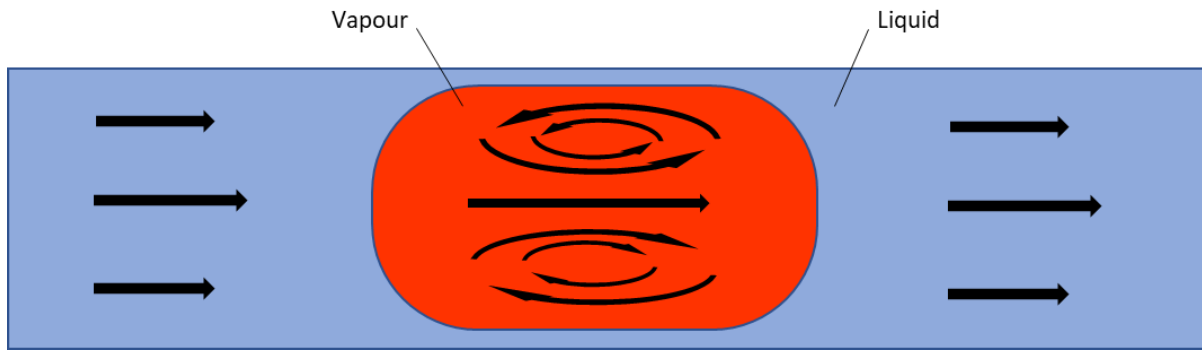
Figure 2-5: Vapour recirculation field inside the cylindrical slug (adapted from Che et al., 2013)

As the bubbles start to take over the entire channel diameter, the difference in velocity caused by the decrease in density of the fluid due to evaporation and the shear force experienced by the bubbles cause them to break apart and reform, causing instability in the flow. This is known as the churn flow regime, which is similar to annular flow with a number of random liquid slugs mixed in with the vapour bubbles (Kew and Cornwell, 1997).

Once the vapour quality is high enough, the bubbles that have typically been flowing along the top of the channel due to buoyancy and the instability of churn flow start to move towards the middle of the channel. The shear force experienced by the bubble interface becomes stronger than the force of buoyancy, and a ring of liquid flows around the perimeter of the channel, while the vapour flows continuously through the centre of the channel (Colombo and Fairweather, 2016). This is the annular flow regime. While it is hydrodynamically unstable and can often cause burnout, it is the most popular flow regime in microchannel flow boiling (Guo et al., 2016).

The liquid film that exists between the vapour bubbles and the channel wall in slug and annular flow is a major factor in the heat flux that the microchannel is capable of producing. The transition point between slug and annular flow, as well as the hydrodynamics of the liquid film, have been the focus of many experimental and numerical studies (Fouilland et al., 2010). Each flow regime can produce CHFs that vary along the length of the flow channel. The relationship between heat flux and the quality of the fluid was experimentally investigated by Szczukiewicz et al. (2012), who produced the HTC vs quality graph shown in Figure 2-6.

Figure 2-6 closely resembles the pool boiling curve shown in Figure 2-2, which signifies the relationship between the pool boiling regimes and the microchannel flow boiling regimes. This phenomenon correlates well with the findings of Kew and Cornwell (1997), who found that heat transfer in channels with a confinement number of above 0.5 was better predicted by using nucleate pool boiling relations.
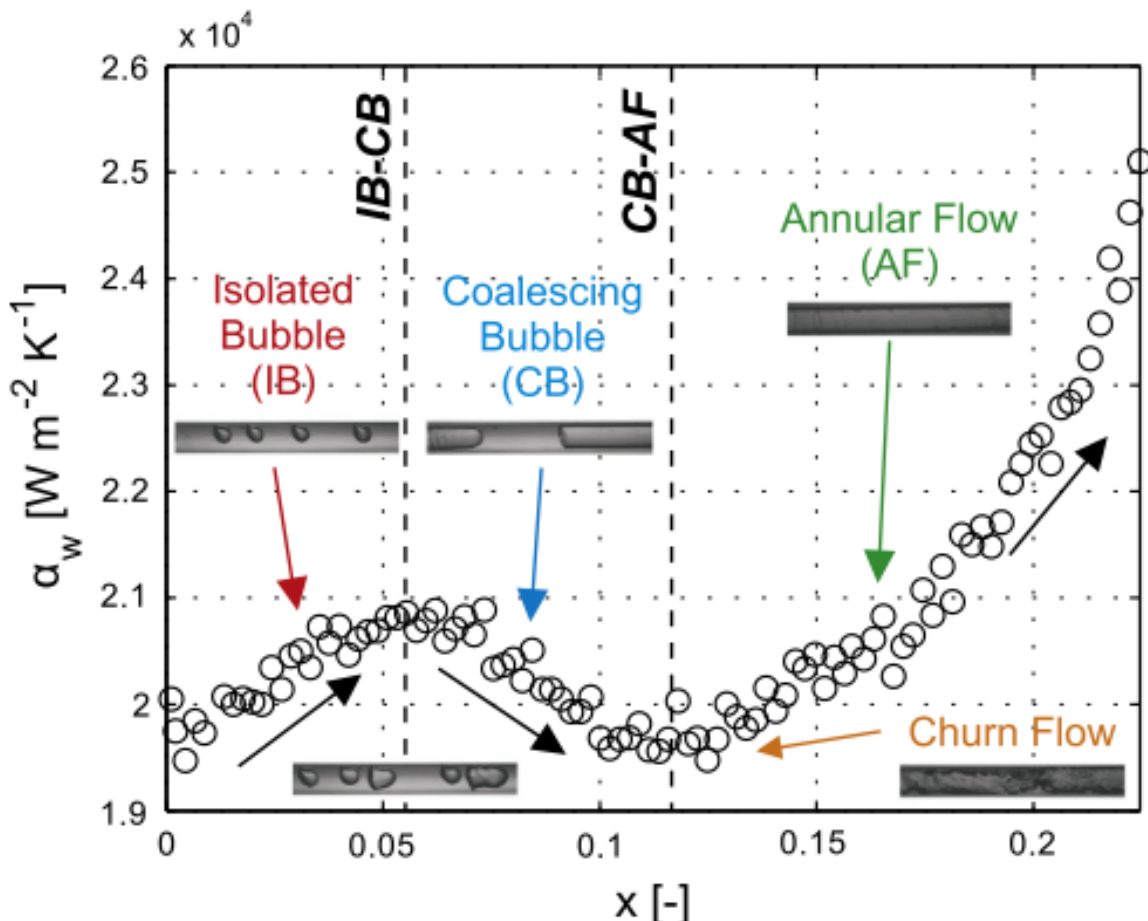
Figure 2-6: Experimentally obtained HTC vs quality for the flow boiling of 236fa in a silicone microchannel (Szczukiewicz et al., 2012). Flow visualisations by Revellin (2005)

The complex flow regimes bring with them large fluctuations in heat transfer over the walls of the microchannels, which can be used to the benefit of the CHE. However, the increase in heat transfer when utilising flow boiling in microchannels comes at a cost. The small channel size and the unstable nature of the flow regimes bring with them a pressure drop, increasing the amount of power required to pump the fluid.

2.2.5. Two-phase pressure drop and surface roughness

The pressure drop that occurs when a fluid is pumped through a confined channel is caused by a no-slip condition at the walls of the channel, which causes the fluid velocity at the wall to be zero. The flow in the centre of the channel is forced to increase due to the conservation of mass, which produces shear stresses between fluids flowing at different velocities. An analysis of previous experimental works done by Ribatski et al. (2006) proposed several trends. They proposed that the pressure drop increased with an increase in mass flux, but decreased with both an increase in saturation temperature and channel diameter.

The addition of another phase with a significantly different density and velocity brings several complexities to the calculation of these pressure drops during two-phase flow. Two different models of predicting this pressure drop have been reported in literature. The first method, known as the separated flow model, was proposed by Lockhart and Martinelli (1949). This model considers the flow of each phase separately, with each stream assumed to travel at the mean velocity of the said phase. The second method is the homogenous flow model, which treats the two-phase flow as single-phase flow. The properties of this flow are pseudo-properties based on the two different flows and their flow fractions (Ribatski et al., 2006).

Kandlikar et al. (2005) proposed that the pressure drop during the flow boiling of microchannels is comprised of six different components. The components are summed to provide the following correlation:

$$\Delta P = \Delta P_c + \Delta P_{f,1-ph} + \Delta P_{f,tp} + \Delta P_a + \Delta P_g + \Delta P_e$$

(2.21)

where ΔP is the total pressure change across the channel.

The subscripts denote what causes the component, where *c* is the contraction at the entrance, *f,1-ph* is the single-phase frictional pressure drop, *f,tp* is the two-phase frictional pressure drop, *a* is the acceleration due to the decreased density of the vapour, *g* is the effect of gravity and *e* is caused by expansion at the outlet.

The single- and two-phase pressure drop components are both functions of the friction factor of the channel, which is mostly determined by the surface roughness of the material. The surface roughness has a large impact on the contact angle of the bubbles that form on the channel walls, which influences the frequency of bubble release and the size of the released bubbles (Hecht et al., 2013).

Surface roughness increases the surface area to which a bubble would be exposed, even though the area of the channel wall remains constant. Hecht et al. (2013) found various causes and effects of the contact angle. They reported that an increase in pressure caused a larger contact angle, and that the size of the pressure drop affects the contact angle proportionately. Gravity was also found to affect the contact angle, but only when the bubbles are larger than several millimetres.

When bubbles nucleate, detach and bounce around the inside of the channel, they can cause pressure and heat flux fluctuations. When these fluctuations are close to the characteristic frequency of the channel, they can cause temperature and mechanical oscillations, whose formation criteria and effects are discussed below.

2.2.6. Instabilities

The rapid expanse and collapse of vapour bubbles and near-instantaneous accelerations caused by a sudden decrease in density can cause large temperature, pressure and HTC fluctuations, as well as mechanical vibrations.

The effects of these fluctuations vary, with backflow, flow maldistribution, burnout and mechanical damage all being reported in a summary by Szczukiewicz et al. (2014). They also proposed that the use of a micro-orifice at the inlet of the channel could be used to control the inlet condition of the flow, and through this, the flow in the channel can be stabilised.

The fluctuations mentioned are increased significantly when using several parallel microchannels, and can cause some of the microchannels to experience different flow regimes at the same transverse location (Bogojevic et al., 2009). Experiments done by both Bogojevic et al. (2009) and Barber et al. (2011) found that the type and magnitude of the flow instabilities were related to the heat flux and the inlet condition. A numerical investigation performed by Mohammed et al. (2011) found that artificially creating instabilities by using wavy microchannels of various amplitudes could increase the HTC. However, the pressure drop increased proportionately to the HTC increase.

Brutin et al. (2003) investigated the two-phase flow instabilities of n-pentane flowing through a rectangular microchannel with a hydraulic diameter of 889 μm. They judged unsteady flow as flow that had a fluctuation amplitude higher than 1 kPa and a characteristic oscillation frequency more than 20 (the characteristic oscillation frequency is the ratio of peak amplitude to noise amplitude). They produced Figure 2-7, which shows the stable regions on a graph of heat flux vs mass flow rate.
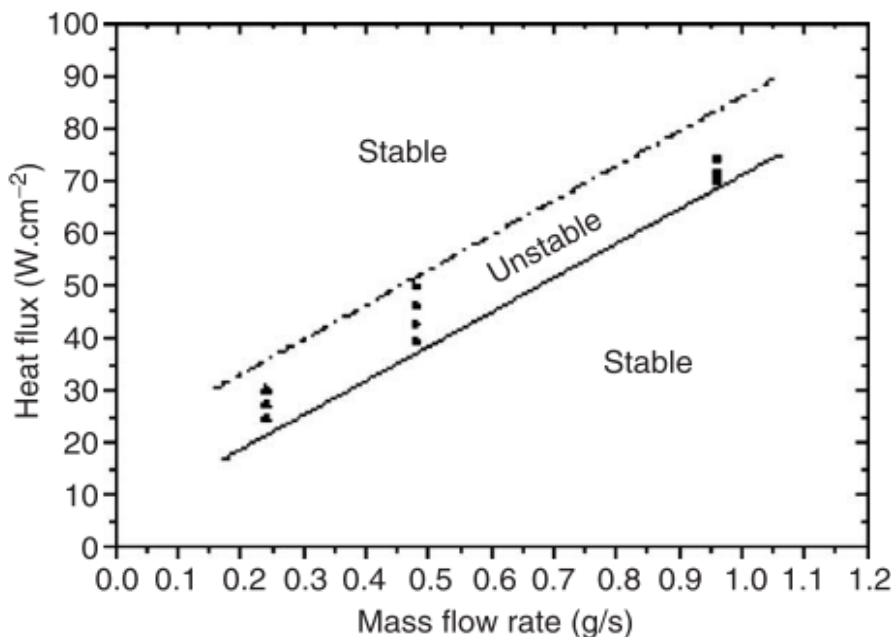
Figure 2-7: Stability diagram of heat flux as a function of mass flow rate (Brutin et al., 2003)

When designing CHEs, the instabilities that are caused by flow boiling and their impact on the system should be thoroughly investigated. While mechanical vibrations in the system should be avoided due to component damage, heat flux and temperature fluctuations can potentially increase the capabilities of the CHEs.

2.2.7. Other heat transfer enhancement methods

The many variations that can be applied to the geometry of the microchannels, flow regimes and working fluid properties require a vast amount of experimentation and numerical modelling to quantify the effects that each variation can cause. The shape, aspect ratio, hydraulic diameter, length and axial profile, as well as the presence of fins, all present complications to the flow that are not extensively investigated. However, some studies have shown that the performance of a CHE can be significantly improved by the inclusion of these complexities.

Korniliou (2018) experimentally tested a series of microchannels with aspect ratio values ranging from 0.33 to 3, and hydraulic diameters from 50 to 150 μm. Two-phase flow using water as the working fluid was the primary heat removal process. She found that a heat sink that comprised of multiple microchannels with aspect ratios of 1.5 and hydraulic diameters of 120 μm produced the maximum heat flux with relatively small pressure drops. She also found that high aspect ratios caused very fast bubble growth, but also caused flow complications such as dryout and backflow, which negatively affected all the other microchannels in the system due to unsteady flow rates.

Numerical investigations on heat transfer using wavy microchannels with rectangular cross-sections were done by Mohammed et al. (2011) and Sui et al. (2010). Their results were well correlated, with both studies finding that increasing the amplitude of the waves increased the heat transfer disproportionately to the increase in pressure drop until a certain point. Further investigation was done on the effects of varying the amplitude and wavelength along the length of the channel, which showed that increases in heat flux could be caused at different sections. This aspect is especially promising because of the non-uniform heat fluxes that are characteristic of microelectronic components. In many of these components, the gravitational orientation of the entire system may vary, depending on the purpose of the component. This has caused interest, and therefore experimentation, into how this orientation may affect the heat transfer performance of microchannel-based CHEs.

2.2.8. Research performed on gravitational effects

When analysing fluid flow in microchannels, their small volume-to-surface area ratios increase the influence of surface tension to the extent that the influence of most other physical mechanisms can be neglected. However, some research has shown that the effects of gravitational orientation on flow boiling in microchannels cannot be neglected, especially in channels on the upper side of the micro scale and channels with high aspect ratios.

A study performed by Kandlikar and Balasubramanian (2005) on a set of six parallel microchannels with a hydraulic diameter of 333 μm and an aspect ratio of 5 showed significant changes in the performance of the system when the flow direction of the channel was changed from vertically downward to horizontal, and then to vertically upward.

When changing the orientation from vertically downward to vertically upward, the resulting HTC increased by up to 40%. They also noticed a distinct change in both the shape of the vapour bubbles, as well as the backflow characteristics of the channels.

The next study was performed by Hsu et al. (2015), who altered the inclination of their 440 μm hydraulic diameter channel system from -90⁰ to 90⁰ in five increments. From this study, they concluded that the HTC obtained for the 45⁰ orientation was the highest, which is shown in Figure 2-8.
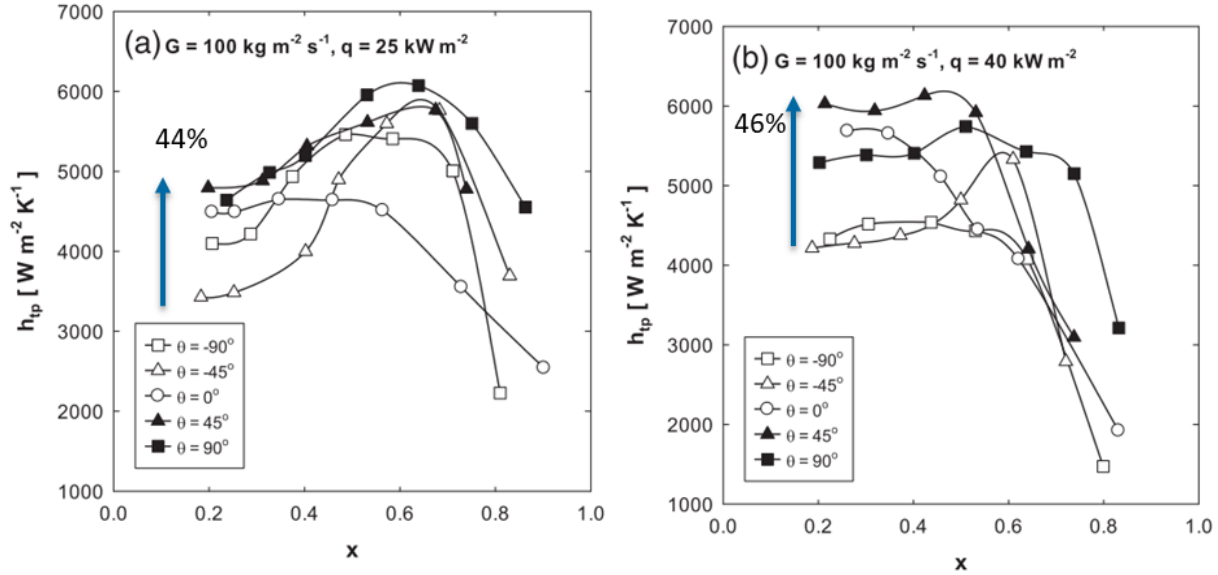
Figure 2-8: Heat transfer coefficient results obtained by Hsu et al. (2015)

The last study that will be examined was performed by Li et al. (2019), who altered the axial orientation of their 940 μm hydraulic diameter channel, which had an aspect ratio of 10.
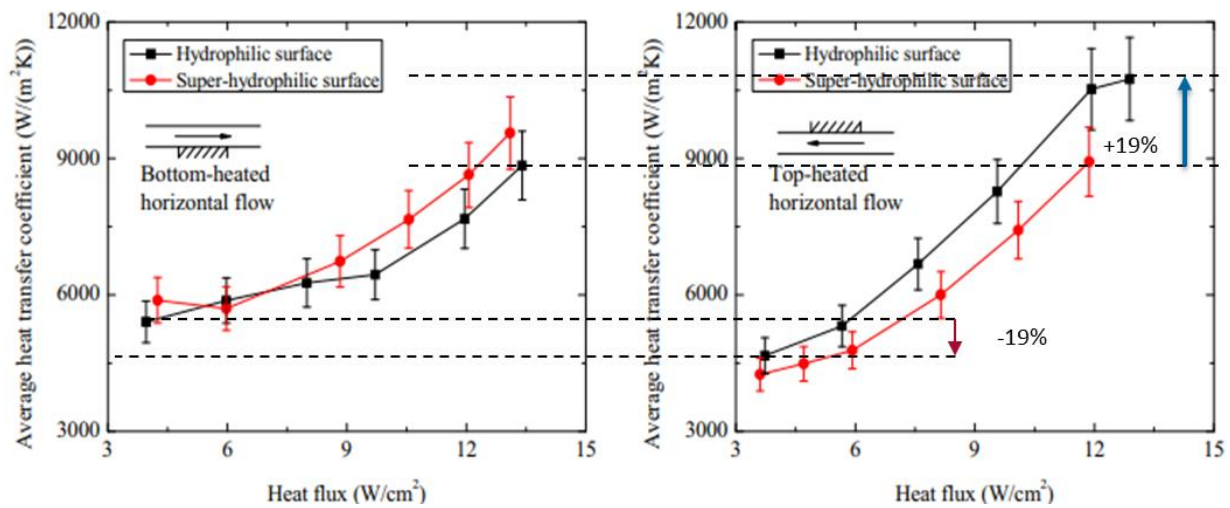
Figure 2-9: Average HTC results obtained by Li et al. (2019)

The experiments were done on a hydrophilic rectangular microchannel with only one heated face, which included heating the channel from only the bottom and only the top. The average HTC of the experiments heated from the top and from the bottom for both the lower and higher ranges of their applied heat flux, is demonstrated in Figure 2-9.

From these experimental studies, one can see that, in some instances, the gravitational orientation of the channels can influence the heat transfer characteristics significantly, and that the exact cause of this phenomenon is not currently understood or well quantified.

2.3. Numerical modelling of microchannel flow boiling

2.3.1. Introduction

Recent improvements that have occurred in the field of data capturing have helped researchers better record the small-scale phenomenon that affect heat and mass transfer. Technologies such as high-resolution infrared cameras have made visualising the temperature distributions within microchannels easier and more accurate. Despite these advances, current technology cannot accurately predict the exact state within microchannels due to their tiny sizes, the reflective indexes of the channel material and the incredibly small time-variations. An example of this is a report by Szczukiewicz et al. (2014), which states that the characteristic times of certain phenomena, such as bubble nucleation, are smaller than the response times of most thermocouples.

To better investigate the individual physical phenomena that occur in two-phase flow, CFD software can be used to model the system under investigation. The numerical model can then provide insight into what is happening at the micro scale, without the need for incredibly accurate and expensive monitoring equipment. While it may be impossible to simulate the scenario down to the molecular level, the errors that occur can be quantified and reduced to the extent that the solutions obtained are very similar to the actual solution, and theoretical models can be based on a combination of numerical and experimental results (Szczukiewicz et al., 2014). Due to the complex models and algorithms used by commercial CFD software, each case must be analysed individually to ensure that the most accurate models for each thermophysical aspect of the system are used.

Flow boiling in microchannels involves physical phenomena that occur at incredibly small scales, most notably surface tension and mass transfer. These tiny scales require minute mesh elements to correctly capture them, which induces incredibly high computational costs. Table 2-3, which is produced at the end of this section, shows that even 2D cases can involve several million cells, which require small time steps to ensure numerical stability and accuracy.

The high computational costs have limited most works to 2D studies, with 13 of the 21 cases from Table 2-3 being 2D. The cases are also limited by time, with most of the studies simulating less than a second of flow time.

23

Another limitation is the flow regime, with slug and annular flow being the most frequent. Nucleation, bubble departure and coalescence occur in a fraction of studies due to our limited understanding of the mechanisms behind them.

2.3.2. Modelling of slug flow

Slug flow is the most common regime to simulate numerically, with most of the studies listed in Table 2-3 focusing on it. One of the more common flow boiling models was presented by Thome (2004), which attempts to model heat transfer during slug flow as the elongated bubbles pass over the section of interest. This model divides the microchannel into three regimes with different HTCs. The first component of this model is when the liquid slug flows over the section of interest, followed by a currently evaporating elongated bubble and then finally a vapour slug. The model assumes that several bubbles will begin to nucleate on the microchannel wall. These bubbles stay in place after nucleation, growing until their radii reach the walls of the channel. The bubbles then detach from the wall and join the flow, where they continue to grow in the axial direction. At this stage, the flow is in the slug regime, which involves the flow of alternating liquid and vapour regions that are described by the three-zone model.

The hydrodynamics, as well as the heat transfer characteristics of large vapour slugs in an axisymmetric domain, was investigated by Magnini et al. (2013b), showing that the largest increases in HTC are obtained when the thickness of the liquid film between the slug and the wall is at its minimum, which usually occurs at the rear of the bubble. This increase is also felt in the wake of the bubble due to it interfering with the thermal boundary layer. This was built upon by Ferrari et al. (2018), who used the previous study as a base for a smaller 3D model. The same scenario was investigated, that of large slugs flowing in a microchannel, except that this study looked at flow within a square channel. They found that, in comparison to circular channels, the vapour slug velocity was always higher, and that the minimum film thickness was lower due to fluid being drawn to the corners of the channels.

2.3.3. Modelling of single bubble growth on heated surfaces

Ling et al. (2015) investigated the growth and merger of multiple bubbles in a 3D rectangular microchannel. A single bubble was placed on the wall of the microchannel and allowed to grow until fully confined, at which point it begins to grow along the length of the channel. The simulation was repeated with another bubble in front of it on the same wall, and another one with another bubble on the opposite wall. The investigation showed that the highest heat flux happened at the contact line between the bubble and the microchannel wall, and increased heat fluxes were found directly adjacent to this line, which decreased as one moved further into the liquid region. The interface between the bubble and the microchannel wall, which contained only vapour, exhibited the worst heat flux and the highest thermal boundary layer caused by the low conductivity and density of the gas.

Once two bubbles came into contact and merged, the oscillations that occurred as the surface tension forced the bubbles back into a sphere were also shown to interrupt the thermal boundary layer and increase the heat flux. As the bubble moves along the channel, lower temperature liquid is sucked into the region behind the bubble, leaving a high heat flux region in its wake.

Liu et al. (2017a) simulated the growth and detachment of a single bubble in a circular vertical channel. A single bubble was placed on the base of the cylinder. The bubble grew in proportion to the contact area between the bubble and the wall. The area initially grew, and the bubble became larger, but as gravity began to pull the bubble off the wall, the contact angle and contact area decreased, resulting in a lower growth rate. This implies that the growth rate of the bubble is influenced by the contact area between the bubble and the microchannel wall. As the bubble departs from the wall, liquid from the cooler bulk area is sucked into the void, improving the HTC of the heated surface.

Sanna et al. (2008) proposed a bubble detachment model based on experimentally observed bubble diameters. The method of enforcing departure is based on the contact angle between the liquid-vapour interface at the heated surface. The contact angle is kept in contact during an initial growth period. Once it reaches a characteristic diameter, the contact angle is gradually reduced. When the angle has been driven close to zero, the contact area between the vapour phase and the heated surface shrinks to zero, at which stage the bubble detaches. This process is illustrated in Figure 2-10, where part (a) has a constant contact angle and part (b) has a variable contact angle.
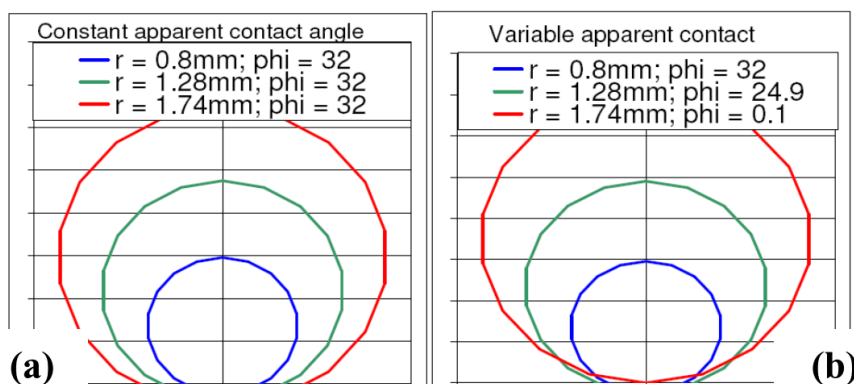
Figure 2-10: Variable contact angle bubble departure model by Sanna et al. (2008)

2.3.4. Mass transfer

The transfer of mass from liquid to vapour, and vice versa, is the most important aspect of this study. This transfer is what causes the boiling phenomenon and is why flow boiling offers such high heat transfer characteristics. However, correctly recreating mass transfer in a numerical simulation is incredibly difficult because the mechanisms that drive nucleation, coalescence, evaporation and condensation occur on a molecular level that cannot be correctly simulated using CFD. Therefore, only correlations and approximations based on experimental results can be used.

There are three primary mass transfer models in the literature that are implemented in most numerical studies (Kharangate and Mudawar, 2017). These models are the Rankine-Hugoniot jump condition, the Schrage model and the Lee model. These models are usually tweaked or simplified to better suit the study in question.

The Rankine-Hugoniot jump condition is a mass transfer model that relies purely on evaporation across the interface, and ignores the kinetic energy changes within this region (Kharangate and Mudawar, 2017). The mass transfer is calculated using:

$$S_g = -S_L = \frac{\left(k_L \nabla T_L - k_f \nabla T_f\right)|\nabla \alpha|}{h_L} \tag{2.22}$$

where S_e and S_c are the evaporation and condensation source terms, respectively (W/m²K).

The default mass transfer model in Ansys Fluent is the Lee model. However, this is more of a macro-scale model and induces phase change throughout the liquid domain. In the Lee model, evaporation and condensation are calculated via the following equation (Kharangate and Mudawar, 2017):

$$S_e = r_i \alpha_L \rho_L \frac{T - T_{sat}}{T_{sat}} \tag{2.23}$$

$$S_c = r_i \alpha_g \rho_g \frac{T - T_{sat}}{T_{sat}} \tag{2.24}$$

where r_i is the mass transfer intensity factor (1/s).

Multiplying the liquid and vapour volume fractions into each equation ensures that evaporation only occurs within the interface, and the liquid regime and condensation only occur in the interface and the vapour regime.

The next mass transfer model is the Schrage model (Schrage, 1953). This model is based on the kinetic theory of gases, and relates the transfer of mass on the difference in partial pressure across the interface, as well as an accommodation coefficient, ω, which is the ratio of excited molecules that cross the interface to the total number of excited molecules that strike the interface. The mass flux is given by the following equation (Kharangate and Mudawar, 2017):

$$\dot{m} = \frac{2\omega}{2 - \omega} \sqrt{\frac{M}{2\pi R}} \left[\frac{P_g}{\sqrt{T_{g,sat}}} - \frac{P_L}{\sqrt{T_{L,sat}}} \right] \tag{2.25}$$

where ω is an experimentally determined coefficient, which is usually set to 1.

Tanasawa (1991) simplified this by assuming that the mass flux across the interface is linearly dependent on the temperature difference across the interface, and that $T_{g,sat}$ and $T_{L,sat}$ are both constant and equal. This mass flux was then found using:

$$\dot{m} = \frac{2\omega}{2-\omega}\sqrt{\frac{M}{2\pi R}}\left[\frac{\rho_g h_{fg}(T - T_{sat})}{T}\right]$$
(2.26)

Once the mass flux is obtained, the mass transfer or source term is calculated as a function of the interfacial area:

$$S_g = -S_L = \dot{m}|\nabla\alpha|$$
(2.27)

The interfacial area term in Equation 2.27 is the magnitude of the gradient of the volume fraction, which ensures that evaporation only happens at the interface. In micro-scale flows, the tiny cell size focuses the mass transfer on a very small area, which can attempt to evaporate more liquid than exists in the cell and produce negative volume fractions. This makes the Tanasawa (1991) model, in its original form, inappropriate for micro-scale flow boiling (Kharangate and Mudawar, 2017). Hardt and Wondra (2008) proposed a smeared source term model that would conserve the net mass transfer across the interface, but would limit the vapour and liquid source terms to the pure vapour and liquid domains respectively, and ensure volume fraction conservation.

Each of these models utilises different assumptions and substitutions. Therefore, the specifics of each case should be taken into account before a model is chosen.

2.3.5. Mesh refinement

The division of the domain of interest into a collection of small elements, or nodes, is one of the most influential aspects of a CFD solution. The accuracy of the solution is highly dependent on the resolution of the mesh because the properties of each element are uniform throughout the entire element. Therefore, small changes cannot be properly captured by a mesh with large elements.

The simplest form of mesh is a structured mesh, which is similar to a Cartesian grid. The grid lines that originate from a face never cross each other, and grid lines from other faces only cross each line once. This allows each node to be identified by its position on its respective origin, similar to the Cartesian (x, y, z) system. These grids are mostly used for simple geometries because complex geometries can cause concentrations of cells that produce incredibly small elements with low qualities, which can be a waste of resources and can decrease the accuracy of the solution (Ferziger and Perić, 2002).

Unstructured grids are more popular for complex geometries because their elements can be of any shape or size, and there is no restriction on the distribution of the elements. Unstructured grids offer more freedom, but the difference in the shape and size of neighbouring elements can cause numerical errors and increase the time required to create the mesh and solve the solution (Ferziger and Perić, 2002).

During each iteration of the computation, the solution is solved at each individual cell in the domain. This creates a dependence of the computational time or cost on the number of cells in the domain. To decrease the time that each iteration takes, the number of cells in the domain should be kept to a minimum. However, some areas of the domain might need a much finer resolution to keep up the accuracy of scenarios, such as the thin liquid film at the wall of a microchannel or the interface between liquid and solid during bubble movement (Bordbar et al., 2018). To increase the resolution around specific areas, adaptive mesh refinement can be performed. This method changes specific areas of the mesh at set intervals, either every couple of iterations or every couple of time steps.

The adaption method is based on the error that is expected to occur over the cell size and the gradient of the specific area. The expected 2D error is calculated via the equation:

$$|e_{i1}| = (A_{cell})^{\frac{r_g}{2}}|\nabla f|$$

(2.28)

where e is the associated error, A_{cell} is the area of the cell, r_g is the gradient volume weight and ∇f is the Euclidean norm of the gradient of the chosen metric.

The curvature option of the gradient adaption approach uses the second derivative of the target metric, and the iso-value version uses the metric itself.

The purpose of adaptive meshing is to reduce the expected error. From Equation 2.28, one can see that the variables that determine the error are the cell area and the gradient. The gradient cannot be changed without affecting the solution. Therefore, reducing the cell area is the best way to reduce the expected error. The default adaption procedure in Ansys Fluent can be based on several different parameters, such as the pressure or temperature, but for two-phase flow simulations, the more common parameter is the gradient of the volume fraction, which refines cells that are within the interface. This method was used in studies performed by authors such as Fondelli et al. (2015) and Mehdizadeh et al. (2011).

Mehdizadeh et al. (2011) used adaptive mesh refinement to recreate a previous numerical investigation on slug flow in microchannels. Using their adaptive meshing technique, they were able to recreate the study using 96% less cells. They performed their investigation on a uniform 2D axisymmetric grid with base cell sizes of 50 µm, which were then refined eight times. This resulted in a cell size of 6.25 µm around the interface. The gradient of the volume fraction was used as the adaption metric, and all cells with a value of over 0.1 were refined every five time steps. Fondelli et al. (2015) used a similar method to recreate a dam break problem, which is a macro-scale problem. Therefore, larger cells could be used. They performed their investigation in 3D, which shows that this adaption method can be valuable in both 2D and 3D studies.

Another method of mesh adaption is to focus cells around the interface of the bubble, and to move the elements along with the bubble as it moves.

28

This method was used by Jafari and Okutucu-Özyurt (2016a), and was shown to provide accurate results. However, they found that, as the bubble grew, the cells that moved along with the interface were stretched and deformed, especially when the bubble grew and moved simultaneously. To ensure that the mesh still provided accurate results, it was regenerated once the elements were significantly deformed.

There are many ways of adapting or regenerating meshes, and each method should be tailored to better suit the application. The areas that require highlighting, the computational resources that are available and the mesh ratio of refined to unrefined cells all contribute to the necessity of using an adaptive meshing method over a static grid approach.

2.3.6 Summary of numerical studies

Table 2-2: Summary of numerical studies involving heat transfer in mini- and microchannels

Author	Title	Scope	2D/3D	Geometry	Solver	Mesh
Burk et al. (2019)	Computational examination of two-phase microchannel heat transfer correlations with conjugate heat spreading	Flow boiling with R134a for small channels with high heat fluxes	3D	0.1 x 1 mm	Comsol/Matlab	11 000 cells uniform mesh
Lorenzini and Joshi (2018)	Computational fluid dynamics modelling of flow boiling in microchannels with non-uniform heat flux	Simulate boiling from nucleation to bubble coalescence	3D	0.3 x 0.15 x 4.5 mm	Ansys Fluent 15	632 400 cells uniform mesh
Kurimoto et al. (2018)	Numerical investigation of bubble shape and flow field of gas-liquid slug flow in circular microchannels	Investigate effects of relevant dimensionless numbers on the bubble shape and the flow structure inside and outside a bubble	2D axisymmetric	0.32 mm circular	Not mentioned	Uses adaptive meshing with cells refined at bubble interface Minimum cell size: D/256
Ferrari et al. (2018)	Numerical analysis of slug flow boiling in square microchannels	Investigate effect of corners on slug flow boiling	3D	0.1 x 2 mm square	OpenFOAM	Semi-uniform mesh refined at wall by liquid layer. Large aspect ratio (up to 40)

Luo et al. (2017)	Numerical investigation of the bubble growth in horizontal rectangular microchannels	Investigate single vapour bubble evaporating and two lateral bubbles merging in a 2D microchannel	2D	1 x 0.2 mm	OpenFOAM	25 000 uniform mesh
Liu et al. (2017c)	Numerical study of the interactions and merge of multiple bubbles during convective boiling in microchannels	Study effects of mass flux, heat flux and saturation temperature on bubble merging	3D	0.64 x 5 mm circular	Not mentioned	Mesh refined around bubbles Minimum size: D/128.
Liu et al. (2017b)	A numerical study of the transition from slug to annular flow in microchannel convective boiling	Study effects of the transition. Findings are that this process disturbs thermal boundary layer, which further enhances bubble evaporation	2D	0.4 x 6 mm circular	Not mentioned	Refined around bubbles Minimum size: D/288
Liu et al. (2017a)	Numerical simulation of single bubble boiling behaviour	Analyse the bubble boiling dynamics, the transient pressure field, velocity field and temperature field in time	2D axisymmetric	5 x 5 mm	Comsol	400 000 cells Minimum size: 0.004 mm
Ma et al. (2016)	Numerical investigation on saturated boiling and heat transfer correlations in a vertical rectangular minichannel	Investigate saturated boiling mechanism by Ansys CFX based on the model that was validated by the experimental data from literature	3D	1.6 x 6.3 x 200 mm	Ansys CFX	1 290 000 with mesh refined at surfaces
Liu and Palm (2016)	Numerical study of bubbles rising and merging during convective boiling in microchannels	Conduct a 3D numerical study on bubble growth and merger in a microchannel with a diameter of 0.64 mm	3D	0.64 x 1.6 mm circular	Ansys Fluent	Minimum mesh size: D/128

Jafari and Okutucu-Özyurt (2016b)	Numerical simulation of flow boiling from an artificial cavity in a microchannel	Numerically simulate subcooled water boiling in which nucleation occurs from an artificial cavity on the inner surface of a microchannel	2D	0.1 x 64 mm	Comsol	Cell size ranges from 0.001 mm at the interface and wall to 0.008 mm in the bulk flow
Zu et al. (2011)	Confined bubble growth during flow boiling in a mini- or microchannel of rectangular cross-section part II: Approximate 3D numerical simulation	The numerical simulation aims to provide detailed information of the fields of velocity, temperature and pressure so as to further understand the effect of bubble growth on the flow field and heat transfer from the channel wall	3D	0.38 x 0.16 x 40 mm	Ansys Fluent	225 x 50 x 20 mesh used, non-uniform hexahedral mesh, 225 000 cells
Magnini and Thome (2016b)	Computational study of saturated flow boiling within a microchannel in the slug flow regime	Investigate the speed of bubbles and the influence of leading and trailing bubbles	2D axisymmetric	0.5 x 10 mm	Ansys Fluent	2×10^6 cells, square mesh
Guo et al. (2016)	Numerical simulation of annular flow hydrodynamics in microchannels	A CFD model is proposed and verified for the study of annular flow hydrodynamics in microchannels	2D axisymmetric	2 x 26 mm	Ansys Fluent	D/200 uniform mesh
Vivekanand and Raju (2015)	Simulation of evaporation heat transfer in a rectangular microchannel		2D	0.1 x 1 mm	Ansys Fluent	10 000 cells

Ling et al. (2015)	The 3D numerical simulation on bubble growth and merger in microchannel boiling flow	Simulate growth and merger of the bubbles and analyse the impact of the bubbles' merger on the heat transfer	3D	0.2 x 0.2 x 1 mm	Not Mentioned	0.004 mm uniform grid, 625 000 cells
Jesseela and Sobhan (2015)	Numerical modelling of annular flow with phase change in a microchannel	Carry out a numerical simulation to predict the characteristics of two-phase flow with liquid to vapour phase change in rectangular microchannels for a range of hydraulic diameters	Semi 3D	0.2 x 0.2-0.3 mm	Fortran	81 x 41 cross-section
Magnini et al. (2013b)	Numerical investigation of hydrodynamics and heat transfer of elongated bubbles during flow boiling in a microchannel	Perform numerical simulations of single elongated bubbles in flow boiling conditions within circular microchannels	2D axisymmetric	0.5 x 8 mm	Ansys Fluent	D/300, 720 000 cells uniform grid
Magnini et al. (2013a)	Numerical investigation of the influence of leading and sequential bubbles on slug flow boiling within a microchannel	Perform numerical simulations of multiple sequential elongated bubbles in flow boiling conditions within circular microchannels	2D axisymmetric	0.5 mm	Ansys Fluent	D/300, over 3 000 000 cells

Zhuan and Wang (2012)	Flow pattern of boiling in microchannel by numerical simulation	Looks at simulating nucleation and coalescence	2D	0.5 x 0.7 mm	Not mentioned	1 436 298
Mehdizadeh et al. (2011)	Numerical simulation of thermofluid characteristics of two-phase slug flow in microchannels	Investigating why slug flow produces such high heat transfer	2D	1.5 x 60 mm	ANSYS Fluent	D/30

2.4. Engineering applications

2.4.1. Microelectronics

Recent designs and innovations in the field of electronics have produced smaller and smaller components that can perform at a significantly higher rate than their predecessors. As the circuits get smaller and faster, the surface area to which a heat sink can be attached shrinks, while the heat output grows. This has driven researchers to develop many different cooling methods to ensure that the temperature of the circuits does not cause them to become inaccurate, inefficient or damaged.

The thermal resistance of the heat sink is the primary aspect that represents its performance and maximum heat flux. The thermal resistance is defined as follows (Husain and Kwang-Yong, 2008):

$$R_{th} = \frac{T_{s,o} - T_{f,i}}{\dot{q} A_s} \qquad (2.29)$$

where R_{th} is the thermal resistance (W/m), $T_{s,o}$ is the temperature of the substrate at the outlet/maximum temperature (K), $T_{f,I}$ is the temperature of the working fluid at the inlet/minimum temperature (K) and A_s is the exposed area of the substrate (m^2).

Bar-Cohen (1993) reported on a multitude of these cooling methods, including direct contact liquid cooling, miniature finned heat exchangers, jet impingement and minichannel substrates. They found that high velocity flow boiling in direct contact with the chip surface offered the most promising HTC.

Tuckerman and Pease (1981) studied the use of microchannels as heat sinks. They proposed that scaling down liquid cooling systems to the micro scale could increase the heat removal capabilities of heat from 20 W/cm^2 to over 1 000 W/cm^2. They developed a silicone substrate water-cooled heat sink, which they tested at heat fluxes of 790 W/cm^2. They used a heat sink with a series of microchannels with high aspect ratios (50 μm x 300 μm) and found that the thermal resistance of the system was tiny, resulting in a high heat flux. They concluded by recommending that non-uniform heat fluxes, which more closely represent the localised heat sources that exist on integrated chip surfaces, will increase the thermal resistance, albeit by a tiny amount.

Hassan et al. (2004) performed further research on the state of microchannel electronic cooling. They highlighted a number of aspects that are still in need of exploration. The effects of different working fluids should be more thoroughly investigated as most research so far has involved water as the working fluid. More experimental work needs to be conducted on surface roughness, which reportedly has a large effect of the pressure drop and HTC, to understand its effect on performance. Other factors were the geometry, varying heat fluxes, phase change and boiling regimes.

Husain and Kwang-Yong (2008) did an optimisation study on the shapes of the channels in a rectangular channel heat sink. They numerically modelled the channels and changed the aspect ratio to investigate its effect on performance. They found that thermal resistance decreases with an increase in aspect ratio until velocity starts to dominate the convective heat transfer.

A microchannel heat exchanger with a high aspect ratio attached directly to the surface of a microchip, shown in Figure 2-11, was tested by Yu et al. (2010). They found that a change in aspect ratio significantly affects the flow rate of the working fluid. When using an aspect ratio of 5:1 on a microchannel with a D_h of 20 μm, they managed to obtain a maximum HTC of 511 W/m^{2}K.
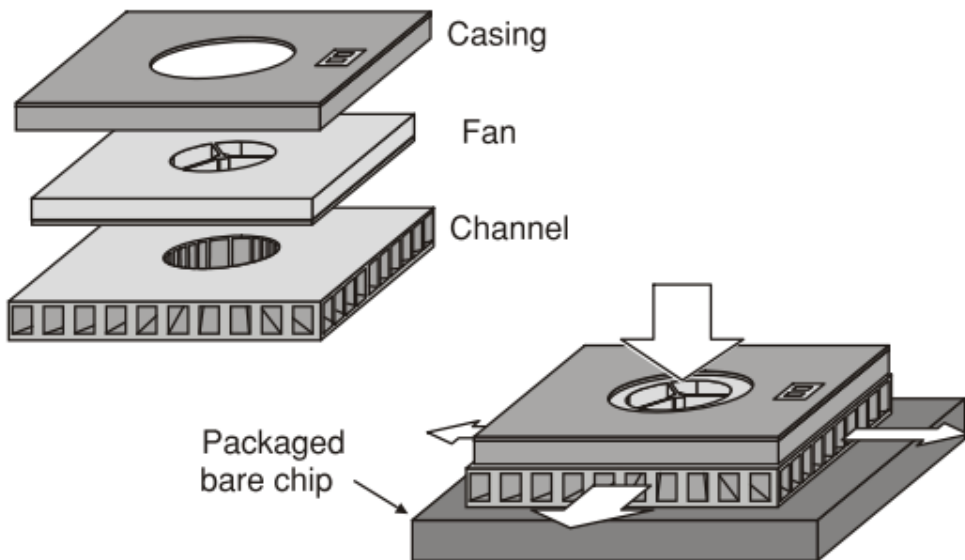
Figure 2-11: Microchannel cooling system proposed by Yu et al. (2010)

The working fluid is a vital component of a microchannel electronic cooling system. Kandlikar et al. (2005) proposed a set of characteristics that were required for a fluid to be an ideal contender. These characteristics are as follows:

- A high latent heat capacity
- A saturation pressure just above atmospheric pressure
- Good thermophysical properties (high conductivity, low viscosity, relevant electrical conductivity)
- Non-reactive with the common materials used in microchips (silicon, copper, solder)
- High dielectric constant
- Chemical stability
- Non-hazardous to humans and materials exposed in case of accidental leaks

2.4.2. Concentrated solar power plants

2.3.2.1. Overview

With global temperatures rising due to increased CO_2 in the atmosphere and dwindling coal reserves, the focus of many countries has shifted away from coal-fuelled power plants to more sustainable methods. Renewable energy production comes in many forms, such as hydropower, wind turbines, biofuel and solar energy, with hydropower being by far the largest contributor (IRENA, 2018).

Solar energy is one of the fastest-growing energy production methods that currently produces 18% of the world's total renewable electricity (IRENA, 2018). Photovoltaic (PV) cells are the most common type of solar energy due to their modularity, simplicity and price. The PV cells are installed in many households to supplement their energy needs, but most cannot rely purely on these panels due to their dependence on strong sunlight.

The PV cells have relatively low efficiencies and current battery technologies are not capable of storing electricity for long periods of time at a feasible price. While PV cells are a good investment when small-scale electricity production is required, large-scale production is becoming dominated by using CSP plants. The CSP plants operate by using mirrors to focus the sun's light onto a receiver of some sort, which usually heats up a heat transfer fluid. This can then either be stored or used to power a turbine (Moghimi Ardekani, 2017).

The concentration ratios and high temperatures that can be achieved by this technology increase the thermal performance of the system to levels to which PV cells cannot come close. Upscaling CSP plants is also significantly cheaper than establishing PV plants because a field of mirrors is much cheaper than a field of individual PV cells (Moghimi et al., 2015). The electricity produced by PV cells relies heavily on the amount of direct normal irradiation (DNI) that strikes the panel. Electricity production can be significantly slowed down on a cloudy day.

The need for a constant source of electricity, which is currently mostly produced by coal power stations, means that PV cells alone will not be able to consistently provide the energy requirements needed by households, businesses and factories. The CSP plants offer an alternative solar energy source that does not result in immediate electricity, but rather produces large amounts of heat. This heat does not have to be converted to electricity but can rather be stored so that a constant electric output is provided several hours after the sun has set.

The reflectors used at these plants can offer concentration ratios of up to 1:10 000, which can drive temperatures up as high as 2 000 ºC, which is much higher than the temperature at which most turbines can operate. These high concentration ratios are achieved using solar dishes, with other technologies offering much lower ratios.

Parabolic trough reflectors, which are most-often utilised, offer ratios of up to 100. While this may be lower than solar dish reflectors, the temperatures that are obtained using parabolic trough reflectors are still close to the operational temperature limit of most CSP plants.

Four types of CSP plant configurations dominate current research and are present in most operational CSP plants. These configurations are parabolic troughs, heliostat fields/central receivers, parabolic dishes and linear Fresnel reflectors (Craig et al., 2016). While central receivers offer the highest efficiency, their use is overshadowed by parabolic trough reflectors, which account for roughly 85% of operational CSP plants (del Río et al., 2018). The four configurations are shown in Figure 2-12.
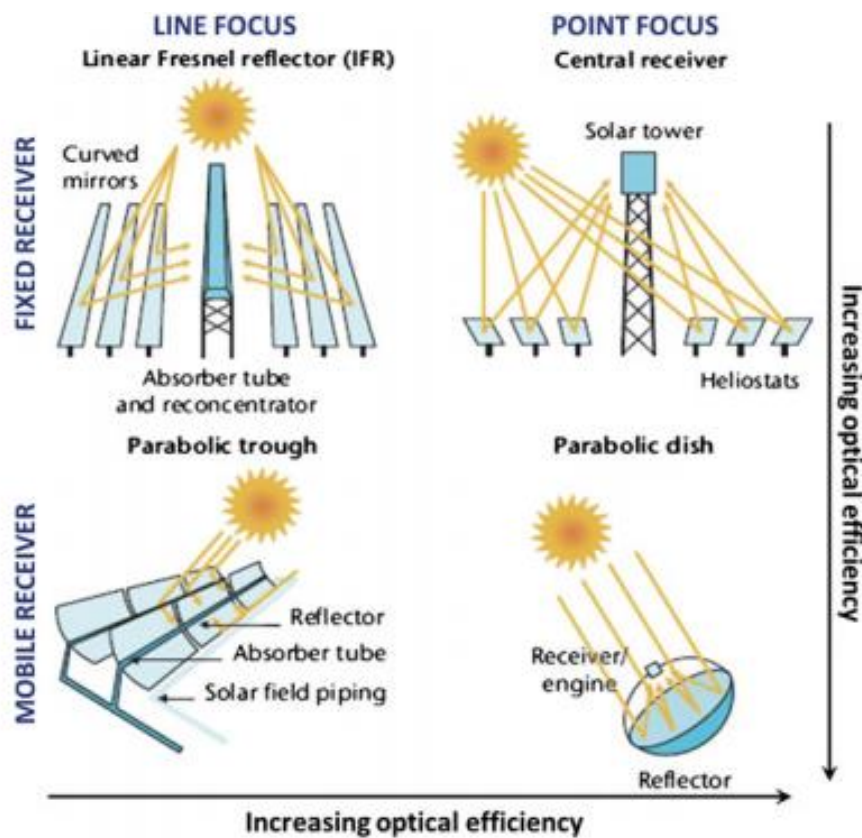
Figure 2-12: Concentrated solar power technologies (Serrano, 2017)

Parabolic trough reflectors operate by using long rows of parabolically shaped mirrors to concentrate sunlight into a fluid-filled pipe that runs parallel to the mirrors. A heat transfer fluid is pumped through the tubes, absorbing the sunlight with low thermal losses to the atmosphere (Moghimi and Ahmadi, 2018). The temperatures obtained in these tubes are usually limited to 400 ⁰C, which is the stability limit for the synthetic oils that are used in these plants (Serrano, 2017). The design of the troughs allows them to operate using one-axis tracking, which significantly decreases the cost and complexity of the tracking system and reduces the possibility of error.

Central receiver CSP plants use a large field of mirrors to focus incoming light onto a receiver at the top of a tower. The receivers can utilise various heat transfer systems, such as the same fluid-based system used in parabolic trough systems. Steam can be directly produced for use in a Rankine cycle turbine or air itself can be heated directly to power a Stirling cycle (Ho, 2017). Central receivers can obtain concentration ratios up to 5 000 and temperatures up to 2 000 °C (Li et al., 2016).

Linear Fresnel reflectors consist of several long, thin mirrors that are set at slightly different angles to focus sunlight onto a receiver similar to those used in parabolic trough reflectors. The shape of the mirrors and their sizes reduce the cost of the system and allow single-axis tracking to be used (Moghimi et al., 2017). These systems usually pump water through the pipes to generate steam directly for use in a Rankine cycle turbine.

The fourth CSP configuration is the parabolic dish reflector, which has a separate receiver and generator for each dish. The dishes are large and expensive, and require two-axis tracking, but offer huge concentration ratios and temperatures much higher than that which the other CSP variants can obtain (Ho, 2017). The dish heats up air directly for use in a microturbine, which reduces the feasibility of heat storage.

The CSP plants still require a significant amount of research and testing to improve their efficiency and lower their costs. Several countries, such as the USA and Spain, have already constructed several CSP plants, with an installed capacity of 4 GW and 1.75 GW, respectively (IRENA, 2018).

2.3.2.2. Energy storage

Many variants of storage systems have been proposed as alternatives to batteries since solar energy started to become a major contributor to the world's energy consumption. Many of the storage systems proposed can extend the production of electricity for over 10 hours, which allows the plant to run for 24 hours a day, seven days a week (Simbolotti, 2013).

The most popular form of storage is a two-tank system, which stores the heat transfer fluid that has been run through the receiver (Simbolotti, 2013). The fluid flow rate through the receiver is higher than the flow rate through the heat exchanger to the turbine, and the excess fluid is stored in a large tank. Once the fluid has passed through the heat exchanger, it is stored in another large tank through the night. Once the sun has risen, the fluid can start being pumped through the receiver again. This storage method relies on the storage of heat sensibly, with the total heat stored in the fluid calculated using the following equation (Çengel and Ghajar, 2015):

$$Q = mc_p \Delta T \tag{2.30}$$

where Q is the heat stored (J), m is the mass of the storage fluid (kg), c_p is the specific heat capacity (j/kg.K) and ΔT is the temperature change of the fluid (K).

Sensible heat storage is the simplest method to use, but decreases the thermal efficiency of the plant due to the decrease in temperature once the fluid starts to lose energy. A more efficient method is to store the heat latently in some sort of phase-change material. At first, the storage medium releases heat sensibly until it reaches its melting temperature. A phase of constant temperature heat release follows, which relies on the latent heat capacity of the fluid (Çengel and Ghajar, 2015):

$$Q = mh_L \tag{2.31}$$

where h_L is the latent heat capacity(J/kg).

The latent heat storage capacity of most materials dwarfs the sensible heat capacity, and the combination of the two methods allows for significantly lower material and space requirements to meet the storage needs. These storage methods require a large amount of heat transfer from the heat transfer fluid to the storage system and back to the fluid. This means that heat exchangers are a vital part of the system, and any improvement to the heat fluxes obtained could reduce the cost and size of the system, while simultaneously improving the efficiency of the entire plant.

2.3.3.3. Use in thermal receivers

Parabolic trough CSP plants have dominated the industry for some time, but other competing technologies are becoming more efficient and cost effective, with technologies using central receivers and heliostat fields becoming more popular. At the end of 2016, 60% of the CSP plants being constructed were utilising central receiver technology (Ho, 2017).

Central receivers offer much larger concentration ratios than parabolic trough fields, which allow higher temperatures to be reached (Serrano, 2017). However, with higher temperatures, higher thermal losses are experienced due to convection and radiation (Ho, 2017). At high temperatures, radiation and convection dominate the thermal losses, and both heat transfer methods are proportional to the area and temperature of the receiver. The relationship between radiation heat transfer, area and temperature are expressed as follows (Çengel and Ghajar, 2015):

$$\dot{Q} = A\sigma_s \varepsilon (T_s{}^4 - T_\infty{}^4) \tag{2.32}$$

where $\dot{Q}$ is the heat loss (W), A is the surface area (m^2), σ_s is the Stefan-Boltzmann constant (W/(m^2.K^4)), ε is the emissivity (W/m^2), T_s is the surface temperature (K) and T_∞ is the temperature of the surroundings (K).

The heat loss is proportional to the temperature to the power of 4. Increases in temperature therefore induce disproportional heat losses. The design of the solar receivers must therefore balance the increase in efficiency due to high temperature with higher radiation losses (Steinfeld and Schubnell, 1993).

Due to their high heat fluxes and small area requirements, microchannels have been examined as a potential addition to central receiver technology. They allow for massive amounts of heat transfer at high temperatures without the increase in surface area that would be required without the technology. The receivers that utilise mini- and microchannels are referred to as CHEs, which have been the topic of several experimental and numerical investigations (Ho, 2017).

Besarati et al. (2015) performed a numerical investigation on the effects of channel diameter and spacing on the heat flux and pressure drop of a CHE for use in a central receiver CSP plant, which uses supercritical CO_2 as the working fluid. In the study, the working fluid is heated from 530 to 700 ºC inside the CHE. The heat exchanger comprised several square channels inside a block made of Inconel 625, as depicted in Figure 2-13.
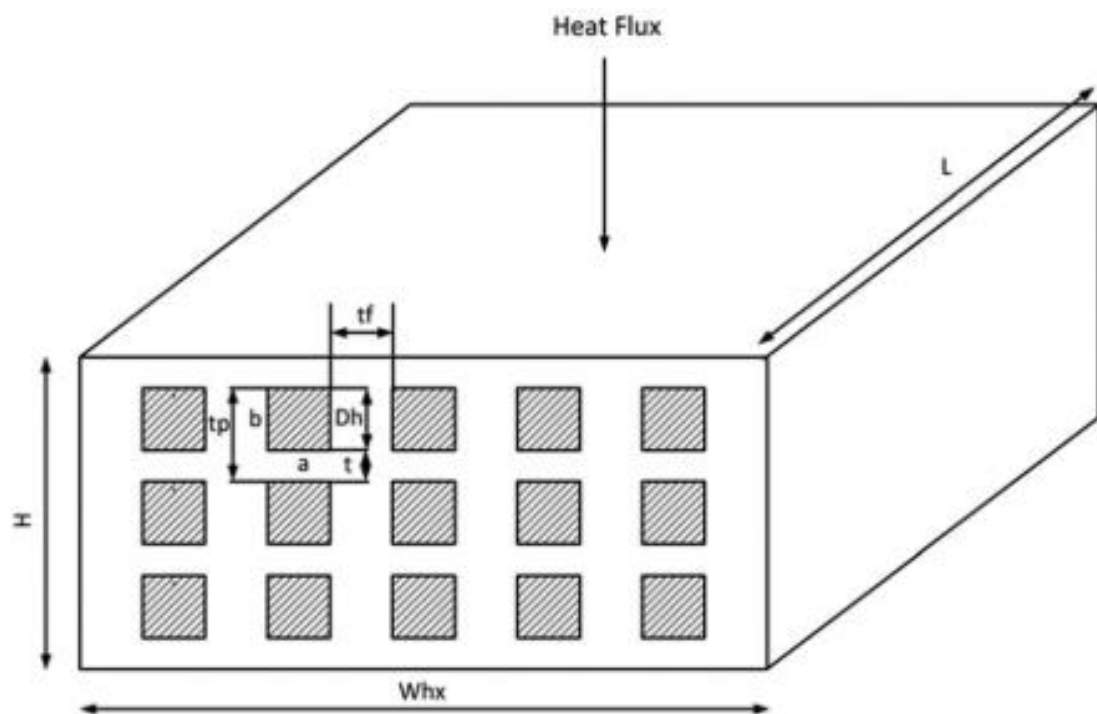

Figure 2-13: Compact heat exchanger configuration (Lei et al., 2007)

The study found that the thermal performance and pressure drop of the heat exchanger were both inversely proportional to the channel diameter. A multi-objective optimisation was performed, which concluded that the increased heat fluxes and pressure drops were balanced when the channel diameter was 2.8 mm.

A receiver concept developed at Oregon State University was reported by (Zada et al., 2016). They found that using multiple cells comprised of microchannels and microscale pin fins in parallel allowed them to achieve thermal efficiencies of up to 90% without inducing large pressure drops. Other studies on the use of small diameter channels in central receivers were done by Padilla et al. (2015), Ortega et al. (2015a), Ortega et al. (2015b) and Roldán et al. (2016).

The changing orientation of both the sun and the mirrors, as well as the wide-spread nature of CSP plants, ensures that the solar receiver will have to be orientated at an angle that will allow it to receive most of the incoming irradiation at a right angle. Since the optimum receiver angle may not be perpendicular to the ground, the effects of gravitational orientation on the heat transfer characteristics of microchannel flow boiling need to be analysed before a microchannel based heat exchanger that utilised flow boiling can be implemented in a CSP receiver.

2.3.3.4. Use in equipment cooling and accuracy of tracking

Due to the concentrating properties of curved mirrors, as well as the constant change in the position of the sun, very accurate solar trackers are required to ensure that the sunlight reflected off each mirror is directed at the solar receiver with as little error as possible. While parabolic trough technology only relies on one-axis tracking, heliostats and solar dishes, it requires highly accurate two-axis tracking.

Both the thermal and electrical conductivity of most materials relies heavily on the temperature of the component. Because CSP plants rely on high levels of DNI, the temperature of the surroundings can reach levels high enough to impact on the performance of computer-based equipment. If the tracking systems in the plant reach temperatures that are too high, they lose accuracy and can drastically decrease the efficiency of the plant.

Research on the impact of temperature on the performance of tracking equipment was found to be scarce. However, some studies were done on the impact of tracking errors on the efficiency of the system. Zhao et al. (2016) performed a study on the effect of tracking errors on the performance of parabolic trough receivers. They found that the tracking error must be less than 0.2% for optimal heat absorption by the working fluid.

Freeman et al. (2014) performed a review on several published studies involving the tracking errors and the effects that are experienced in heliostat reflector fields. They quoted allowable tracking errors of up to 0.1 degrees. They found that if the resolution of the encoder, which measures the angular rotation of the actuators, is too low, it can cause significant tracking errors. They found that the reference angle of the azimuth also produced significant errors if the sensor calibration was not high enough.

Due to the sensitivity of the electronic components that are used for tracking temperature, microchannel heat sinks are a viable technology to remove the high heat fluxes that are produced by CSP plants. However, designing a system with such large-scale variations is difficult, if not impossible, without a comprehensive knowledge of the inner workings of the system and a good estimation of the behaviour and performance of the many components. Creating and analysing a system model by means of hand calculations is unfeasible. Therefore, numerical models that can easily be altered and optimised are much better suited.

2.5. Conclusion

Current research into fluid flow and heat transfer in the micro scale has shown to display many different characteristics to macro-scale flow. However, there is a large disparity between the two, with macro-scale research dominating the available literature. The transition point between the macro and the micro scale is vague, with many different opinions and classifications. Experimental studies in microchannels are made incredibly difficult due to their small size, which makes flow visualisation, as well as temperature, pressure and heat flux readings, difficult to obtain. The difficulty in manufacturing microchannels has also limited research to mostly circular channels with uniform heat flux.

The heat flux obtained in microchannels from boiling has been shown to be significantly higher than that obtained in macrochannels, which is mostly due to the different mechanisms that drive heat transfer. Macrochannel heat transfer is dominated by flow boiling, which is well documented and quantified in literature. As the scale shrinks, the influence of gravity and viscosity is slowly replaced by the influence of surface tension, which completely dominates the flow once the $Bo < 0.05$. The intermediate region, where $0.05 < Bo < 3$, is dominated by gravity, viscosity and surface tension, with the influence of each of these properties in need of more investigation, especially in non-circular microchannels.

Investigating the phenomena that drive heat transfer in microchannels is made easier through the use of numerical modelling, which allows aspects of an investigation to be altered without having to physically recreate the microchannels, and for properties such as temperature, pressure and heat flux to be measured more accurately and easily. Numerical modelling allows for the optimisation of systems that would typically be too expensive and time consuming as very small changes to the geometry, orientation or material properties can be made almost instantaneously. Observations, such as temperature and velocity profiles, which are difficult to make in experimental studies, can easily be made using numerical studies.

The literature study performed highlighted many gaps in the research into microchannel heat transfer. In light of this, the following chapters in this study will contain a numerical investigation into bubble growth at different gravitational orientations in the intermediate Bo region.

3. Numerical modelling of microchannel flow boiling

3.1. Introduction

The nature of this study, which focuses on several 3D factors such as surface tension, the rectangular cross-section of the microchannel and the variation of gravity, requires several 3D simulations to be run to gauge the effect of these parameters. While 3D simulations of this nature have been performed in previous studies, the incredibly high mesh sizes that are required to correctly capture microscale effects have significantly limited the scope of research.

The most important microscale effect to capture in this study is the surface tension, as this is what governs the behaviour of bubbles within the system. It is possible to focus cells only within regions that contain a liquid-vapour interface. This will severely decrease the number of cells required within the system. However, it is imperative that the coarsening of cells within the bulk liquid and vapour regions does not compromise the accuracy of the model.

To ensure that the accuracy of the model remains within reasonable bounds, several benchmark tests are performed on variations of the mesh refinement model in the following chapter. First, the governing equations, solution procedure and discretisation methods that are used throughout these benchmark tests, as well as the proceeding numerical simulations, are described. This is followed by a description of the numerical domain within which the mesh refinement and mass transfer benchmark tests, as well as validation of the models against existing literature, are performed. The mass transfer and mesh refinement benchmark tests are then performed, followed by validation and verification against past numerical papers that will ensure mesh independence and correct mass transfer.

3.2. Numerical methods and axisymmetric domain

3.2.1. Governing equations

When performing numerical studies, the forces that govern the physical world are implemented on the system in question in a number of ways. Some forces, such as magnetism or Van der Waals forces, are usually either absent or unnoticeable, and can therefore be ignored. When it comes to CFD simulations, the conservation of mass, momentum and energy are the laws that define each system, and usually all three are required to obtain a usable solution. These are known as the Navier-Stokes equations.

The first equation is the conservation of mass, which ensures that mass can neither be created nor destroyed throughout the simulation:

$$\frac{\partial \rho}{\partial t} + \nabla(\rho \tilde{u}) = 0 \qquad (3.1)$$

where $\tilde{u}$ is a vector that contains all 3D velocity components.

The first part of the equation accounts for the volumetric change in density of the cell, and the second part accounts for mass entering and leaving the cell.

Even when mass is being conserved, the momentum stored within each cell also requires an equation to ensure that it cannot be created or destroyed:

$$\rho\left(\frac{\partial \tilde{u}}{\partial \tilde{t}} + \tilde{u}.\tilde{\nabla}\tilde{u}\right) = -\tilde{\nabla}P + \mu\tilde{\nabla}^2\tilde{u} + \rho g + \sigma\tilde{\kappa}\tilde{n}\delta \tag{3.2}$$

The left-hand side of this equation operates similarly to the conservation of mass by ensuring that the sum of momentum within the cell and the momentum leaving the cell via the movement of fluid remain balanced. The right-hand side of the equation contains the other terms, which can influence a cell's momentum. These are the pressure, viscous dissipation, gravitational head and surface tension.

The next equation is the conservation of energy, which governs the way that heat is conducted, advected or removed via phase change.

$$\rho c_p\left(\frac{\partial T}{\partial t} + \tilde{u}.\tilde{\nabla}T\right) = k\tilde{\nabla}^2 T + \tilde{\nabla}h_{LV}\dot{m} \tag{3.3}$$

Once again, the left-hand side of the equation operates similarly to the conservation of mass by ensuring that the heat within the cell and the heat entering or leaving the cell via the movement of fluid are balanced. The first term on the right-hand side represents heat that is moving via conduction, and the last term represents the heat that is absorbed at a constant temperature during phase change.

The next two equations are less common in CFD simulations than the previous three. However, they are just as vital to this study. The first equation is a standard advection equation, which monitors the movement of an arbitrary user-defined scalar quantity, $\emptyset$.

$$\frac{\partial \emptyset}{\partial t} + \nabla.\emptyset\tilde{u} = \emptyset\nabla.\emptyset \tag{3.4}$$

This equation is used for both the mass transfer and mesh refinement models that are used later in the study.

The last equation is the volume fraction advection equation, which ensures conservation of the volume fractions. It is always between 0 and 1.

$$\frac{1}{\rho}\left[\frac{\partial}{\partial t}(\alpha\rho) + \nabla.(\alpha\rho\tilde{u})\right] = \frac{1}{\rho_L}[S_\alpha + \dot{m}_V - \dot{m}_L] \tag{3.5}$$

The term on the left-hand side of the equation is an advection equation to govern the volume fraction that is entering or leaving the cell via the movement of mass, and the term on the right ensures that the volume fraction is conserved during evaporation, condensation or any other applied source terms.

To make solving the equations easier, a number of assumptions are made. First, both the liquid and the gas are incompressible (constant ρ), viscous ($\gamma \neq 0$) and immiscible, and the interfacial surface tension is constant (constant σ).

The low Re that is used throughout the study allows for the turbulence modelling to be set to laminar. The multiphase method that is used in the study is the volume of fluid (VOF) method, which treats the two phases as non-interpenetrating fluids that have a clearly defined interface. In this model, each part of the domain is given a value that is usually either 0 or 1. This represents the volume fraction of the two fluids and is denoted as c. The dimensionless single-fluid properties of the bulk fluid can then be calculated using c and the properties of the two phases can be calculated by using the following equations:

$$\overline{\emptyset} = \emptyset_L c + (1 - c)\emptyset_v$$

(3.6)

where $\emptyset$ can represent ρ, μ, k or c_P and where the superscript -- shows that the single-fluid approach has been implemented.

With these values representing the bulk of the flow, only a single set of conservation equations are required to be solved during each iteration.

Once the assumptions and single-fluid approach are implemented, the equations assume the following forms:

$$\nabla(\tilde{u}) = 0$$

(3.7a)

$$\bar{\rho}\left(\frac{\partial \tilde{u}}{\partial \tilde{t}} + \tilde{u}.\widetilde{\nabla}\tilde{u}\right) = -\widetilde{\nabla}P + \bar{\mu}\widetilde{\nabla}^2\tilde{u} + \bar{\rho}g + \sigma\tilde{\kappa}\tilde{n}\delta$$

(3.7b)

$$\bar{\rho}\bar{c}_p\left(\frac{\partial T}{\partial t} + \tilde{u}.\widetilde{\nabla}T\right) = \bar{k}\widetilde{\nabla}^2 T + \widetilde{\nabla}h_L\dot{m}$$

(3.7c)

$$\frac{\partial \emptyset}{\partial t} + \nabla.\emptyset\tilde{u} = \emptyset\nabla.\emptyset$$

(3.7d)

$$\frac{1}{\bar{\rho}}\left[\frac{\partial}{\partial t}(\alpha\bar{\rho}) + \nabla.(\alpha\bar{\rho}\tilde{u})\right] = \frac{1}{\bar{\rho}}[S_\alpha + \dot{m}_V - \dot{m}_L]$$

(3.7e)

Each of these equations will play a vital role in ensuring that the solution remains stable throughout each time step and that physically sound results are provided.

3.2.2. Discretisation methods and solution procedure

During each iteration, the equations that govern the system are solved in each cell in the domain. Some quantities can be taken directly from the cell. However, many terms in the governing equations are either temporal or special gradients. Because the domain is broken up into cells, differential gradients cannot be obtained, therefore, approximations to the gradients are used.

Ansys Fluent has several different solution strategies and discretisation methods, which can be used in many combinations. Each has its own advantages and disadvantages. The solver used in this study is the pressure-based solver, with the pressure calculated using PRESTO! (PREssure STaggered Option) scheme. The PRESTO! scheme obtains the pressure at each face of the cell using a discrete continuity balance.

After the continuity balance is done, the pressure and velocity are coupled by reformatting the continuity equation using a predictor-corrector method. The pressure-velocity coupling is done via the PISO (Pressure-Implicit with Splitting of Operators) method, which ensures that both the continuity and momentum equations are balanced by performing both neighbour and skewness corrections.

For each spatial gradient that is calculated, a second-order scheme is used. For both the momentum and energy equations, second-order upwind schemes are implemented, and for the volume fraction gradient, a second-order implicit method is used. During each iteration, the VOF interface is broken up into a cell value between 0 and 1 and a normal unit. The interface is then propagated via the advection equation before being reconstructed to form a sharp interface. To obtain the volume fractions at the cell faces and to reconstruct the interface, the compressive scheme is used, which is a high-resolution second-order scheme. The compressive scheme uses the cell face values, donor cell values and special gradients to recreate the VOF interface from the cell values and normal unit that are associated with the cell and its surroundings. An implicit body force is implemented in the VOF model, which accounts for pressure gradients and the forces between different phases within the momentum equation.

The time advancement is done via an implicit first-order time-stepping method. The time advancement is iterative and solves the continuity, momentum, energy, volume fraction and other scalar equations simultaneously until they have all converged bellow 0.0001. The time step is calculated via a limited Courant-Friedrichs Lewy number (CFL) criterion, where the time step is found by means of the following (Courant et al., 1967):

$$CFL = \frac{u\Delta t}{\Delta x} \tag{3.8}$$

The time step limitation, which is set to CFL = 0.25, ensures that the distance information travels during each time step, which is usually carried by the movement of the liquid, does not exceed the characteristic length of the mesh elements. This limitation ensures that the solution remains stable, and an additional limitation of $\Delta t_{max} < 1e-6$ s ensures that no more than 1% of liquid evaporates from each cell within a time step. These limitations produced time steps of between 2e-7 s and 1e-6 s for all simulations.

To initialise the solution, the following steps are performed:

1. Initially, the domain is run as a single-phase, steady-state case to initialise the temperature, velocity and pressure profiles.
2. The simulation is then changed to transient and the bubble is patched into the domain.
3. Once the bubble has been patched, the temperature within the bubble is set to the saturation temperature and the pressure is set to slightly above the surrounding pressure to account for the influence of surface tension.
4. All equations are turned off, and a single iteration is run.

5. The adjust functions are activated one by one with an iteration run in between them. This step ensures that all scalar variables are initialised so that, when called during the solution procedure, a value is present. If no values are present, an Ansys Fluent error occurs, and the process must be restarted.

6. Once all relevant scalar equations are initiated via the adjust functions, the last three scalar equations are initialised by implementing the mass and energy source terms and running the calculation for an iteration.

7. Lastly, the momentum, volume fraction, energy and scalar equations are reactivated.

The solution is then run transiently, where the following steps are followed during each iteration:

1. The first step in each iteration is to run each adjust function in the order in which it is implemented in the UDF.

2. The mass and energy source terms are calculated from the smeared source term.

3. The momentum equations are solved.

4. The mass continuity equation is solved, which is used to update the velocities.

5. The volume fraction equation is solved.

6. The energy equation is solved.

7. The scalar equations for the mass transfer and mesh adaption terms are solved.

8. The system properties are updated.

9. The residuals are checked. If they are above $1e^{-4}$, the solution starts again at Step 1. If they are below $1e^{-4}$, the solution has converged sufficiently, and it moves on to the next time step.

3.2.3. Axisymmetric computational domain

The numerical model is comprised of a pill-shaped vapour slug that flows through an axisymmetric domain. The slug flows through an adiabatic section to allow it to obtain a steady shape and motion. The bubble then flows through a heated section with a heat flux of 9 kW/m^2.
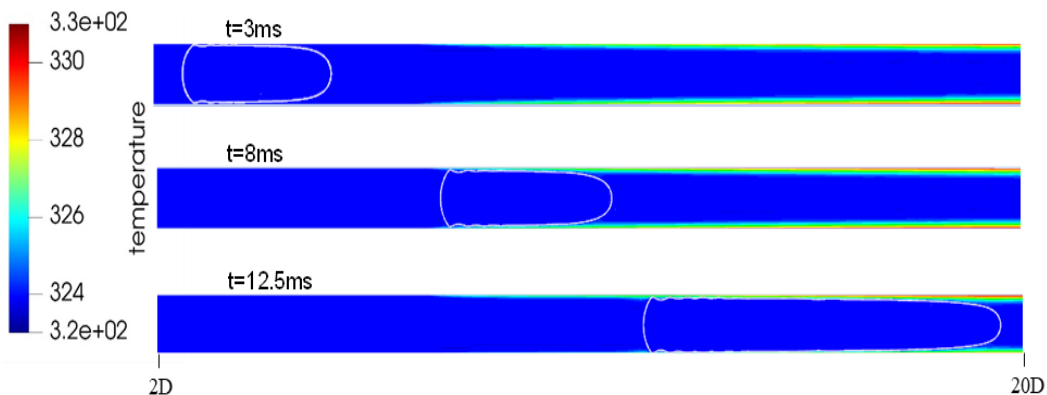

Figure 3-1: Temperature profile and position of the bubble (white outline) at various times (K)

The channel has a diameter of 0.5 mm, an adiabatic length of 4 mm and a heated length of 6 mm. The vapour slug is created by patching a 1.5 x 0.464 mm cylinder with rounded ends 0.5 mm from the inlet of the channel. The inlet has a uniform mass flux of 600 kg/m^2, and the outlet has a constant pressure boundary. To initialise the system, a single-phase case is run until the velocity, temperature and pressure fields are developed. The bubble is then patched into the domain and the simulation is run for 12.5 ms. The position of the bubble (outlined in white), as well as the temperature in the channel at various times, is shown in Figure 3-1.

The fluid that was used in the mesh refinement and mass transfer benchmark tests, and the validation case is the refrigerant R113, whose properties are presented in Table 3-1. The properties are kept constant throughout the simulations.

Table 3-1: Properties of R113 (adapted from Ferrari et al., 2018)

Property	Dimensions	Value
Liquid density	kg/m^3	1 502
Vapour density	kg/m^3	8
Liquid viscosity	μPa.s	477
Vapour viscosity	μPa.s	10.4
Liquid-specific heat	J/kg.K	943
Vapour-specific heat	J/kg.K	695
Liquid conductivity	mW/m.K	63.2
Vapour conductivity	mW/m.K	9.62
Saturation temperature	K	323.15
Surface tension	N/m	14.4
Latent heat capacity	kJ/kg	143.5

3.3. Mass transfer

3.3.1. Mass transfer model

The transfer of mass from liquid to vapour, and vice versa, is the most important aspect of this study. This transfer is what causes the boiling phenomenon and is why flow boiling offers such high heat transfer characteristics. However, correctly recreating mass transfer in a numerical simulation is incredibly difficult because the mechanisms that drive nucleation, coalescence, evaporation and condensation are not well understood. Therefore, only correlations and approximations based on experimental results can be used.

Three primary mass transfer models are implemented in most numerical studies (Kharangate and Mudawar, 2017). These models are the Rankine-Hugoniot jump condition, the Schrage model and the Lee model. These models are usually tweaked or simplified to better suit the study in question.

The default mass transfer model in Ansys Fluent is the Lee model, However, this is more of a macro-scale model and induces phase change throughout the liquid domain. To focus the evaporation at the interface, the Schrage model was chosen as the basis for the mass transfer model. Many previous studies, such as Ferrari et al. (2018), Liu and Palm (2016) and Magnini and Thome (2016a), have used a variation of this model and have all reported a similar phenomenon, that mass transfer within the interfacial region causes instabilities with the advection of the volume fraction or the level-set method.

The Schrage model was first proposed by Schrage (1953), but the version that is used in this study was simplified by Tanasawa (1991). It was then used to generate the source term-based model by Hardt and Wondra (2008). The Schrage model is based on the kinetic theory of gases, and relates the transfer of mass to the difference in partial pressure across the interface, as well as an accommodation coefficient, ω, which is the ratio of excited molecules that cross the interface to the total number of excited molecules that strike the interface. The mass flux is given by:

$$\dot{m} = \frac{2\omega}{2-\omega}\sqrt{\frac{M}{2\pi R}}\left[\frac{P_g}{\sqrt{T_{g,sat}}} - \frac{P_L}{\sqrt{T_{L,sat}}}\right] \tag{3.10}$$

where ṁ is the mass transfer rate (kg/m³.s), M is the molecular mass (kg/mol), R_g is a gas constant and $\omega = 1$.

Tanasawa (1991) then simplified this by assuming that the mass flux across the interface is linearly dependent on the temperature difference across the interface and that $T_{g,sat}$ and $T_{L,sat}$ are both constant and equal. This mass flux was then found using:

$$\dot{m} = \frac{2\omega}{2-\omega}\sqrt{\frac{M}{2\pi R}}\left[\frac{\rho_g h_L (T - T_{sat})}{T}\right] \tag{3.11}$$

Once the mass flux is obtained, the mass transfer or source term is calculated as a function of the interfacial area:

$$S_g = -S_L = \dot{m}|\nabla\alpha| \tag{3.12}$$

where S_g and S_L are the mass source terms for the vapour and liquid phases, respectively.

The interfacial area term in Equation 3.12 is the magnitude of the gradient of the volume fraction, which ensures that evaporation only happens at the interface. In micro-scale flows, the tiny cell size focuses the mass transfer to a very small area, which can attempt to evaporate more liquid than exists in the cell and produces negative volume fractions.

This can interfere with the volume fraction advection equation, which makes the Tanasawa (1991) model, in its original form, inappropriate for micro-scale flow boiling (Kharangate and Mudawar, 2017).

Hardt and Wondra (2008) proposed a smeared source term model that would conserve the net mass transfer across the interface, but would limit the vapour and liquid source terms to the pure vapour and liquid domains, respectively.
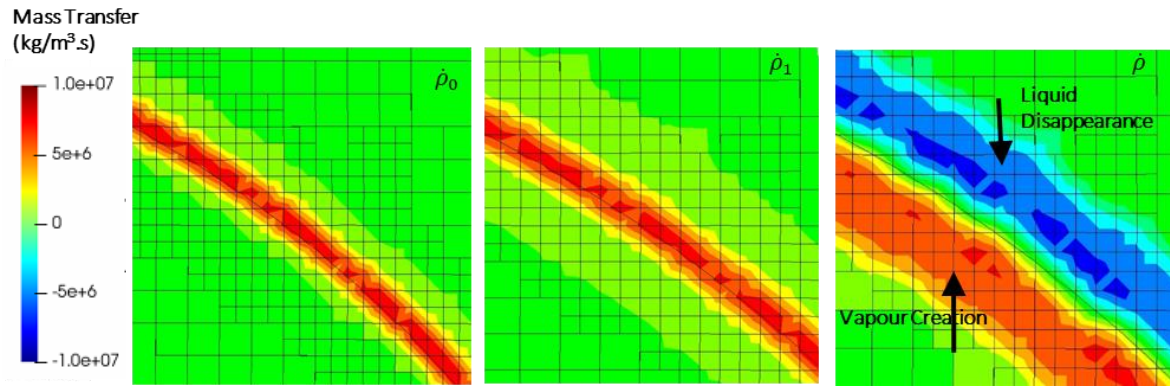
Figure 3-2: Mass transfer model with initial source term (left), smeared source term (middle) and implemented source term (right)

The smeared source terms are displayed in Figure 3-2, and the procedure for implementing the model is as follows:

1. The initial source term, which is shown in Figure 3-2 (left), is calculated using:

$$\dot{\rho}_0 = N_{to}\dot{m}\alpha|\nabla\alpha| \tag{3.13}$$

where $\dot{m}$ is first calculated using Equation 3.13 and where N_t is a normalisation factor to account for the multiplication of α into the equation, which shifts the source term more to the liquid side of the interface.

N_t is calculated using:

$$N_{to} = \frac{\int_V |\nabla\alpha|dV}{\int_V \alpha|\nabla\alpha|dV} \tag{3.14}$$

2. The initial source term, which only exists over the two to three cells of which the interface is comprised, is then smeared over a larger area so that three to four cells on either side of the interface contain a portion of the source term. The smearing is done via the following steady diffusion equation:

$$\dot{\rho}_1 = \dot{\rho}_0 + D\nabla^2\dot{\rho}_1 \tag{3.15}$$

Neumann boundary conditions are set on each boundary, which ensures that there is no discrepancy between the integral of the initial and smeared source terms. The Neumann boundary condition keeps the gradient of the scalars equal to 0 throughout the simulations. This ensures that the flux at the boundaries is equal to zero, or more specifically that none of the scalar is leaving the system. The smeared source term is shown in Figure 3-2 (middle).

3. With the source term smeared over the required area, it is then bounded on either side, as well as within the interface. If the term is within the interface or appears within cells that have not previously been refined, it is set to 0 in these cells. The final source term that is shown in Figure 3-2 (right) and that is implemented in Ansys Fluent is:

$$\dot{\rho} = \begin{cases} N_v(1-\alpha)\dot{\rho}_1 & if\ \alpha < 0.001 \\ N_L\alpha\dot{\rho}_1 & if\ \alpha > 0.999 \\ 0 & if\ 0.001 \le \alpha \le 0.999 \end{cases} \tag{3.16}$$

where N_v and N_L are normalisation factors that ensure that the volume integral of the vapour and liquid source terms is equal to the initial source term.

The normalisation factors are calculated using:

$$N_v = \frac{\int_{V_v} \dot{\rho}_0 dV_v}{\int_V (1-\alpha)\dot{\rho}_1 dV} \tag{3.17}$$

$$N_L = \frac{\int_{V_L} \dot{\rho}_0 dV_L}{\int_V \alpha\dot{\rho}_1 dV} \tag{3.18}$$

where N_v and N_L are the vapour and liquid phases, respectively.

4. When the source terms are implemented, mass disappears from the liquid phase and reappears in the vapour phase. However, the total enthalpy within these regions remains constant, resulting in a heating of the liquid and a cooling of the vapour regions. To account for this, as well as the enthalpy of formation, a source term is implemented in the energy equation, as follows:

$$\dot{h} = -\dot{\rho}_0 h_L + N_v(1-\alpha)\dot{\rho}c_{p,v}T - N_L\alpha\dot{\rho}c_{p,L}T \tag{3.19}$$

The mass transfer model is implemented in the UDF, which is provided in Appendix A.

3.3.2. Benchmark tests

The default mass transfer model for use with the VOF method in Ansys Fluent 19.1 is the Lee model, which gives the evaporation and condensation rates based on equations 2.23 and 2.24. This model is a macro phase-change model, which induces evaporation in any cells that contain liquid and are superheated, and condensation in any cells that contain vapour and are subcooled.

The mass transfer rate that is produced by this model is shown in Figure 3-3, which displays the slug as soon as it has reached the heated region.

As can be seen from Figure 3-3, evaporation occurs before the slug has even reached superheated liquid. The evaporation is also not limited to the vapour-liquid region, as is the case with the other models. Because mass transfer occurs in a region far from the interface, this model is deemed inappropriate for investigations into micro-scale flow boiling.

Mass Transfer (kg/m^{2}s)
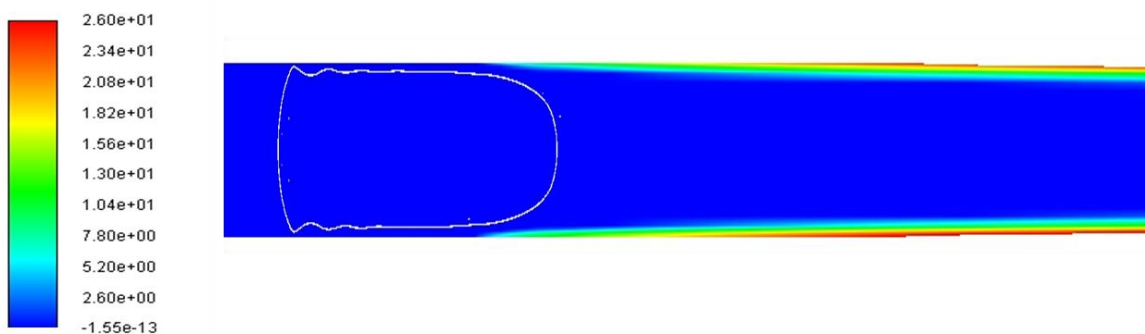
Figure 3-3: Mass transfer using the Lee model with the bubble profile outlined in white

To ensure that mass transfer is occurring within the interfacial region, the Tanasawa (1991)model is implemented rather than the default Ansys Fluent model. A UDF is written to implement the many steps that transform the original model to the smeared version.
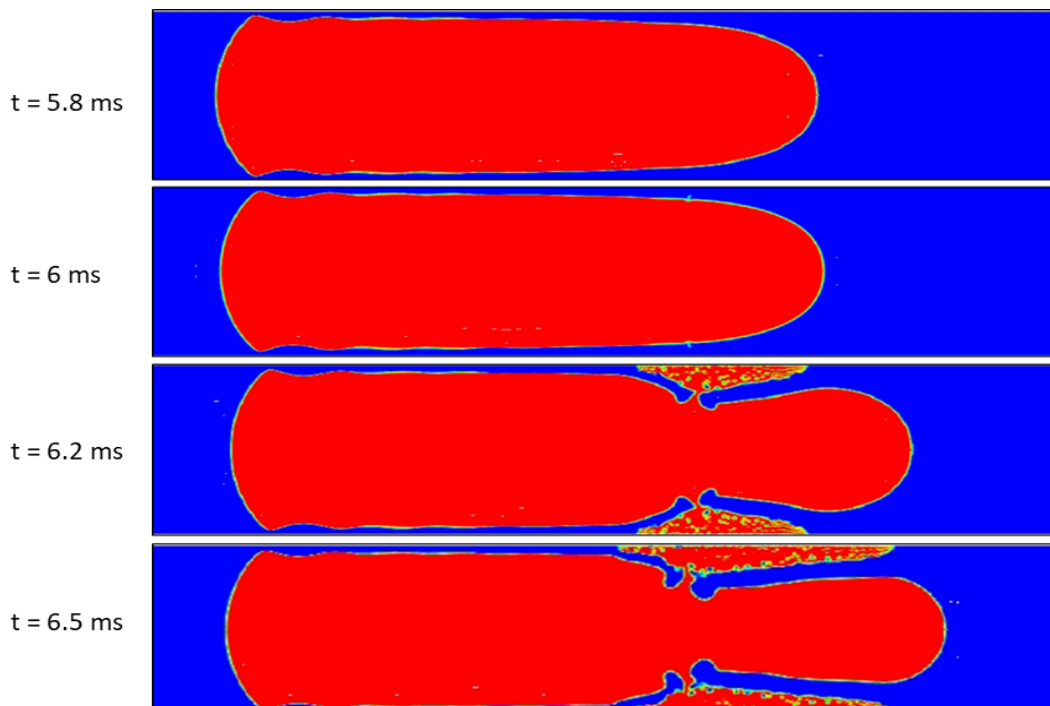
Figure 3-4: Vapour slug profile (red) as it enters the heated region from 5.8 to 6.5 ms without smearing the mass transfer

To demonstrate the importance of these steps, two initial simulations are performed. The first simulation involves using only Equation 3.13 to create the mass source term, and then implementing this directly into the liquid, vapour and energy source terms. The resulting bubble profile as the slug moves into the heated region is shown in Figure 3-4.

As soon as a part of the liquid-vapour interface becomes superheated, the interface breaks down, smearing towards the heated region. This phenomenon compounds on itself, resulting in a large region where the interface has broken down and surface tension pulls the vapour onto the heated surface. The results show the need for the mass transfer obtained in Equation 3.13 to be smeared over the interface.

The next simulation smears the obtained mass transfer and then implements this into the vapour and liquid mass sources. Due to the multiplication of the volume fraction into the source terms obtained from equations 3.13 and 3.15, vapour creation is proportional to the amount of vapour in the cell and liquid disappearance is proportional to the amount of liquid in the cell. However, Step 3, which sets mass transfer within the interface equal to 0, is not implemented.
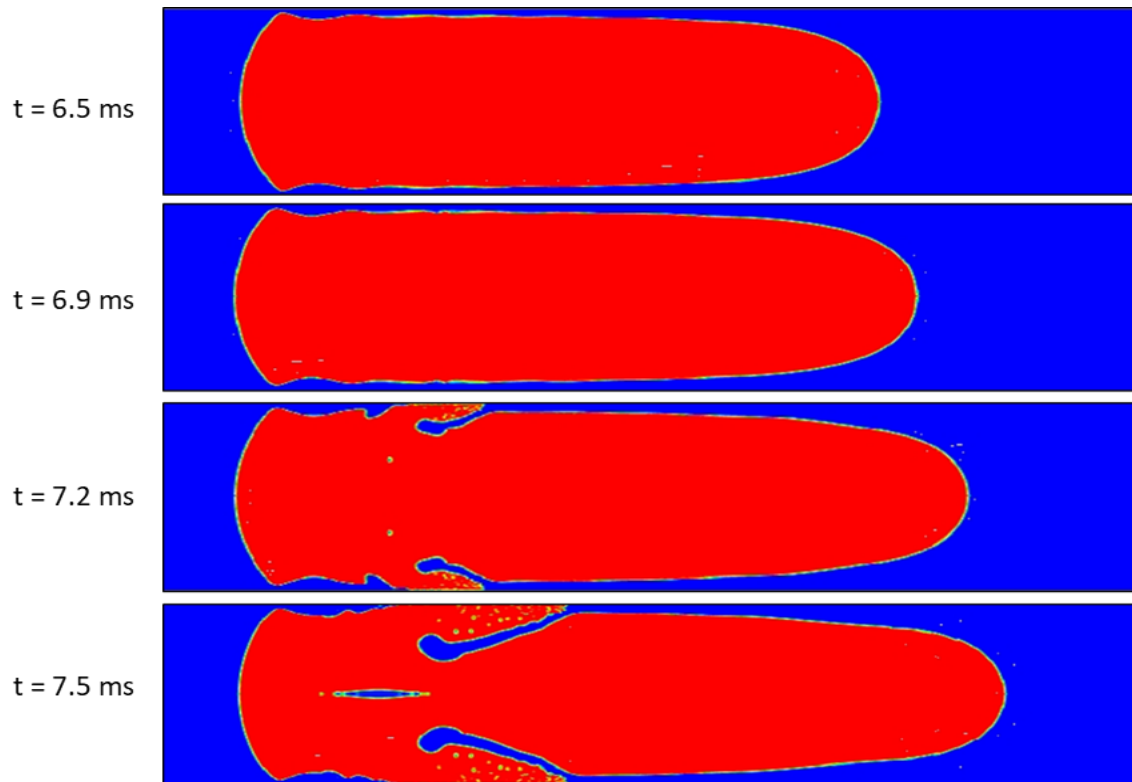
Figure 3-5: Vapour slug profile (red) as it enters the heated region from 6.5 to 7.5 ms without bounding the mass transfer

The resulting vapour slug profiles are shown in Figure 3-5. This mass transfer method retains the integrity of the slug longer than the non-smeared source term. However, the mass transfer within the interface introduces errors into the advection of the volume fraction. The surface tension keeping the bubble together breaks down, causing the vapour to migrate to the heated surface.

54

The results of these three simulations show how necessary the complex mass transfer model is. This model smears the initial mass transfer and then limits it to the pure liquid and vapour regions. The final mass transfer model is implemented for the mesh refinement, bubble detachment, validation and 3D cases.

3.4. Adaptive mesh refinement

3.4.1. Adaptive mesh refinement model

The division of the domain of interest into a collection of small elements or nodes is one of the most influential aspects of a CFD solution. The accuracy of the solution is highly dependent on the resolution of the mesh because the properties of each element are uniform. Therefore, small changes cannot be properly captured by a mesh with large elements.

The simplest form of mesh is a structured mesh, which is similar to a Cartesian grid. The grid lines that originate from a face never cross each other, and grid lines from other faces cross each line only once. This allows each node to be identified by its position on its respective origin, similar to the Cartesian system. These grids are mostly used for simple geometries because complex geometries can cause concentrations of cells that produce incredibly small elements with low qualities, which can be a waste of resources and can decrease the accuracy of the solution (Ferziger and Perić, 2002).

Unstructured grids are more popular for complex geometries because the elements can be of any shape or size and there is no restriction on the distribution of the elements. Unstructured grids offer more freedom, but the difference in the shape and size of neighbouring elements can cause numerical errors and increase the time required for creating the mesh and solving the problem (Ferziger and Perić, 2002).

Because of the effects that different meshes can have on a solution, an investigation is usually required to ensure that the mesh in use is accurately capturing the solution. One method of ensuring that the mesh is not influencing the solution is the Grid Convergence Index (GCI) method (ASME, 2009). This method takes a chosen parameter, such as the exit temperature of the flow, for a number of different sized meshes with a constant refinement ratio in all directions. It then extrapolates the chosen parameter to its asymptotic range, or the value that the parameter would assume as the number of elements in the domain approaches infinity. If the value being produced is close to 1, it has reached its asymptotic range and is judged as being independent of the mesh.

Even if the elements in a mesh are small enough to provide an accurate solution, the shape of the elements can still cause significant numerical error. Many factors can affect the solution, such as the skewness, aspect ratio and growth rate of the cells. The measure of these aspects for each element is referred to as the quality, which is a useful parameter in the analysis of the origin of solution errors.

During each iteration of the computation, the problem is solved at each individual cell in the domain. This creates a dependence of the computational time or cost on the number of cells in the domain. To decrease the time that each iteration takes, the number of cells in the domain should be kept to a minimum. However, some areas of the domain might need a much finer resolution to keep up the accuracy of scenarios, such as the thin liquid film at the wall of a microchannel or the interface between liquid and vapour during bubble movement.

To increase the resolution around specific areas, adaptive mesh refinement can be performed. This method changes specific areas of the mesh at set intervals, either every couple of iterations or every couple of time steps.

The adaption method is based on the error that is expected to occur over the cell size and the gradient of the specific area. The expected 2D error is calculated via the equation:

$$|e_{i1}| = (A_{cell})^{\frac{r}{2}}|\nabla f| \tag{3.20}$$

where e is the associated error, A_{cell} is the area of the cell, r is the gradient volume weight and ∇f is the Euclidean norm of the gradient of the adaption metric.

The curvature option of the gradient adaption approach uses the second derivative of the target metric, and the iso-value version uses the metric itself.

The purpose of adaptive meshing is to reduce the expected error. From Equation 3.20, one can see that the variables that determine the error are the cell area and the gradient. The gradient cannot be changed without affecting the solution. Therefore, reducing the cell area is the best way to reduce the expected error. The default adaption procedure in Ansys Fluent can be based on several different parameters, such as pressure or temperature, but for two-phase flow simulations, the more common parameter is the gradient of the volume fraction, which refines cells that are within the interface. This method was used in studies performed by authors such as Fondelli et al. (2015).

Because of the spurious currents surrounding the bubble interface, which are characteristic of numerical investigations into flow boiling in microchannels, only refining the cells at the interface does not properly capture the mass transfer, temperature and velocity gradients. The mass transfer that is implemented is also smeared over three to four cells on either side of the interface, and it is imperative for this study that mass transfer only occurs within refined cells. It is therefore necessary to refine a set region on either side of the interface, which ensures that these gradients and mass transfer are captured and that the thin liquid film between the bubble and the wall is fully refined.

To ensure that the cells around the interface are fine enough to capture the solution and that refined cells that are no longer in close proximity to the interface are not unnecessarily inducing high computational costs, an execution command is used to implement the refinement every 10 time steps. The method

implemented in this study used a UDF to create a region around the interface that was refined to consistently have at least four cells on either side of the interface. This ensured that the spurious currents that exist around the bubbles, as well as the mass transfer, only occurred in refined cells. The number of refined cells on either side of the interface is referred to as δ_M and the refinement level is referred to as δ_L. The refinement level is the number of times each bulk cell is required to be refined before the elements within it are the same size as the cells at the interface. This refinement is displayed in Figure 3-6.


Before Refinement   After Refinement
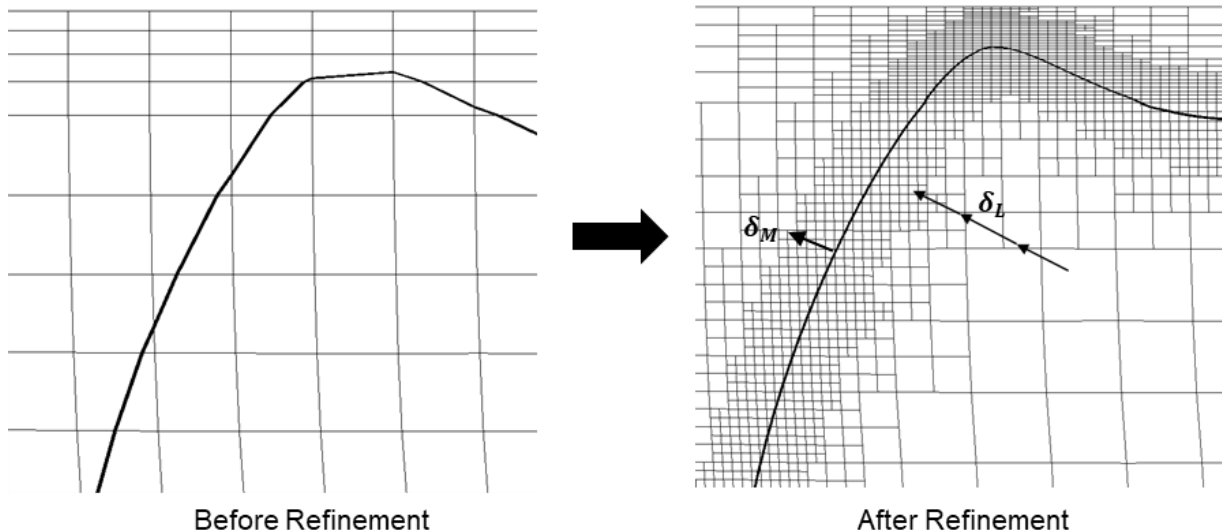
Figure 3-6: Mesh refinement area

Once the mesh has been refined, the size of the elements within the centre of the channel are squares with edge lengths of 3 μm, or $D_{min}/160$. The elements at the wall, which have several inflation layers applied, have one edge length of $D_{min}/160$ and one of $D_{min}/667$, or 0.75 μm. These cell sizes are determined by benchmark tests that are performed in the following sections.

3.4.2. Benchmark tests

Many variations of the mesh refinement model can be implemented. It is therefore necessary to perform several benchmark tests to ensure that the accuracy of the numerical model is upheld. The three major variables of this mesh refinement model are the level to which the cells at the interface are refined, the size of the area within which cells are refined and the size of the refined cells. The first two factors are investigated in this section, while the third is included in the validation section, where literature comparisons are performed.

The first factor under investigation is the level to which cells can be refined. Four benchmark tests are performed: one case is performed with $\delta_L = 0$ (all the cells are the same size) and three cases are performed with $\delta_L = 1$, 2 and 3, respectively. The refinement area is set to four cells on either side of the interface, which will be verified in the proceeding tests.

The most optimal ways of investigating the influence of these factors is to compare the resulting HTC of the heated surface at the end of the simulation, which is calculated using Equation 2.17, and by monitoring the location of the bubble throughout the simulation. The HTC at different mesh refinement levels is shown in Figure 3-7.
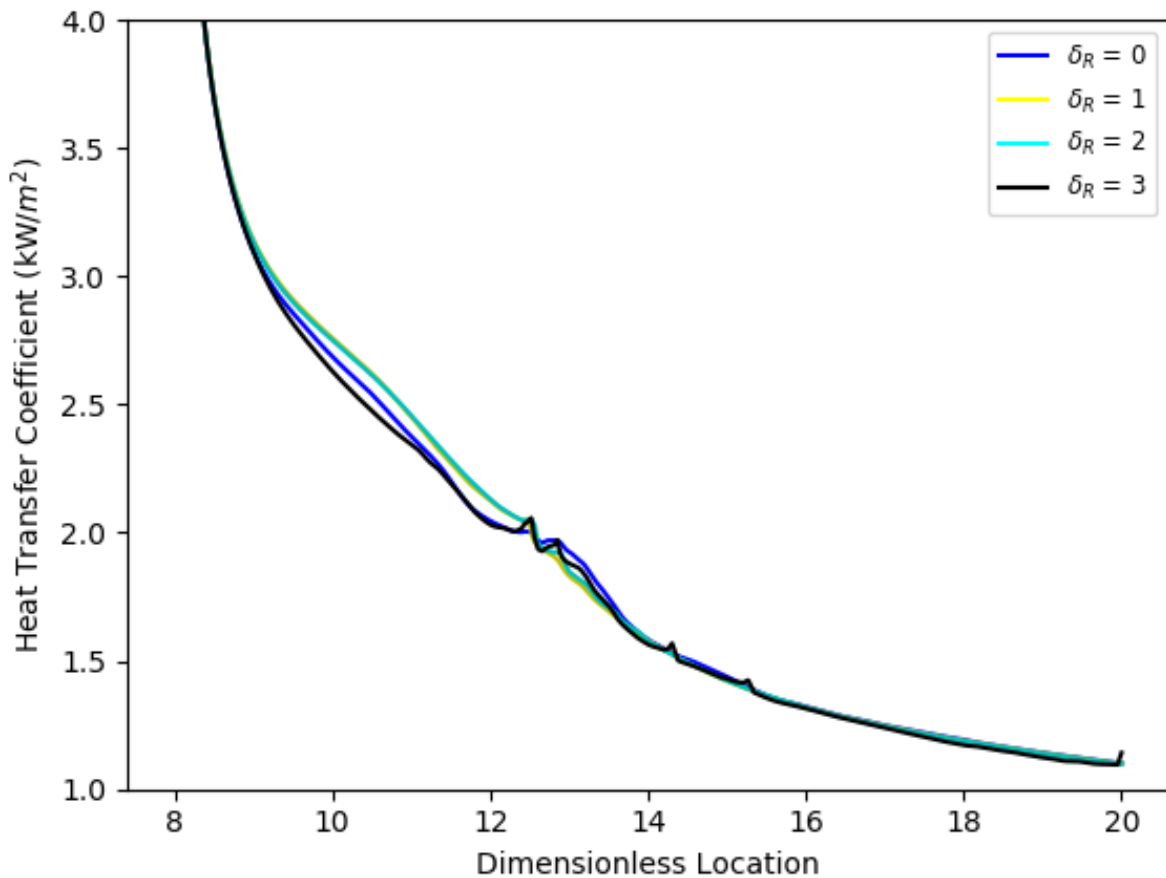

Figure 3-7: Heat transfer coefficient along heated length for different mesh refinement levels

Figure 3-7 shows that the HTC does not vary significantly as the refinement level is increased, with a maximum difference of 5.3% between $\delta_L = 1$ and $\delta_L = 3$. This difference can be explained by the way in which the mesh is generated, specifically the inflation layers. When the mesh with $\delta_L = 3$ is generated, there are five layers of inflation that smoothly grow to the size of the bulk cells. Once refined, the closest cell to the boundary is split into eight smaller cells. When recreating this inflation size without refinement, the constant growth rate of the cells requires either smaller cells to be used, or the growth rate to be slowed. The second option was chosen, which resulted in a less smooth transition from the inflation layer to the bulk cell size and only four minimum-sized cells at the interface instead of eight.

When analysing the temporal position of the slugs, a similar trend is displayed. Figure 3-8 shows the position of the front and rear of the slug vs time for each refinement level. The maximum difference between the cases is merely 2%, which shows that, at this mesh size, the solution is not altered significantly by coarsening the cells within the bulk flow.
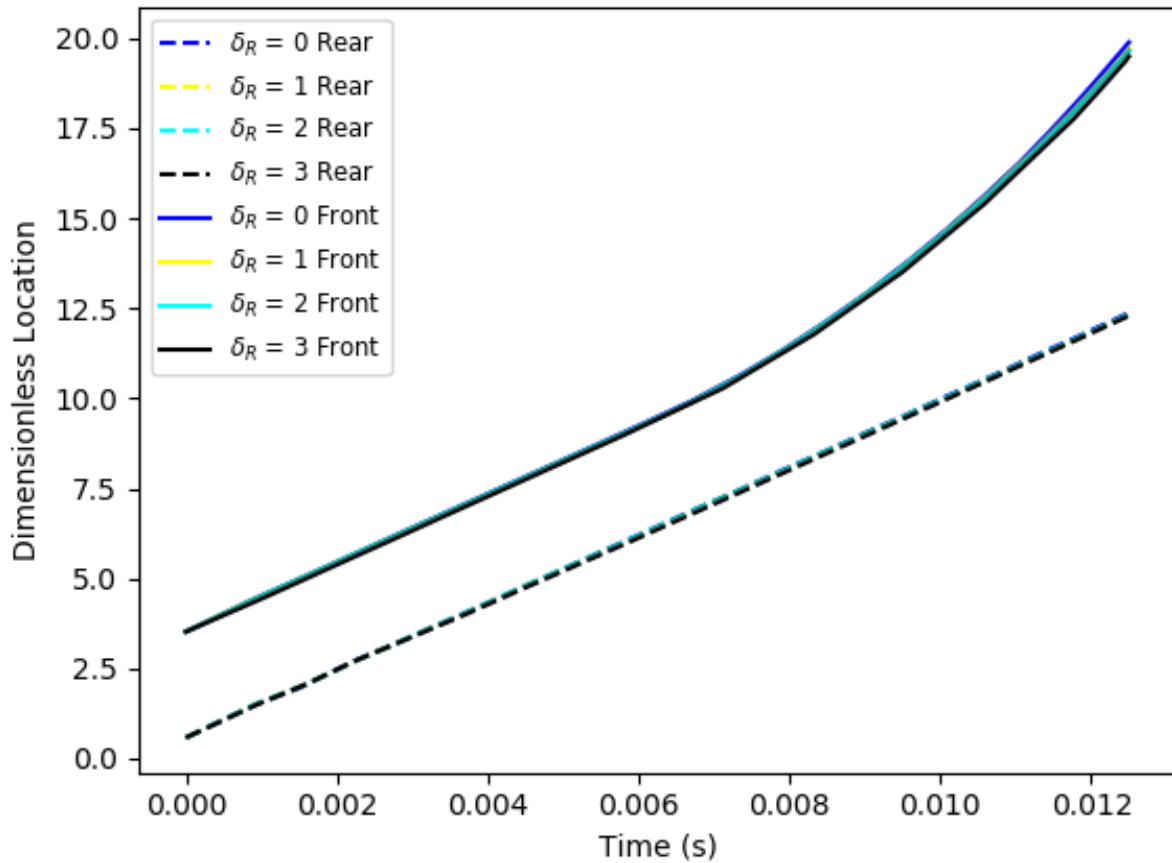
Figure 3-8: Dimensionless location vs time for different mesh refinement levels

The second benchmark test is performed to investigate the number of cells on both sides of the interface that are required to correctly capture both the spurious currents and evaporation/condensation that occurs within the region adjacent to the interface. Four tests are performed, the first of which involves only the cells within the interface being refined and none within the bulk liquid and vapour regions ($\delta_M = 0$). Three more tests with $\delta_M = 2$, 4 and 6, respectively, are then performed.

The first comparison between the cases is the HTC along the heated surface, which is displayed in Figure 3-9. The cases with $\delta_M = 4$ and $\delta_M = 6$ produced an HTC with very little error. However, as the number of cells is reduced to two, the HTC becomes larger and more erratic. This error is further enhanced once only the interface is refined, with the HTC of the $\delta_M = 0$ trial straying significantly from the other cases.
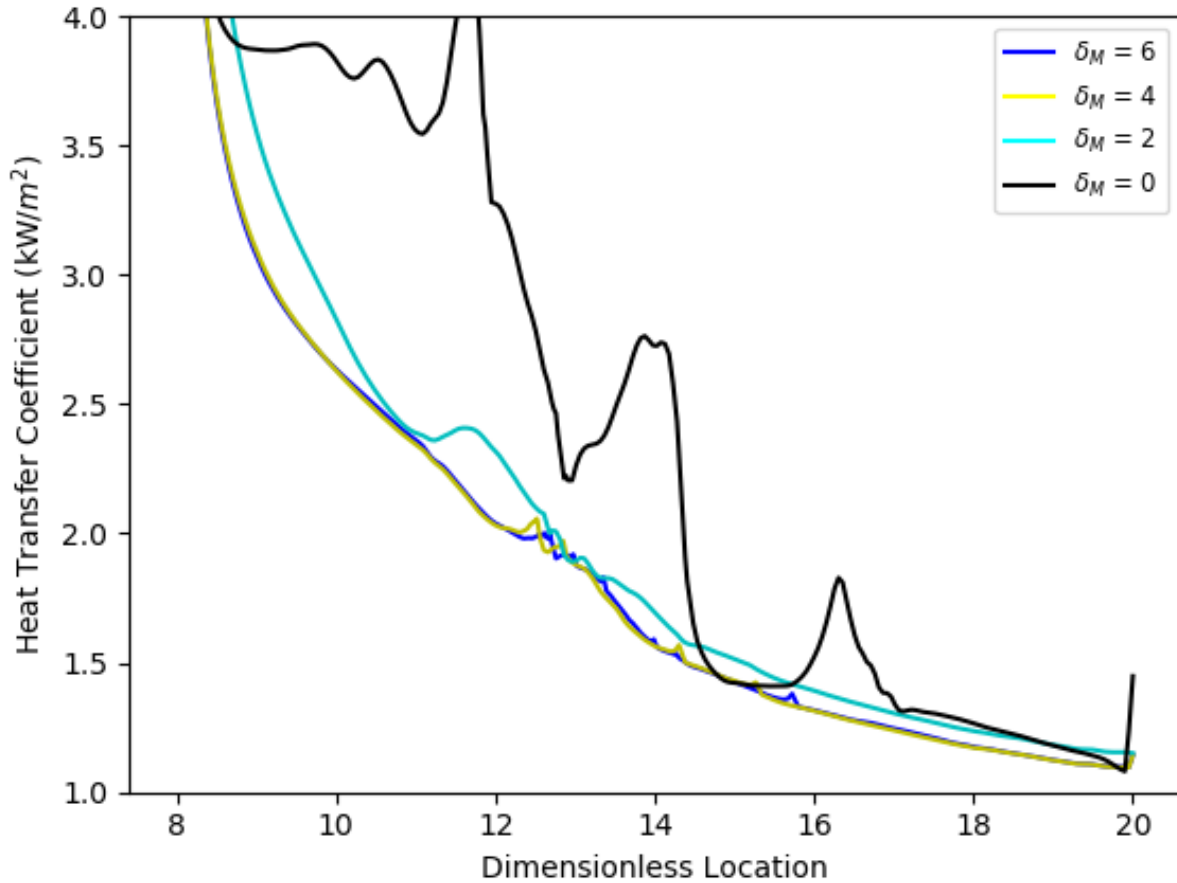
Figure 3-9: Heat transfer coefficient along the heated surface for different mesh refinement areas

This behaviour of the $\delta_M = 2$ case is not reproduced in Figure 3-10, with the difference in bubble position between meshes with $\delta_M = 2$, 4 and 6, respectively, being trivial. The case with $\delta_M = 0$, however, strays significantly, with the rear of the bubble falling behind, and the front of the bubble leaving the domain at 11 ms. The cause of these inconsistencies, shown by the $\delta_M = 0$ case, is that the interface is constantly travelling out of the refined area and into larger cells. After 10 time steps, a large portion of the interface has moved into large cells where information is lost due to decreased cell density. Once the mesh is refined, this information is not regained, but lost as the newly refined cells are given the value of their parent cell. The overestimation of the HTC of both the $\delta_M = 2$ and $\delta_M = 0$ cases is because mass transfer occurs in the three cells surrounding the interface. Therefore, some mass transfer occurs in cells that are too large and therefore overestimate their magnitude.

Dimensionless Location vs Time
For Different Mesh Refinement Areas
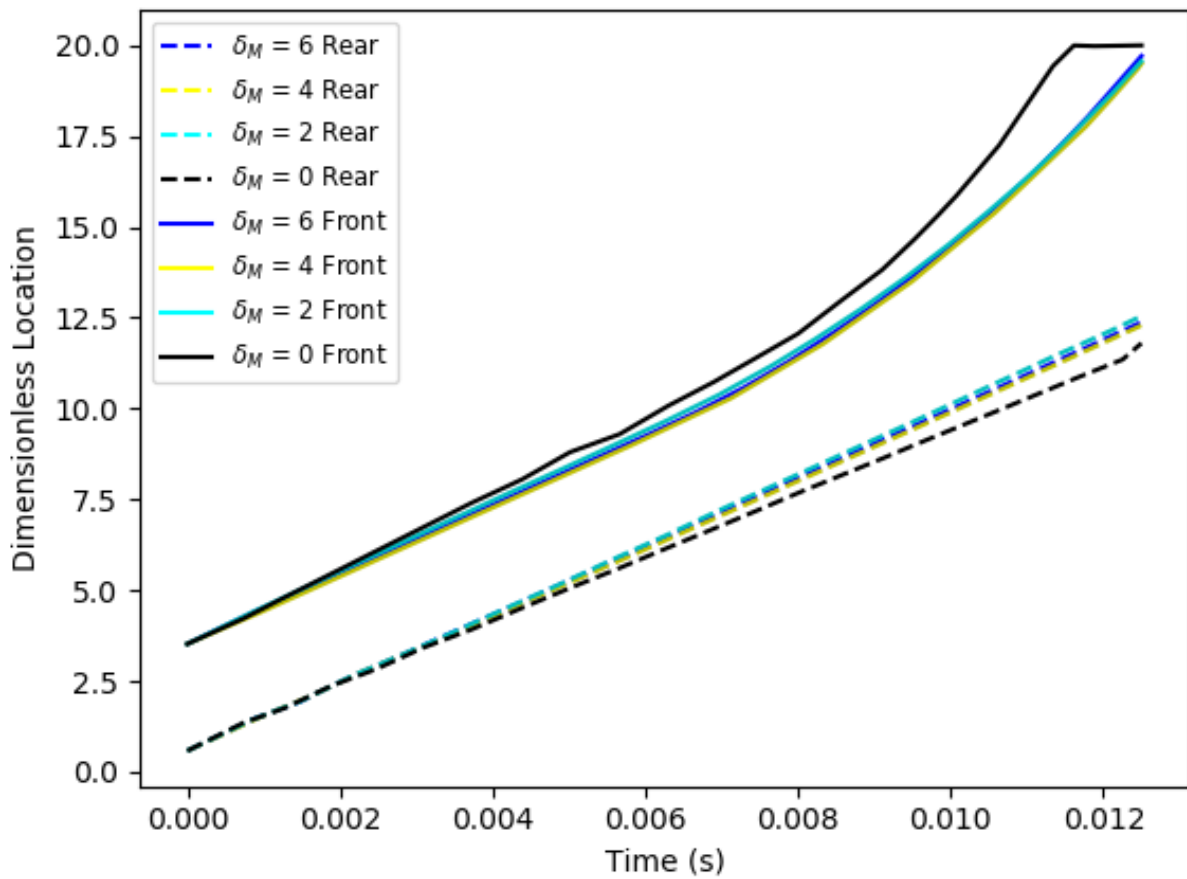
Figure 3-10: Dimensionless location vs time for different mesh refinement areas

Another effect of the interface moving in and out of the refined region is that the effects of surface tension can no longer be replicated correctly, and interesting behaviour occurs. Figure 3-11 shows the bubble profiles of all four cases just after the bubble has entered the heated region and once the simulation has ended.
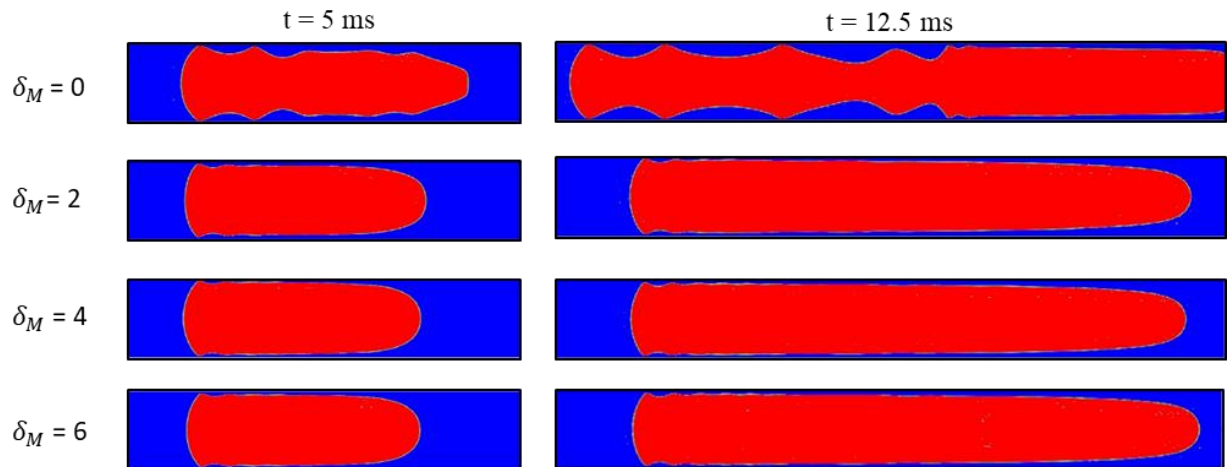
Figure 3-11: Bubble profiles at t = 5 ms (left) and t = 12.5 ms (right) for the zero-cell case, the two-cell case,
the four-cell case and the six-cell case

Figure 3-11 shows that the profiles of the $\delta_M = 2$, $\delta_M = 4$ and $\delta_M = 6$ cases are similar, while the profile for the $\delta_M = 0$ case is drastically different, with jagged edges and large, concave indents on the sides of the slug.

Figures 3-9 and 3-10 show that the mesh refinement model can maintain the original accuracy of a simulation, while reducing the cell density within the bulk liquid and fluid regions. The number of elements that made up the numerical domain at the beginning and end of all the benchmark tests is displayed in Table 3-2.

Table 3-2: Number of cells for each mesh refinement benchmark test

Case	Initial number of cells	Final number of cells
$\delta_L = 0$	327 232	327 232
$\delta_L = 1$	92 338	102 310
$\delta_L = 2$	31 513	43 933
$\delta_L = 3$	17 578	29 779
$\delta_M = 0$	8 665	12 628
$\delta_M = 2$	12 130	18 379
$\delta_M = 4$	17 578	29 779
$\delta_M = 6$	21 613	36 262

The case with the least number of cells that still retains accuracy has three levels of refinement ($\delta_L = 3$) and four cells on either side of the interface ($\delta_M = 4$). When comparing it to the case with $\delta_L = 0$, the simulation produces remarkably similar results, while using 91% less cells.

3.5. Verification and validation

Many assumptions are made and models used during numerical simulations. On top of this, the intrinsic nature of CFD codes introduces truncation errors via the mesh and discretisation methods that are used. While these are all necessary and unavoidable, the errors they produce should be limited so that the results produced are still valid. To ensure that the results have not strayed too far from physical reality, they can be compared to experimental data or other numerical studies, and if they match closely enough, they can be judged to still be valid. Different cases can then be simulated using similar meshes and models that will still produce accurate results.

To investigate the influence of the various factors of the numerical setup, such as the mesh, mass transfer model and discretisation methods, several axisymmetric cases have been performed with four different

mesh densities. These simulations form a numerical benchmark that is then compared with two previous numerical studies.

Four different mesh sizes are used, each with square bulk cells with five layers of inflation at the boundary, which are gradually refined until the cells at the boundary have an aspect ratio of 4. The meshes have initial bulk cell sizes of 50, 37.5, 25 and 17 µm, which, after refinement, are reduced to 6.25, 4.69, 3.13 and 2.13 µm, respectively. The thickness of the boundary cells, where most of the evaporation occurs, is reduced to 1.56, 1.17, 0.78 and 0.53 µm, respectively.
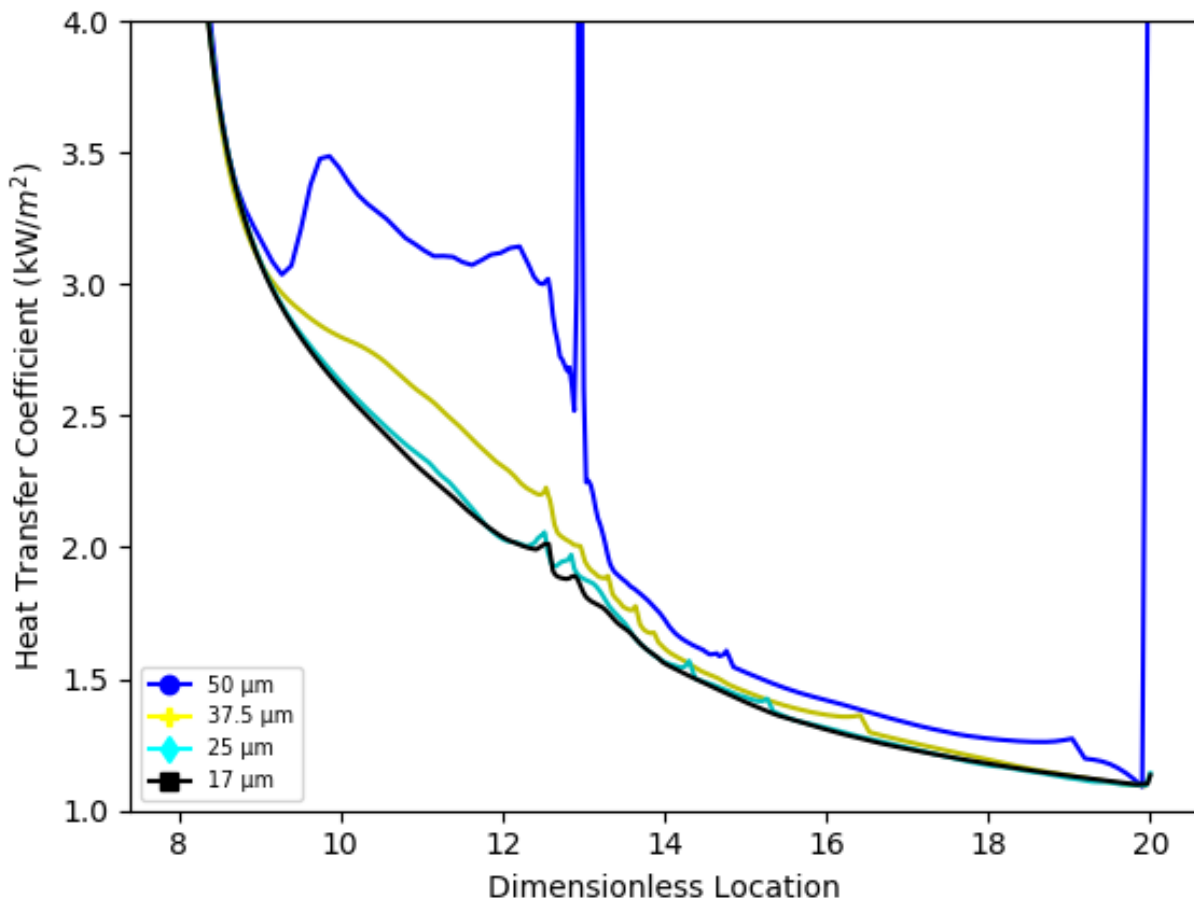
Figure 3-12: Heat transfer coefficient along the heated surface for different mesh sizes

The results of these simulations are presented in Figure 3-12 and Figure 3-13. Figure 3-12 shows the HTC, which is calculated using Equation 2.17, along the heated surface. The 50 µm case is much larger than the other cases and has uncharacteristic spikes, which shows that the elements are too large to correctly capture the effects of surface tension. Therefore, the liquid-vapour interface has ruptured, leading to small bubbles breaking off from the slug.

The case with a bulk mesh size of 37.5 µm retained the integrity of its liquid-vapour interface. However, the HTC was still too high due to an overestimation of the mass transfer source terms. The cases with element sizes of 25 and 17 µm produced an almost identical HTC, with a maximum difference of 4%.
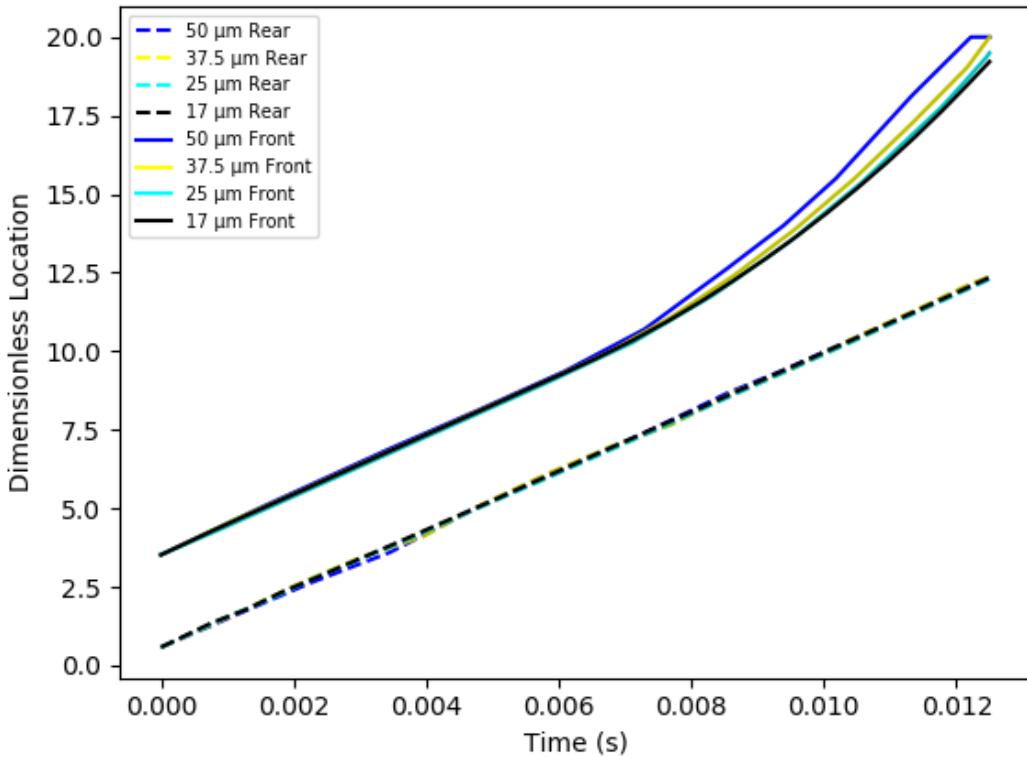
Figure 3-13: Dimensionless axial position vs time for different mesh sizes

The trends that are shown by the results presented in Figure 3-12 are supported in Figure 3-13, which shows the position of the rear and the front of the bubble at specific times. The rear of the bubble is in the same position for every case, which means that the liquid flow characteristics are correctly captured with every element size. However, when the front of the bubble grows faster, the cells are larger. The difference between the final position for the 25 and 17 µm cases is 1.5%.

To further test the influence of the mesh on the solution, the GCI method was implemented. The first step in this procedure is calculating the p value, which is described below:

$$p = \frac{\ln\left(\frac{f_3 - f_2}{f_2 - f_1}\right)}{\ln(r_f)} \tag{3.21}$$

where p is a GCI factor, f is the chosen metric, and r_f is the ratio of cell sizes between consecutive cases.

Next, the GCI values for each step (1 to 2 and 2 to 3) are calculated using the following equations:

$$GCI_{1-2} = \frac{F_s \left|\frac{f_2 - f_1}{f_1}\right|}{r_f^p - 1} \tag{3.22}$$

$$GCI_{2-3} = \frac{F_s \left|\frac{f_3 - f_2}{f_2}\right|}{r_f^p - 1} \tag{3.23}$$

64

Finally, the GCI value for the entire refinement is found using:

$$GCI = \frac{GCI_{1-2}}{r_f^p * GCI_{2-3}}$$

(3.24)

The values used for these calculations are presented in Table 3-3, and the results are presented in Table 3-4. The values used for each element size are the dimensionless position of the front of the bubble at 12 ms, which is taken from Figure 3-13.

Table 3-3: Values used in the GCI test

GCI term	Element size	Value
f_1	50 μm	19.55
f_2	37.5 μm	18.7
f_3	25 μm	18.3

Table 3-4: Results of the GCI test

Property	Value
r_f	1.5
p	1.86
Fs	1
GCI_{1-2}	0.019
GCI_{2-3}	0.04
GCI	0.99

This small magnitude of the difference in the HTC and bubble location, as well as the GCI value of 0.99, led to the conclusion that the solution is sufficiently independent of the mesh at 25 μm, Therefore, this is the bulk cell size that is used in the 3D simulations.

The HTC and the dimensionless bubble position are then compared with two published numerical studies that were performed on the same domain with similar solver settings, material properties, initial conditions and boundary conditions. The authors of the publications are Ferrari et al. (2018) and Magnini et al. (2013b).
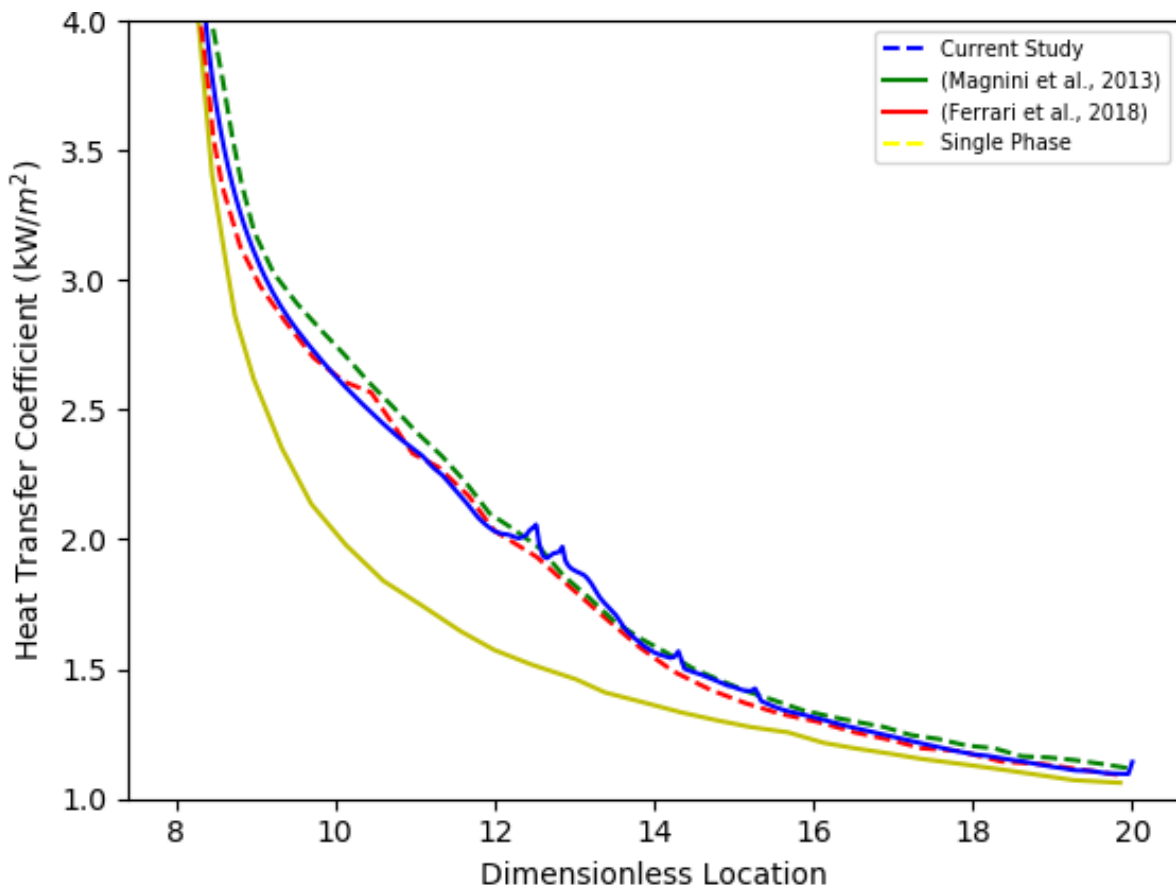
Figure 3-14: Heat transfer coefficient along the heated surface compared with previous numerical studies

The HTC produced by the current study matched both the profile and magnitude reported in both studies very closely. This is shown in Figure 3-14. The maximum error, when compared with the results of Magnini et al. (2013a), is 5.3%, and when compared with the results of Ferrari et al. (2018), it is 6.7%.

The dimensionless position of the rear of the bubble is similar for each of the cases. This is shown in Figure 3-15. This means that the flow characteristics of the liquid phase are fully captured. The final position of the front of the bubble is also very similar when compared with the results presented by both studies. The maximum error, when compared with the results of Ferrari et al. (2018), is 2.5%, and when compared with the results of Magnini et al. (2013a), it is 3%.
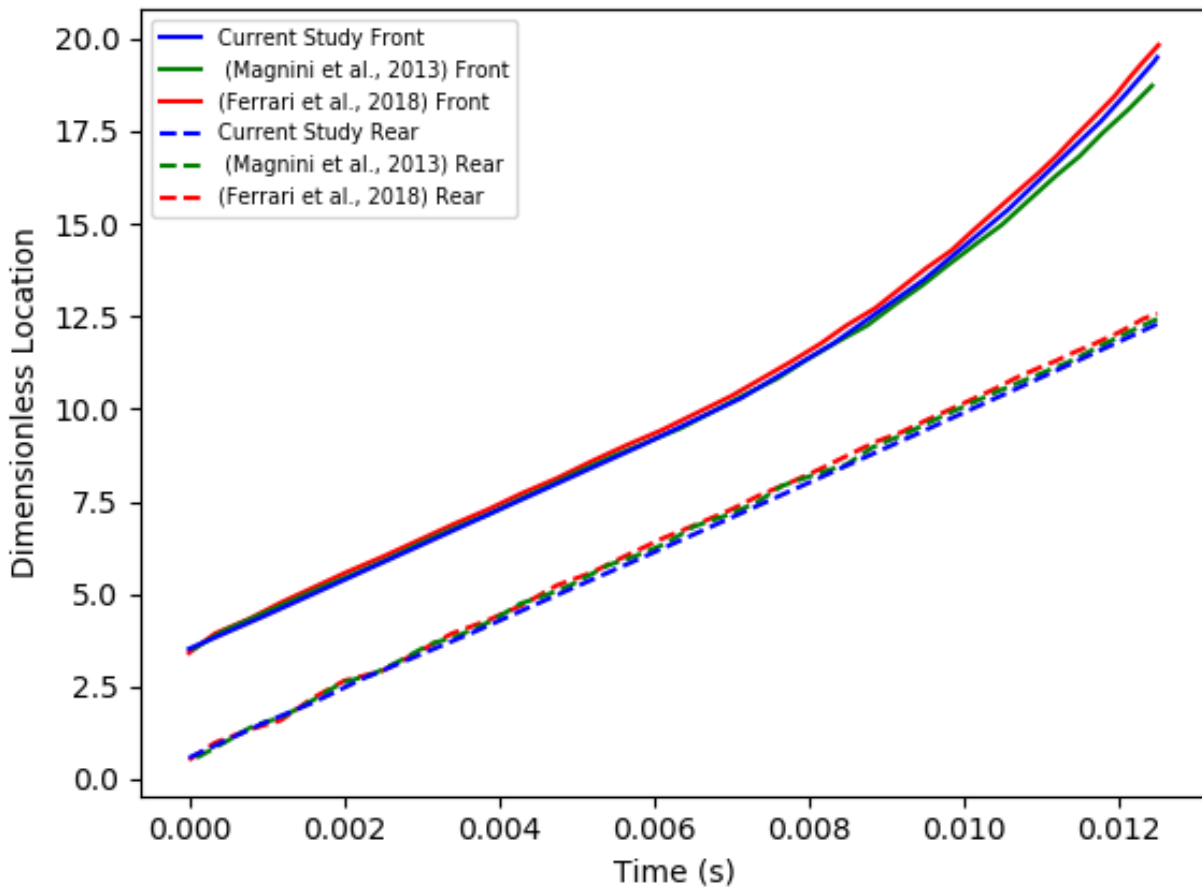
Figure 3-15: Dimensionless axial location vs time compared with previous numerical studies

The results presented in this section show that the results of the proceeding simulations are sufficiently independent of the mesh element size, and that the mass transfer model, solver settings and discretisation methods produce results that are validated against previously published numerical studies.

3.6. Conclusion

The governing equations, discretisation methods and solution procedure that are used throughout the simulations in this study are explained in this chapter, along with a thorough description of the mesh refinement model. Several benchmark tests were performed to investigate the extent to which the mesh refinement model can be altered, while still producing accurate results.

The results of the benchmark tests show that a minimum of four cells on either side of the interface is required to ensure that surface tension and mass transfer are correctly captured. The results also show that, if the interface and surrounding cells are kept the same size, the cells within the bulk liquid and vapour regions can be coarsened up to three times their original size without compromising the accuracy of the solution. The optimal refinement parameters have reproduced the results of an unrefined mesh using 91% fewer cells.

4. Results

4.1 Introduction

The primary aspect of flow boiling is the change of phase of the working fluid as it absorbs heat from the microchannel walls. Recreating this process using one of the many mass transfer models is a difficult process, as the movement of the vapour-liquid interface in combination with mass being transferred across this interface can introduce numerical instability into the governing equations of the system.

Implementing this numerical model while simulating flow boiling becomes even more difficult, as bubble growth on and departure from the heated surface introduces its own set of challenges. The phenomenon of bubble departure is not well understood, with the few departure models available relying on editing the applied contact angle to force bubbles to depart (Mukherjee and Kandlikar, 2007;Sanna et al., 2008).

The gravitational orientation is expected to influence the bubble behaviour due to the large difference in the Bo between the side-heated case and the top- and bottom-heated cases. Studies are usually based on circular channels, or if 3D, square channels. Therefore, the characteristic diameter that is used in the Bo is simply the hydraulic diameter of the channel. This ensures that the Bo remains constant through rotation. However, if the characteristic length is set as the length parallel to the orientation of gravity, the Bo changes significantly during rotation for microchannels with a high aspect ratio. This change in diameter alters the top part of Equation 2.12 to act as a hydraulic head.
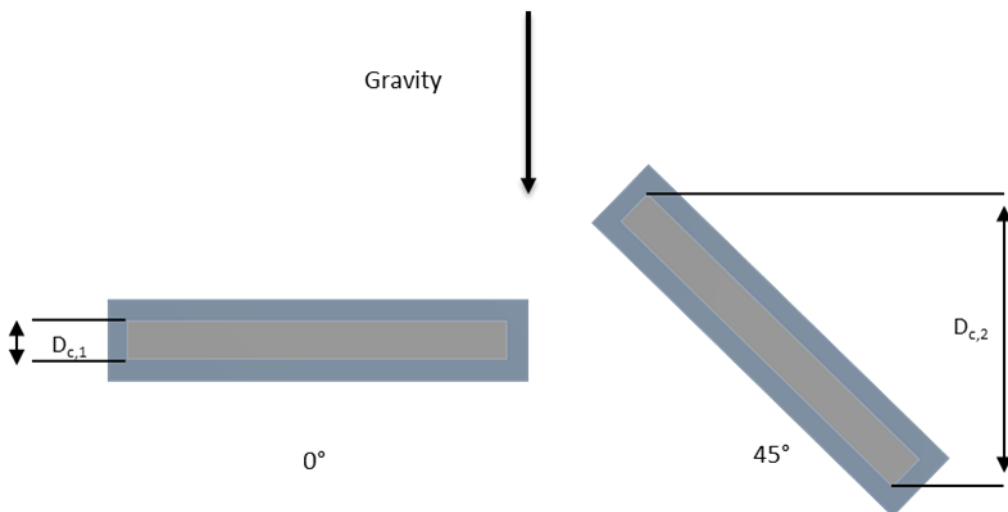
*Figure 4-1: Effect of changing angle on Bo*

Figure 4-1 shows the inlet of the microchannel in question, which has an inner height of 0.5 mm and an inner width of 5 mm. When the channel is rotated from $0°$ (flat) to $45°$, the diameter of the channel that is parallel to gravity changes from $D_{c,1} = 0.5$ mm to $D_{c,2} = 4.07$ mm. When using these diameters, the Bo for the respective cases becomes:

$$Bo_{c,1} = \frac{(\rho_L - \rho_v)gD_{c,1}^2}{\sigma} = \frac{(1620 - 13.4) * 9.81 * 0.0005^2}{0.00827} = 0.48$$

$$Bo_{c,2} = \frac{(\rho_L - \rho_v)gD_{c,1}^2}{\sigma} = \frac{(1620 - 13.4) * 9.81 * 0.004065^2}{0.00827} = 31.49$$

This shows that the same channel, when rotated, can be largely influenced by the orientation of gravity.

In the following chapter, the effects of both gravitational orientation and contact angle on the growth of a bubble in a microchannel will be investigated. Several cases will be performed in a 2D planar microchannel with a diameter of 0.5 mm. These cases will be used to investigate the effects of gravitational orientation and contact angle over a variety of different values. Two of these cases will be recreated in a microchannel with a height of 0.5 mm and a width of 5 mm. The effects of non-uniform confinement will be investigated, and the behaviour of the bubble will be compared to the 2D cases. A third 3D case will also be performed with different initial conditions, which is impossible to recreate in a 2D, planar domain.

4.2 Simulation setup and mesh generation

In this investigation, bubble growth is considered in a rectangular microchannel with a high aspect ratio at three different gravitational orientations. The domain that has been focused on is a small section of a larger microchannel that was used in an experimental investigation performed in conjunction with this study. The fluid, heat flux, mass flux and channel dimensions were the same as those used in the experimental investigation. However, only the length of the channel that underwent bubble nucleation was simulated. The position, size and contact angle approximations for each case were obtained from experimental results. The primary initial and boundary conditions of the simulations are shown in Figure 4-2.
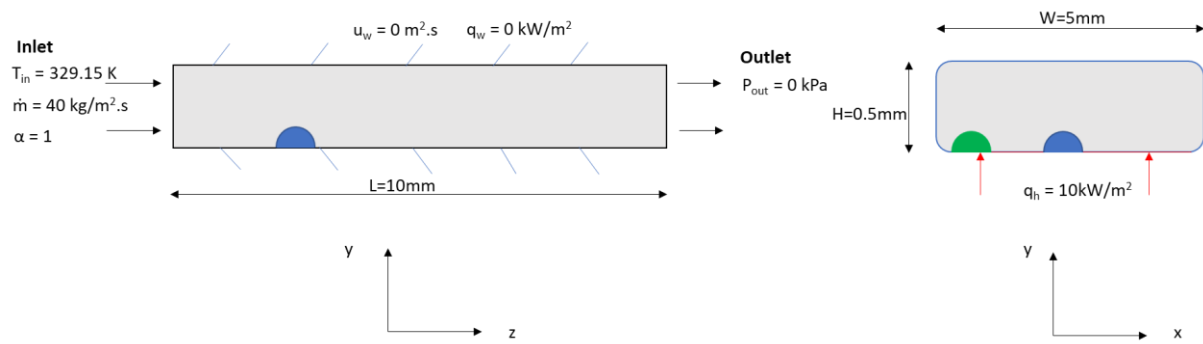

Figure 4-2: Primary initial and boundary conditions (not drawn to scale)

The mesh used for all three 3D cases is shown in Figure 4-3. The mesh utilised cubic bulk elements with an edge length of 25 μm, and seven inflation layers around the circumferential boundaries. The mesh had a minimum quality of 0.4, an average of 0.83 and a maximum aspect ratio of 4.
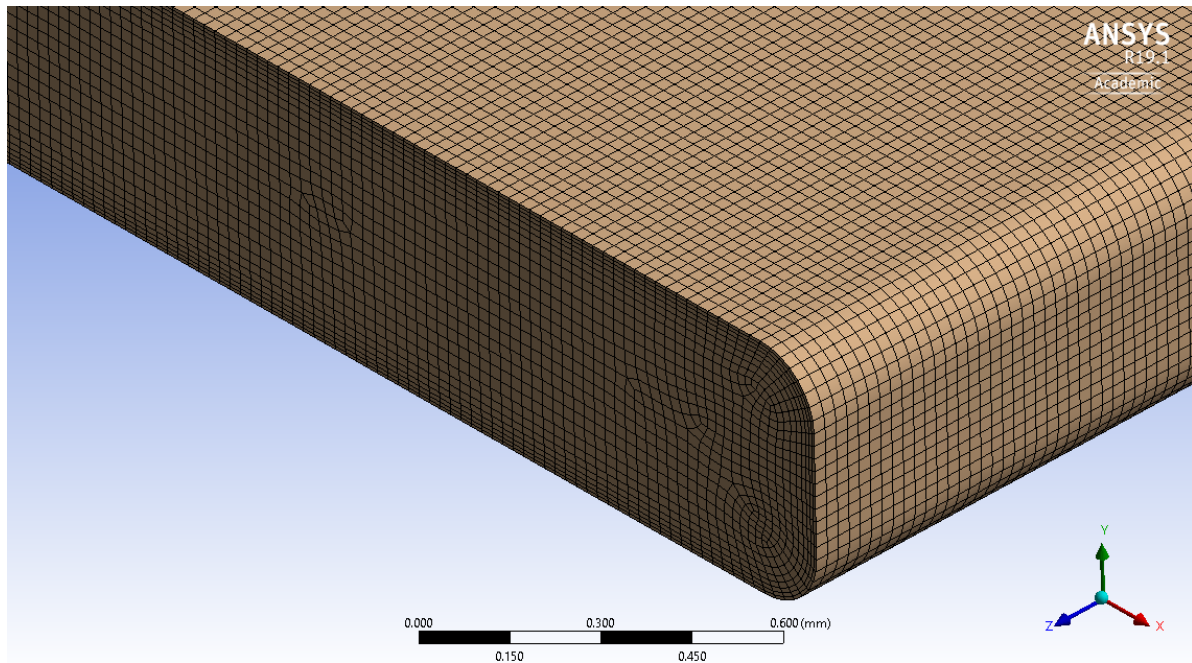
Figure 4-3: 3D mesh used for all cases

To obtain the initial velocity, pressure and temperature profiles, a single-phase simulation was performed. The VOF model was activated and a hemispherical bubble was placed on the heated surface of the channel. The nucleated bubble had a radius of 100 µm and was placed 1 mm from the inlet. For both the bottom- and top-heated cases, the bubble was placed in the centre of the heated surface, which is shown in blue in Figure 4-2. For the side-heated case, the bubble was placed on the side of the heated surface, which is shown in green in Figure 4-2. The temperature in the bubble was set equal to the saturation temperature, and the pressure in the bubble was set equal to 165.4 Pa higher than the gauge pressure at 1 mm from the inlet. The increase in pressure across the interface is calculated as follows (Ferrari et al., 2018):

$$\Delta P = \frac{4\sigma}{D} = \frac{4 * 0.00827}{0.0002} = 165.4 \, Pa \tag{4.1}$$

All simulated cases are idealistic models of flow boiling in a microchannel, with the domain, initial and boundary conditions selected to highlight the effect of gravitational orientation. This is done by varying the bubble location, gravity force vector and contact angle. Once these parameters are investigated in 2D, one top-heated, one bottom-heated and one side-heated case are simulated in the 3D domain. Both the bottom- and the top-heated cases had the same initial conditions, except for the contact angle. The bottom-heated case started with a contact angle of 45°. As the bubble grew and became confined, the contact angle was gradually reduced to 1°, which forced the bubble to detach. The contact angle reduction occurred when the bubble first became confined by the opposing wall and then became linearly reduced over the next 20 ms.

The side-heated case had the same contact angle as the top-heated case (60°), but the bubble was placed on the side of the channel. The bubble location was taken from the experimental results, in which case all nucleated bubbles and vapour slugs rose to the top of the channel in the X-direction due to the force of buoyancy (Meyer et al., 2020).

The material properties used during all the proceeding simulations are presented in Table 4-1. High temperatures are experienced on a small part of the heated surface during some of the simulations (Tsat +100 °C). However, the average temperature throughout the domain never exceeds Tsat +4 °C. At the maximum temperature, no properties vary by more than 30%. The mass transfer model, which drives the interface temperature to be as close to the saturation temperature as possible, the average temperature, the small change in fluid properties, as well as the nature of the study that focuses on buoyancy forces, as opposed to thermal gradients, led to the assumptions of constant liquid and vapour properties.

Table 4-1: Properties of FC-72 (adapted from Warrier et al. (2014) and 3M-Flourinert (2000))

Properties	Unit	Value
Boiling point	$^\circ$C	56
Latent heat	kJ/kg	88
Liquid density	kg/m^3	1680
Vapour density	kg/m^3	13.2
Molecular mass	g/mol	338.04
Kinematic viscosity	m^2/s	3.8×10^{-7}
Liquid-specific heat	J/(kg.K)	1 052.85
Vapour-specific heat	J/(kg.K)	895.2
Surface tension	N/m	0.00827
Liquid thermal conductivity	W/(m.K)	0.05725
Vapour thermal conductivity	W/(m.K)	0.0232

The solver settings and domain specifications used for each of the cases are shown in Table 4-2.

Table 4-2: Solver settings and domain specifications

Numerical simulation settings		
Property		**Specification**
Geometry	2D	0.5 x 10 mm
	3D	0.5 x 5 x 10 mm
Mesh	Elements	16014–45135 (2D) $2.51e^6$–$26.2e^6$ (3D)
	Maximum size	$2.5e^{-5}$ m
	Minimum size	$7e^{-7}$ m
	Minimum quality	0.4
	Average quality	0.83
	Maximum aspect ratio	4
	Adaption method	UDF
Solver	Type	Pressure-based
	Precision	Double
Multiphase	Model	VOF
	Interface	Sharp
	Evaporation modelling	UDF
	Volume fraction cut-off	1e-6
Turbulence	Model	Laminar
Boundary conditions	Inlet	$\dot{m}$ = 40 kg/m^2.s T = 329.15K,
	Heated surface	Heat flux = 10 kW/m^2
	Outlet	Backflow T = 329.15 K P = 0 kPa
Pressure-velocity coupling	Type	PISO
Discretisation	Pressure	PRESTO!
	Time	First-order Implicit
	Momentum	Second-order upwind
	Energy	Second-order upwind

Numerical simulation settings

Property	Specification	
	Volume fraction	Compressive/implicit
	User-defined scalars	First-order upwind
Initialisation	Method	Standard
	X-velocity	0 m/s
	Y-velocity	0 m/s
	Z-velocity	0.025 m/s
	Temperature	329.15 K
	Quality	0
Calculation	Flow time	0.065 (2D)
		0.058–0.072s (3D)
	Time step size	3e-7–1e-6
	Residual convergence	1.00E-04
		1.00E-06 (for energy)
	Maximum iterations/time step	40

The solver settings and discretisation methods presented in Table 4-2 are the same as those used in the validation cases. The dimensionless parameters that represent the system in question, which are calculated using the liquid properties, are presented in Table 4-3.

Table 4-3: Dimensionless parameters of the domain

Dimensionless parameter	Value
Re	57.4
Bo	0.48–47.64
Pr	0.007
Ca	101.89
We	0.115

4.2. Bubble departure model

The driving factor behind the detachment of bubbles from a surface is the imbalance of the forces acting on the bubble. In pool boiling, the forces of surface tension and bubble inertia attempt to keep the bubble fixed to the heated surface, while the buoyancy force attempts to remove the bubble.

However, when one looks at flow boiling, the inertia of the liquid flowing around the bubble also creates a force that attempts to remove the bubble. This force is strengthened when the flow is confined, and the bubble starts to fill most of the channel's cross-sectional area.

The diameter at which bubbles depart from a heated surface is of great interest to this study as experimental results by Meyer et al. (2020) have shown that bubble breakoff is the largest influence on the heat transfer characteristics of different channel rotations. The mass transfer model that has been implemented so far only affects the volume of vapour (the bubble size) and has no direct influence on whether the bubble will detach. Ansys Fluent has no model for bubble departure that can be used with the VOF model, with the only input being a static, uniform contact angle. This makes it necessary for a contact angle approximation to be developed that will simulate bubble departure. The default contact angle in Ansys Fluent is 90°. However, contact angles of 20 to 60° have been reported for a FC-72 bubble growing on a heated surface below it (Liu and Kim, 2017).

An experimental investigation on flow boiling, utilising the same working fluid, heat flux, mass flux and channel shape, was done in conjunction with this numerical study (Meyer et al., 2020). The initial experiments done on a bottom-heated case, a side-heated case and a top-heated case showed large differences between the behaviour of the nucleating bubbles. In these experiments, the bottom-heated case was shown to be the only one that demonstrated typical flow boiling characteristics, with bubbles regular growing, departing, joining the flow and eventually coalescing into slugs. The top- and side-heated cases had much lower bubble departure rates, with large plugs forming instead, which were eventually flushed from the channel.

Part of the process observed during a single bubble departure event that occurred in the bottom-heated case is displayed in Figure 4-4, which shows a bubble growing in front of a slug.
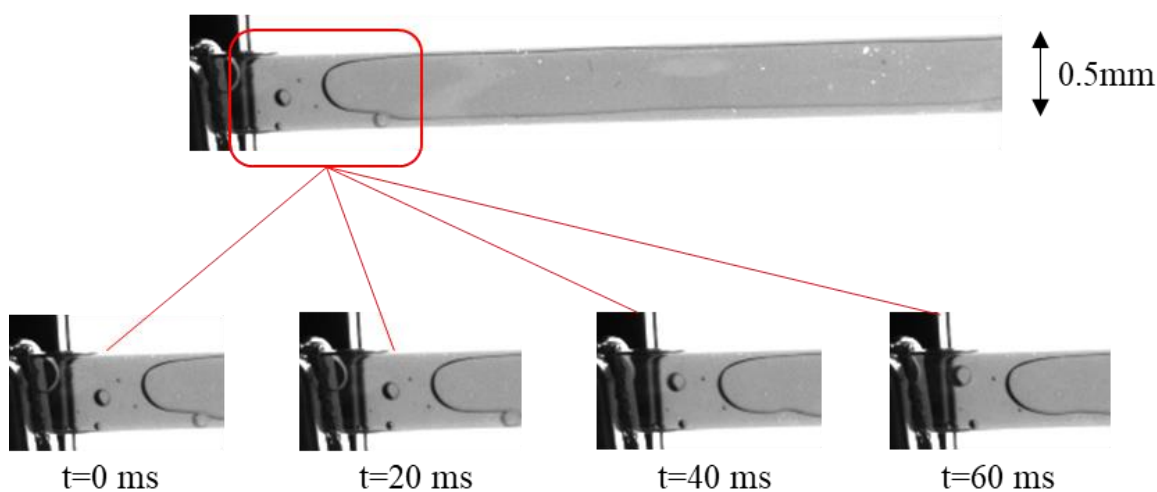

Figure 4-4: Detachment of bubbles during flow boiling (Meyer et al., 2020)

Once it reached the characteristic size, the liquid flow and the buoyancy force pulled it off the heated surface where it then joined the bulk flow and excited the channel or coalesced into larger slugs. Figure 4-4 shows the departure of a small bubble that has nucleated next to the slug. As the bubble has become combined with the upper wall, it stays in place from 0 to 20 ms. Then, from 20 to 40 ms, it departs from the wall and joins the flow, as can be seen at 60 ms.

The contact angle at the surface during flow boiling in a microchannel is incredibly difficult to measure due to the micro-scale size of the channel and the distortion of light through the glass. It is therefore simpler to judge the bubble departure criterion from experimental results and then to use this to create an approximate contact angle model for bubble departure.

As the bubble grows and buoyancy starts to take effect, the contact angle shrinks until it reaches its critical value. The method used to recreate this is similar to the procedure used by Sanna et al. (2008), which kept a constant angle for the initial growth stage. Once the bubble reaches a critical diameter, the contact angle is decreased to 0.1°, which forces the bubble to detach. Once the bubble has grown enough to reach the upper channel wall, it is large enough to become confined, and the contact angle will gradually be reduced. The effect of constant contact angles, a changing contact angle and the orientation of gravity will be tested in the following section.

4.3. Bubble departure benchmark tests

A series of benchmark tests in a 2D planar domain were performed to test the bubble departure model described in the previous section. The 2D axisymmetric domain used for the validation is transformed to a 2D planar domain with similar boundary conditions to the 3D case. This domain then represents a cut out down the central plane of the 3D domain, which results in a 0.5 x 10 mm microchannel. A bubble with a radius of 0.1 mm is initialised 1 mm from the start of the heated surface, and the fluid properties and initial conditions are the same as those used in the 3D tests. Eight simulations were then performed, four with gravity facing downwards and four with gravity facing upwards. In each gravitational case, the contact angle is set to 60°, 45° and 30°, respectively, and finally with a decreasing contact angle.

The aspects of the simulations that were analysed during the simulations are the total bubble area, the contact length between the bubble and the heated surface, the average temperature of the heated surface and the maximum temperature. While the surface tension of the bubble may not be correctly captured by a planar simulation due to its 3D nature, the results of this study will be beneficial as they highlight the extent to which the contact angle affects the behaviour of the bubble. Two of the cases were then recreated in 3D so that the effects of non-uniform confinement could be included in the simulations.

The area of the growing bubble for each of the cases is tracked and displayed in Figure 4-5.
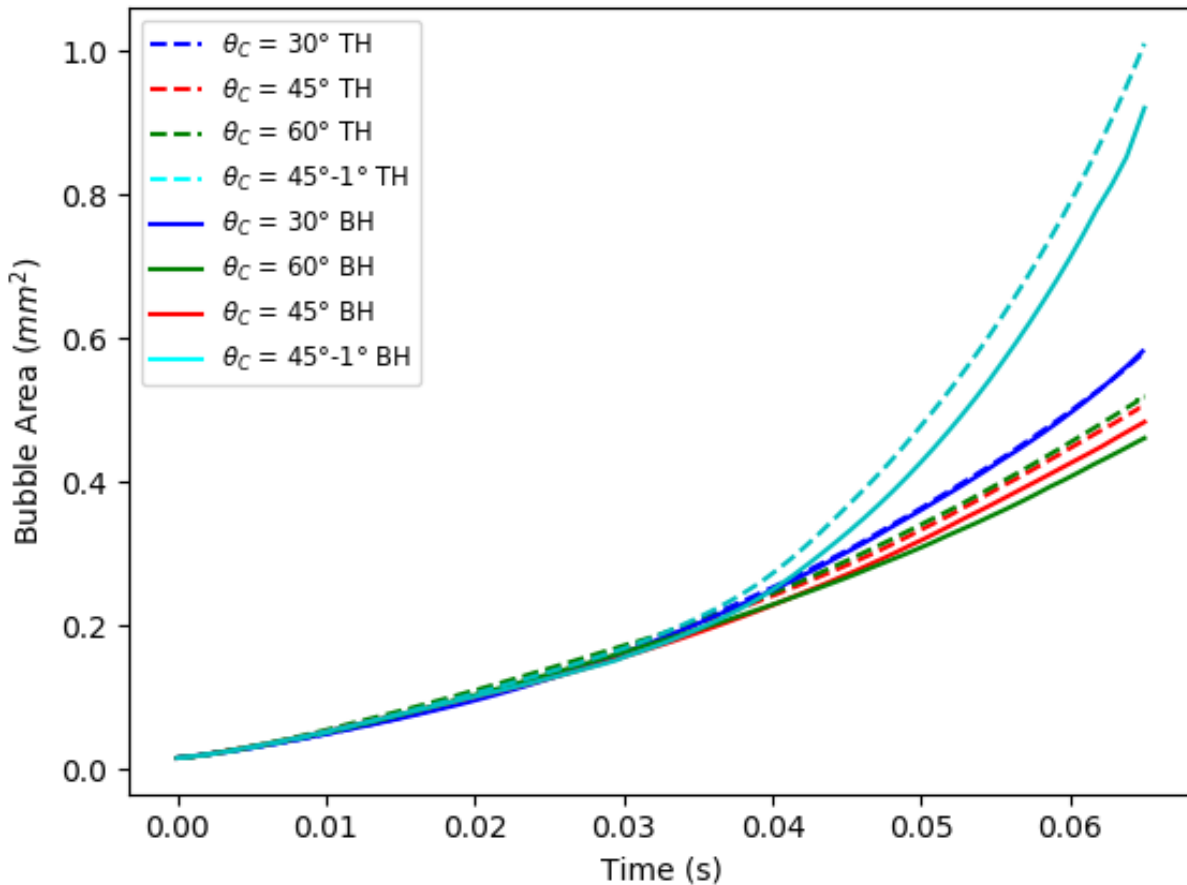
Figure 4-5: Bubble area vs time for the bottom-heated (BH) and top-heated (TH) cases at various applied contact angles

In all the cases with static contact angles, the bubble growth increases as the contact angle decreases. The bubble growth is also slightly higher for the top-heated case, but this difference is much smaller than with the different contact angles. The case that displayed the largest difference between bottom- and top-heated cases is the case with a decreasing contact angle. The bubble volume starts to differ once the bubble has detached from the wall, suggesting that the bubble growth during slug flow is higher for the top-heated case. The increase in mass transfer can be attributed to the difference in area adjacent to the heated surface, which increases as the contact angle decreases, as well as the force of gravity, which squeezes the bubble against the top wall, with the distance from the heated surface to the bubble interface in both the liquid and vapour regimes.

The difference in behaviour between the top- and bottom-heated cases becomes much more evident when the contact length between the bubble and the heated surface, displayed in Figure 4-6, is analysed.
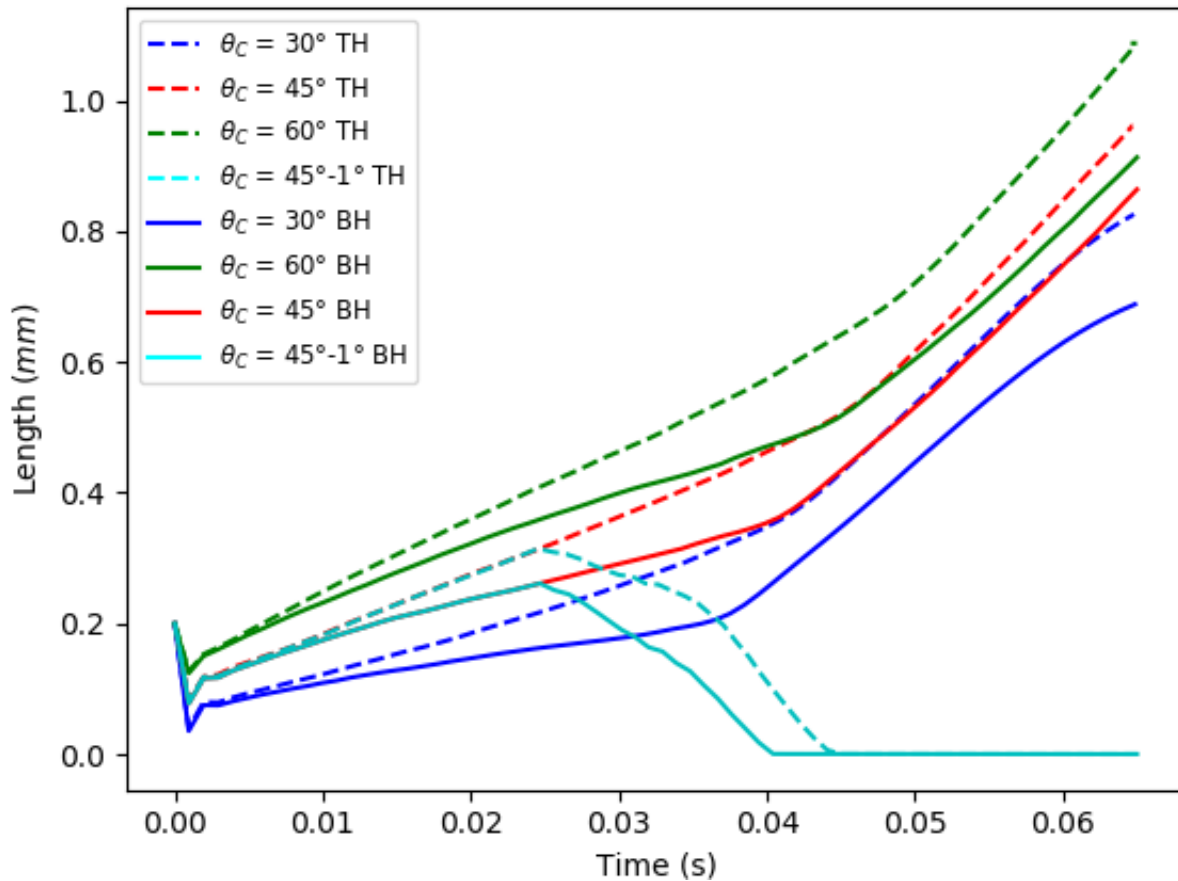
Figure 4-6: Contact length vs time for the bottom-heated (BH) and top-heated (TH) cases at various applied contact angles

From these results, one can see that gravity significantly affects the contact length between the bubble and the wall. The bubble departure, which is forced by reducing the contact angle, is clearly demonstrated in Figure 4-6. Both the bottom- and top-heated variable contact angle cases grow in a similar fashion to the constant contact angle cases. Once the contact angle has been reduced, the contact length between the bubble and the heated surface is reduced to 0, which indicates that the bubble has detached from the wall.

The effect of confinement on the bubbles is also evident in Figure 4-6, as the growth rate of the contact length between the bubble and the wall increases for all cases as the bubble fills the channel. The bubble then grows along the flow direction, increasing the area where evaporation can occur, while the distance from the heated surface to the bubble interface remains constant.

The detachment of the bubble is visualised in Figure 4-7, which shows both the bottom-heated 45⁰ and 45 to 1⁰ cases. The cases are identical at 16 ms. However, as the contact angle shrinks, the contact area decreases. This causes a larger portion of the interface to be exposed to superheated liquid, leading to a larger heat transfer. At 48 ms, the 45 to 1⁰ case has experienced detachment and has formed a liquid slug, the ends of which are both curved slightly upwards. At this stage, mass transfer occurs entirely from heat conduction through the thin liquid layer between the bubble interface and the heated surface.
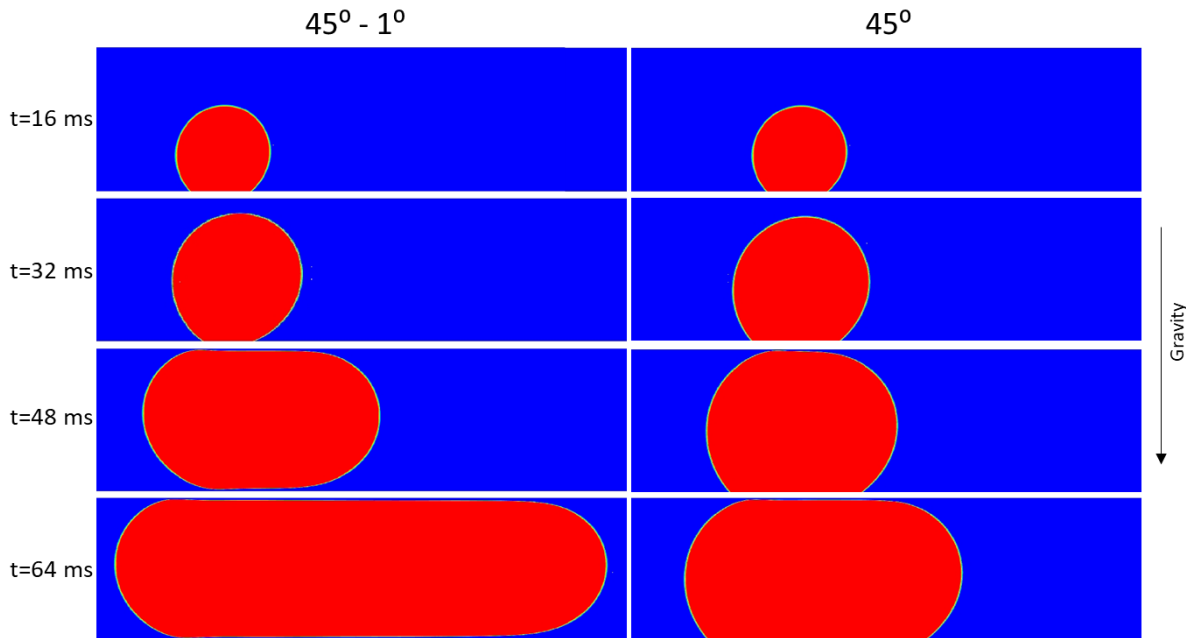
Figure 4-7: Visualisation of bubble detachment for the bottom-heated case

The heat transfer in the 45⁰ case is still dominated by the heat transfer that occurs in the region where the bubble interface is in direct contact with the heated surface. The magnitude of this mass transfer is higher, since the heat does not need to be conducted through any liquid. However, the interface area is much smaller, leading to a smaller overall mass transfer.

The effects of gravity and contact are not limited to the hydrodynamics of the system alone. Large differences are observed between the cases in Figure 4-8, which shows the maximum temperature of the heated surface, as well as in Figure 4-9, which shows the average HTC of the heated surface. When analysing both Figures 4-6 and 4-8, it is apparent that the maximum temperature in the channel is proportional to the contact length between the bubble and the wall, as any change in the contact length is mimicked almost identically by the maximum temperature. The heat that is transferred from the heated surface to the bubble interface radiates in all directions, and as the bubble grows, the distance from the centre of the contact region grows proportionally. The only case where the maximum temperature is not in this region is in the detachment cases. As soon as the bubble detaches, cool liquid is sucked beneath it, quenching the heated surface and moving the maximum temperature to the channel outlet, where it would be in a single-phase case.

The maximum temperature is affected largely by both the contact angle and the gravitational orientation. However, when the bubble becomes confined, the effect of gravitational orientation shrinks. The case that is affected the most is the 30⁰ case, with the temperature growth rate being much larger for the top-heated case for the first 40 ms. However, the difference between the two shrinks rapidly before plateauing once the difference between them is roughly half the difference at 40 ms.
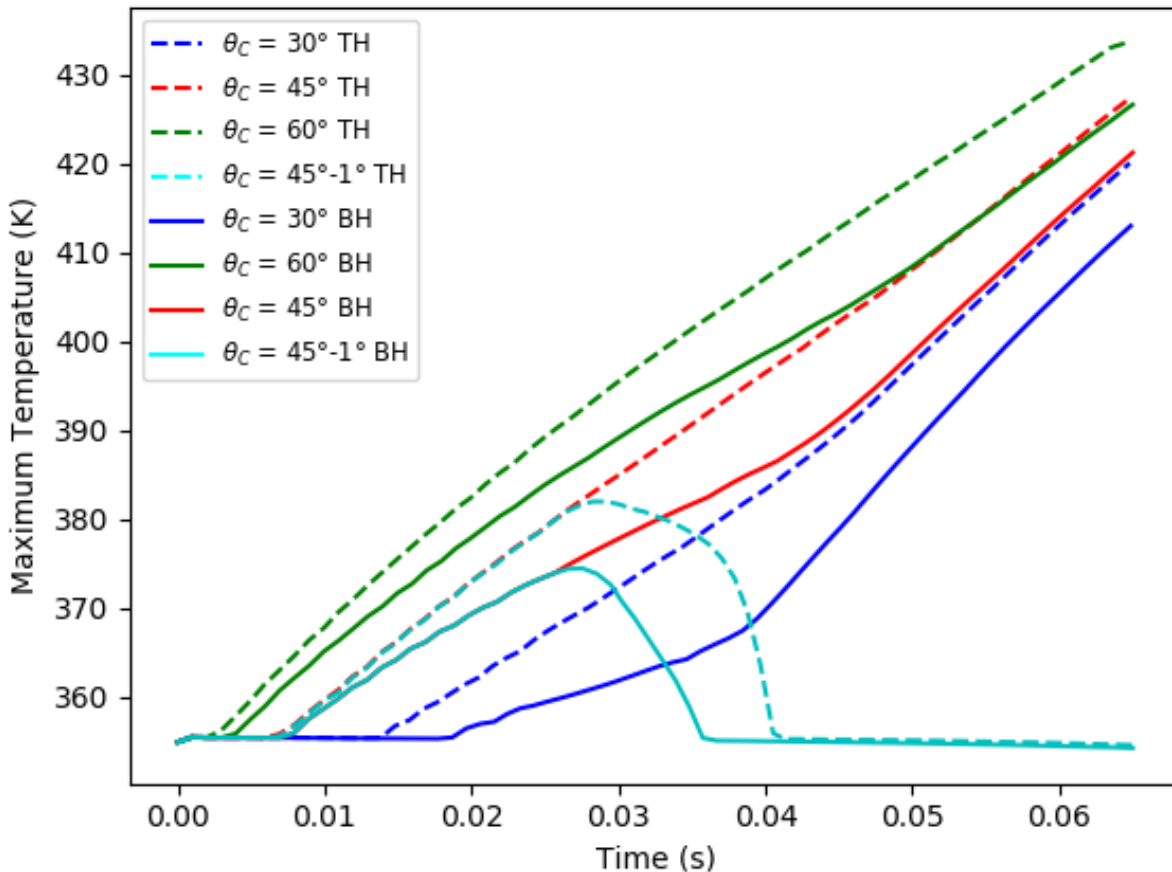
Figure 4-8: Maximum temperature vs time for the bottom-heated (BH) and top-heated (TH) cases
at various applied contact angles

The maximum temperature of the heated surface is an important aspect of any heat exchanger, as this temperature determines what materials can be used, if the heat exchanger can protect sensitive equipment and the safety aspects of the system. Another equally, if not slightly more important aspect is the average HTC, which determines the magnitude of the heat that can be removed by the heat exchanger per unit area.

The average HTC of the heated surface for each case is presented in Figure 4-9. As with the maximum temperature, the average HTC for each case is affected significantly by both the applied contact angle and the gravitational orientation. As the contact angle is decreased, the HTC increases, and each case is higher for the bottom-heated case, except for the bubble detachment case.
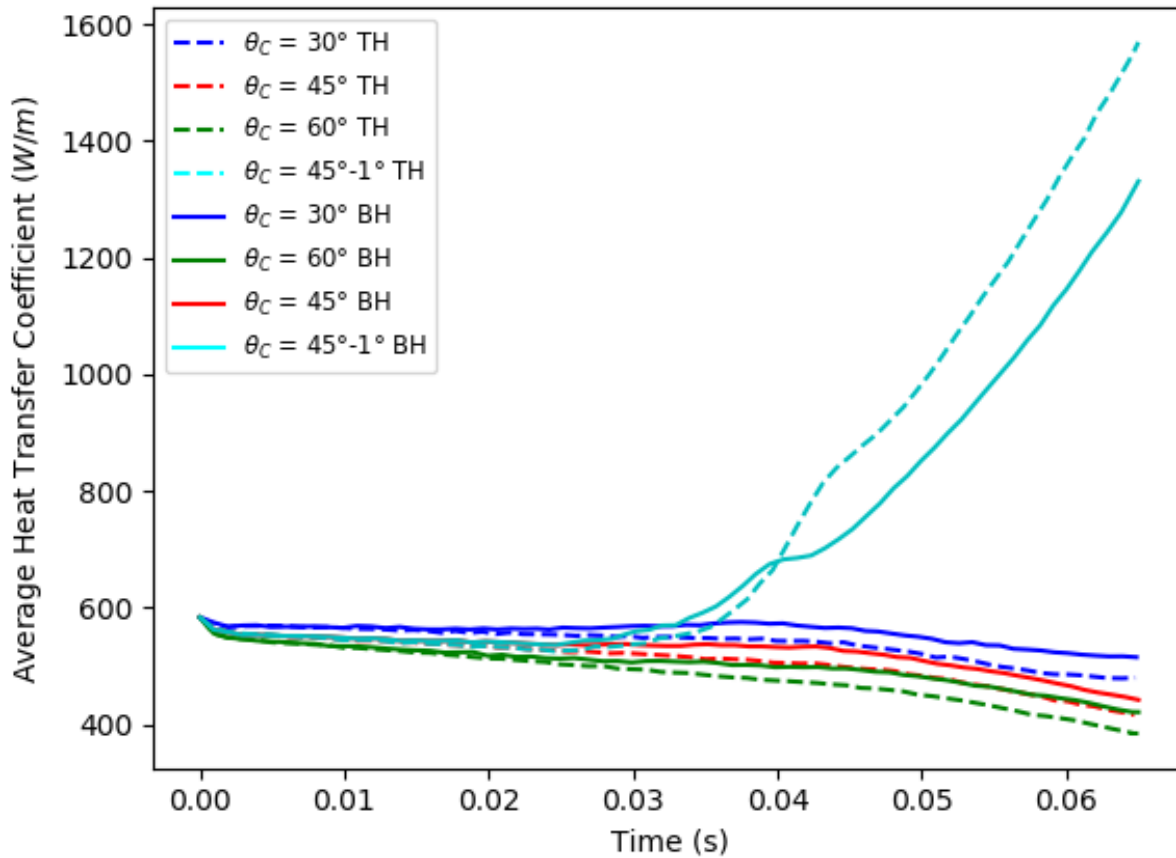
Figure 4-9: Average HTC vs time for the 2D bottom-heated (BH) and top-heated (TH) cases at various applied contact angles

The behaviour of the various constant contact angle cases are all pretty consistent, with a relatively steady decline in HTC as more vapour comes into contact with the heated surface. The vapour has a lower conductivity and a lower heating capacity, which requires higher temperatures to efficiently move heat away from the surface.

The exceptions to this behaviour are the bubble detachment cases, where the average HTC increases by over 100% as the cases grow in volume. These cases display three distinct regions. The first region is a slow, steady decline in the average HTC. As with the constant contact angle cases, the mass transfer, and therefore heat transfer, is dominated by the contact region of the bubble interface and the heated surface. The heat transfer increase provided by this contact area does not compensate for the increase in the vapour-heated surface contact area. Therefore, a higher temperature is required to provide the same heat flux.

The second region occurs once the bubble has begun to detach from the heated surface. As the contact angle shrinks, the contact area between the bubble and the wall recedes. This action creates a vacuum where the bubble was, sucking cooler liquid from the bulk flow into this vacated region. This sudden influx of liquid quenches the heated surface, dramatically reducing its temperature. This causes the average HTC to grow rapidly.

The HTC of the bottom-heated case, which has been higher than the top-heated case up to this point, is overtaken. The top-heated case had a larger vapour-heated surface contact area, which meant that a larger area could be quenched by the cooler liquid.

Once the bubble has detached and the quenching process has occurred, the third region begins. In this region, the heat and mass transfer are dominated by conduction of the heat from the heated surface through a thin liquid layer and into the liquid-vapour interface. The rate of increase of the HTC slows down for both cases, but the HTC of the top-heated case remains higher with a slightly larger rate of increase, which is due to the buoyancy force pushing the bubble up against the surface. This increases the area of the bubble that is adjacent to the heated surface and decreases the thickness of the liquid film between the bubble and the heated surface. Figure 4-10 shows the slug for each case at t = 48 ms, where the difference in bubble shape and location can be seen.
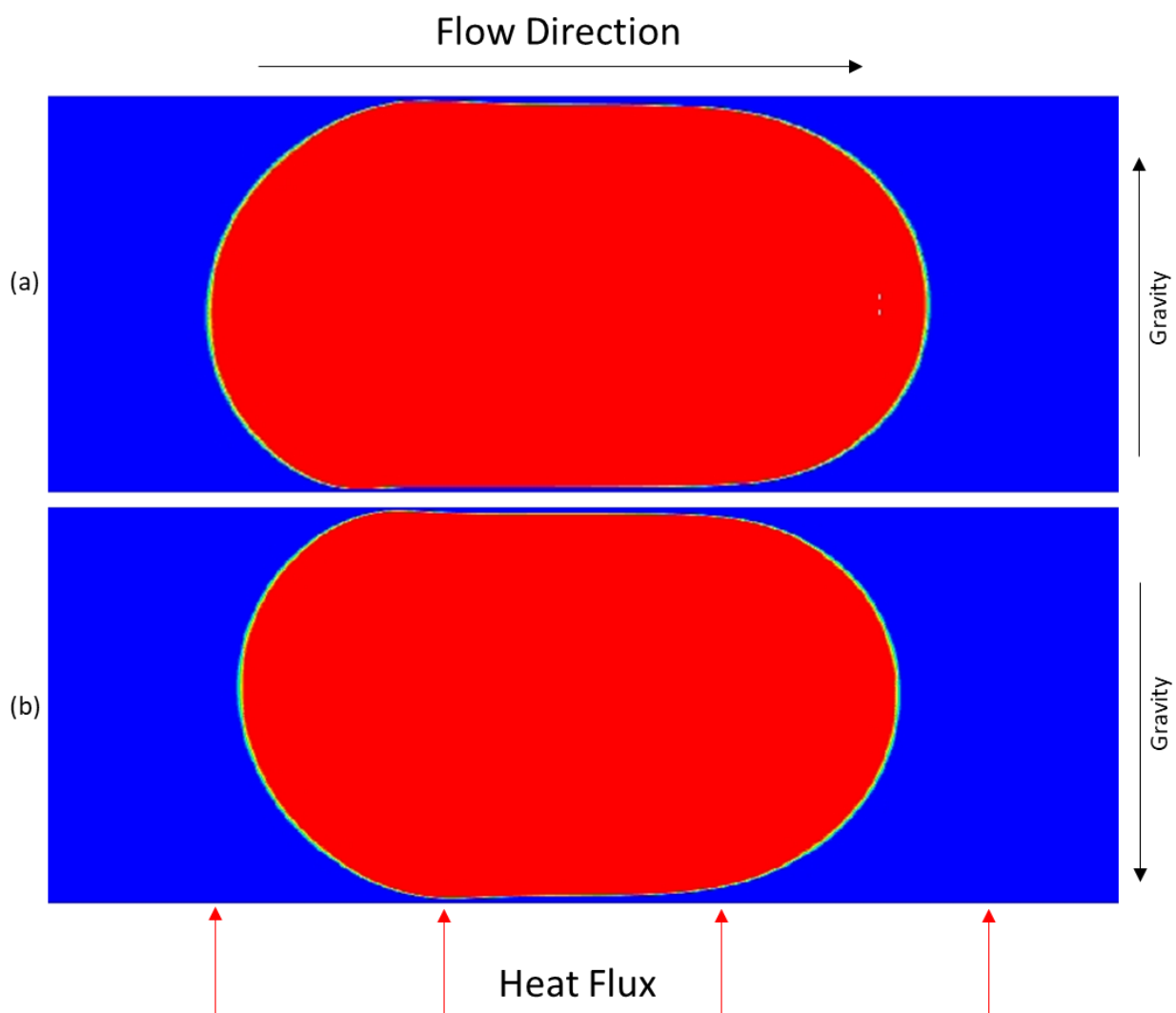

Figure 4-10: Vapour slug for: (a) the top-heated detachment case; and (b) the bottom-heated detachment case

The 2D cases have shown that changing the gravitational orientation and the contact angle seriously affects both bubble growth and the HTC. Two of these cases and an additional case are now recreated in the full 3D domain. The hydrodynamics and heat transfer characteristics of the system will then be presented and analysed.

4.4. 3D bubble growth and hydrodynamics

The effects of bubble presence, growth and orientation on the flow characteristic within a microchannel with a high aspect ratio are presented and discussed below. Figure 4-11 shows a sectioned view of the bottom-heated case, which is cut through the x-plane and focuses on the growing bubble.
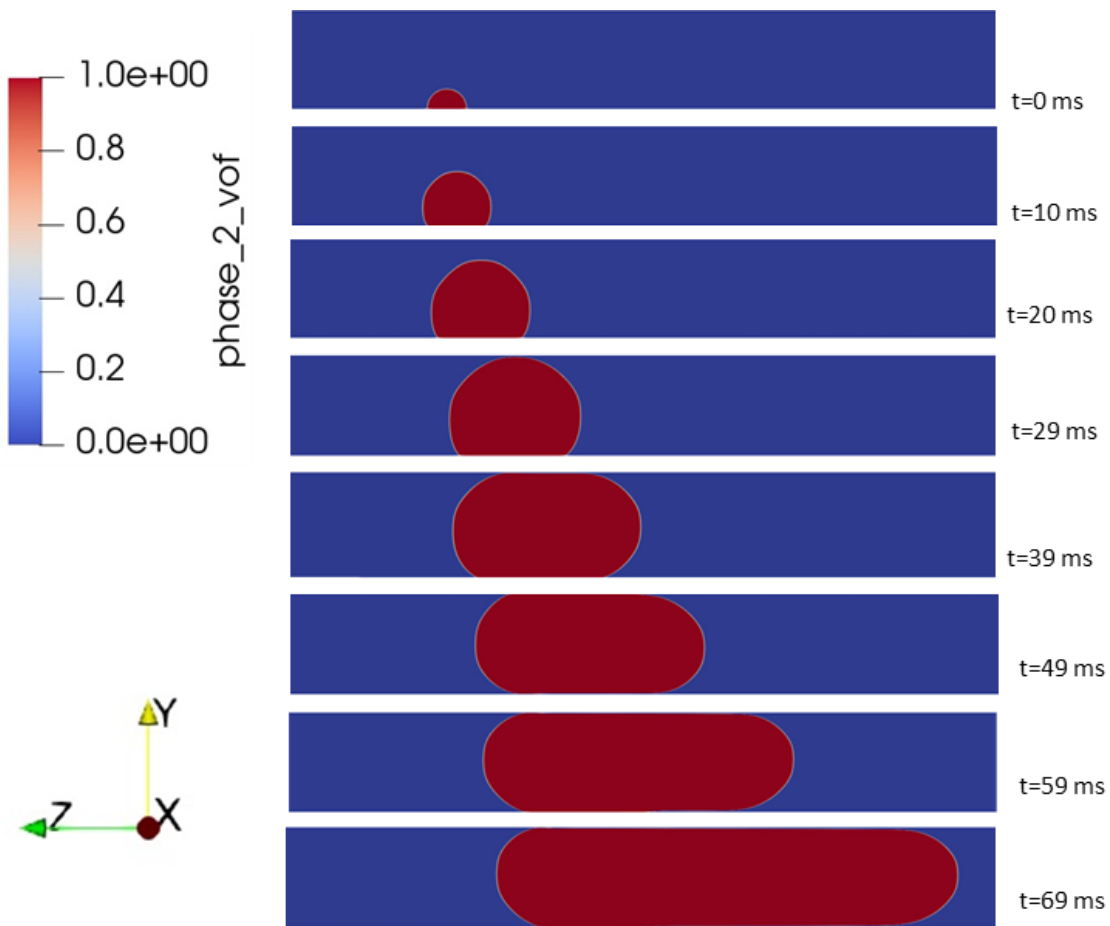
Figure 4-11: Section view of the centre of the bubble for the bottom-heated case

For the first 25 ms, the bubble grows in a spherical shape before it reaches the top wall. The bubble then begins to grow faster along the length of the channel, as well as in the unconfined x-plane. The contact angle between the bubble and the wall remains constant up to 25 ms, which results in the bubble retaining its shape and simply increasing in volume. After 25 ms, the contact angle is gradually reduced, which results in the bubble having significantly more rounded ends and assuming more of a pill shape.

The top-heated case had a distinctly different cross-sectional profile compared to the bottom-heated case, which is displayed in Figure 4-12. The two cases had slightly different contact angles as their initial conditions, which were 45° for the bottom-heated case and 60° for the top-heated case. The contact angle, as well as the buoyancy force, pressed the bubble against the top wall, increasing its contact area in proportion to its volume. For both the bottom- and the top-heated cases, the boundary condition of the non-heated surface was identical, and there was always a thin liquid layer between the wall and the bubble. The angle created between the bubbles and the non-heated wall was lower for the top-heated case than it was for the bottom-heated case.
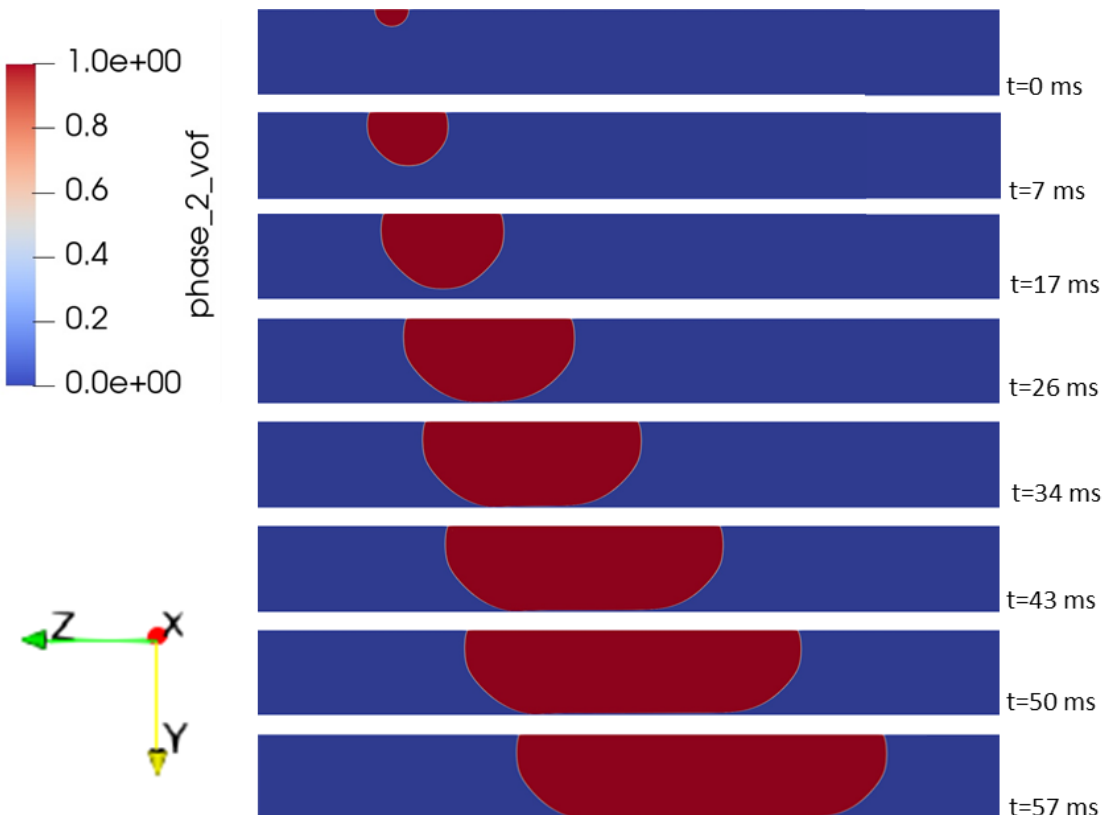
Figure 4-12: Section view of the centre of the bubble for the top-heated case

The behaviour of the vapour bubble in the side-heated case was much more complex than in the other two cases. A sectioned view through the centre of the bubble parallel to the flow direction is shown in Figure 4-13.

The contact area between the bubble and the heated surface increases with bubble volume, as experienced in the other two cases. However, as the buoyancy forces pull the bubble up the wall, it begins to fill the concave area of the channel, which then reduces the contact area. Once the bubble reaches the top of the channel, its upward momentum causes some oscillation, at times 21, 28 and 33 ms, as seen in Figure 4-13, before settling at 42 ms.
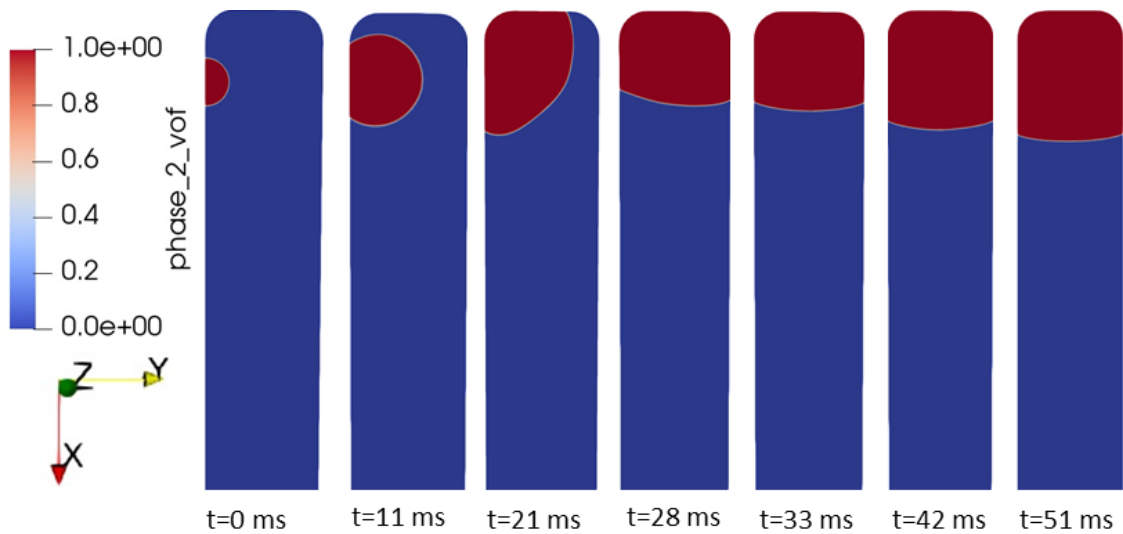
Figure 4-13: Section view through the centre of the bubble for the side-heated case

Each case had very different rates of bubble growth and changes in contact area. Figure 4-14, which shows the bubble volume vs time for each case, shows that, for the initial 5 ms, the top-heated and the side-heated cases had similar growth rates, while the bottom-heated case had a lower growth rate.
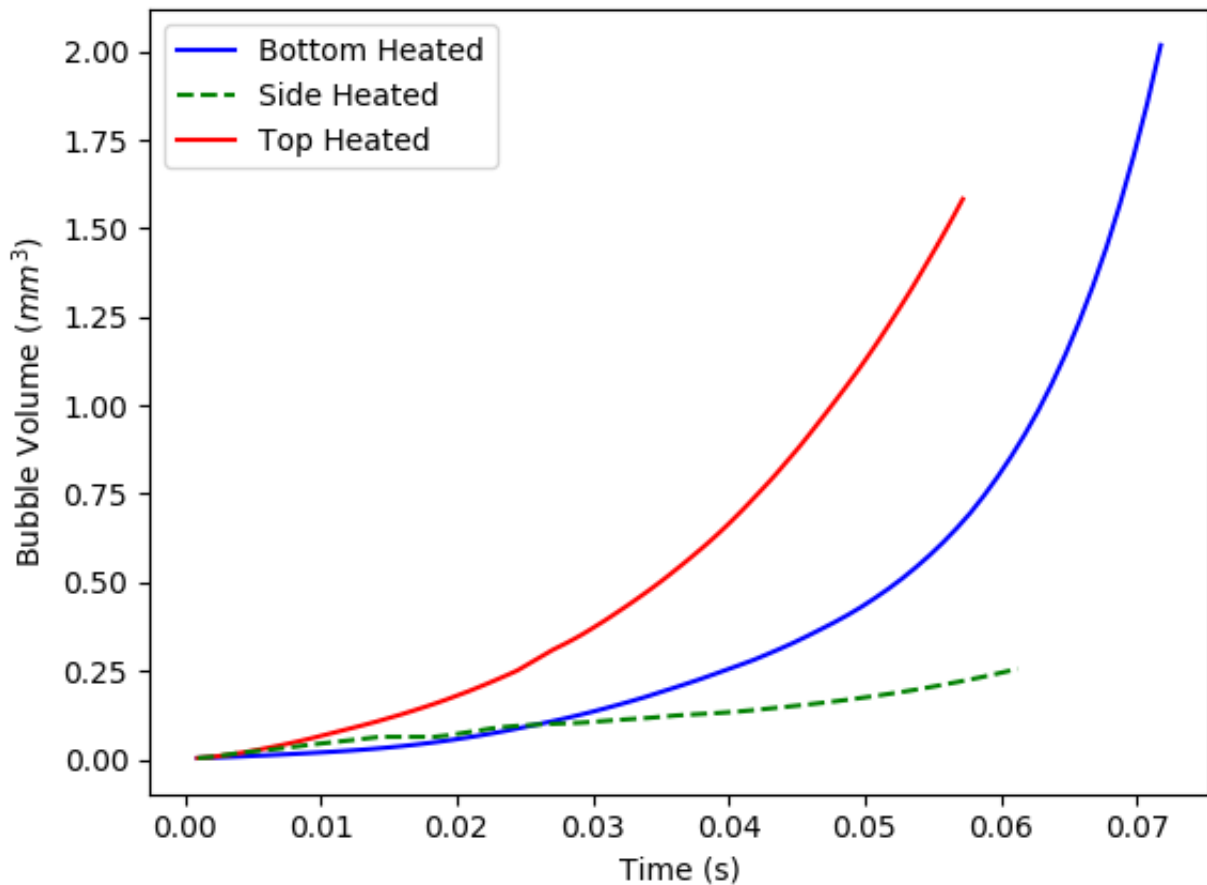
Figure 4-14: Bubble volume vs time for the 3D cases

The bubble growth rates of the top- and bottom-heated cases differed in comparison to their 2D counterparts, with the top-heated case having a much larger growth rate until the bottom-heated case starts to detach.

The higher initial growth rate shown by the top- and side-heated cases is mirrored by Figure 4-15, which shows the size of the contact area between the bubble and the heated surface. After 5 ms, the buoyancy force experienced in the top-heated case pushes the bubble up against the heated surface, which further increases the surface area in comparison to the side-heated case. The opposite is experienced by the bottom-heated case, where the combination of a smaller contact angle and the buoyancy force pulls the bubble off the wall, ensuring that the contact angle remains small in comparison.
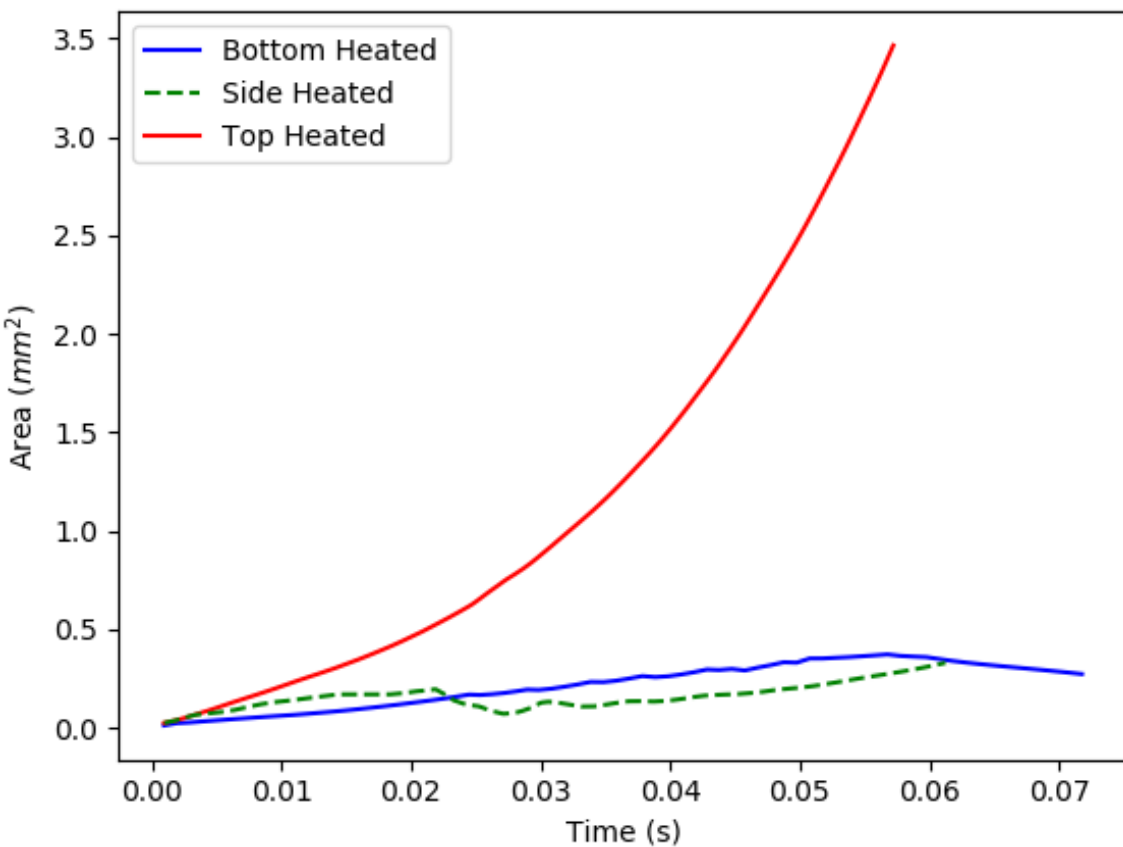
Figure 4-15: Contact area between the bubble and the heated surface vs time for the 3D cases

Figure 4-15 clearly shows the effect of the change in contact angle enforced on the bottom-heated case. The surface area grows until it reaches roughly 30 ms, at which point the bubble volume reaches the characteristic volume of 0.026 mm^3. Once the contact angle is decreased, the growth rate of the contact area gradually decreases, although at a slower rate than in the 2D case. This is likely to be the effect of non-uniform confinement, as the liquid is able to flow around the bubble once it reaches the upper surface. The bubble also starts to detach later, even though confinement begins earlier, which is likely due to the same reason. At 50 ms, the contact angle is at its minimum, and then 5 ms later, the contact area begins to decrease.

85

The oscillatory behaviour of the side-heated case is also displayed in Figure 4-15. The contact area grows steadily up to 21 ms, at which point it begins to decrease. It then increases, decreases and then steadily increases at 28, 31 and 33 ms, respectively. The bottom-heated case has the slowest initial increase in surface area, which remains steady up to 30 ms, at which point the contact angle gradually reduces. The growth then slows and eventually, at 56 ms, the contact angle begins to reduce as the bubble begins to detach. During the first 30 ms of the simulations, especially for the bottom- and top-heated cases, the growth rate of the bubbles is proportional to the contact area between the bubble and the heated surface.

Once the bubbles are seeded within the microchannel, they immediately begin to interrupt the fully developed flow. The surface tension attempts to keep the bubbles stuck to the wall, while the flow of the liquid tries to push them along the channel. This causes the liquid to flow around the bubble, which increases its velocity in the z-direction due to the decrease in cross-sectional area. The velocity magnitude contours at the y = 0.25 mm plane, as well as the black streamlines that originate from the inlet, are plotted in Figure 4-16 for the bottom-heated case.
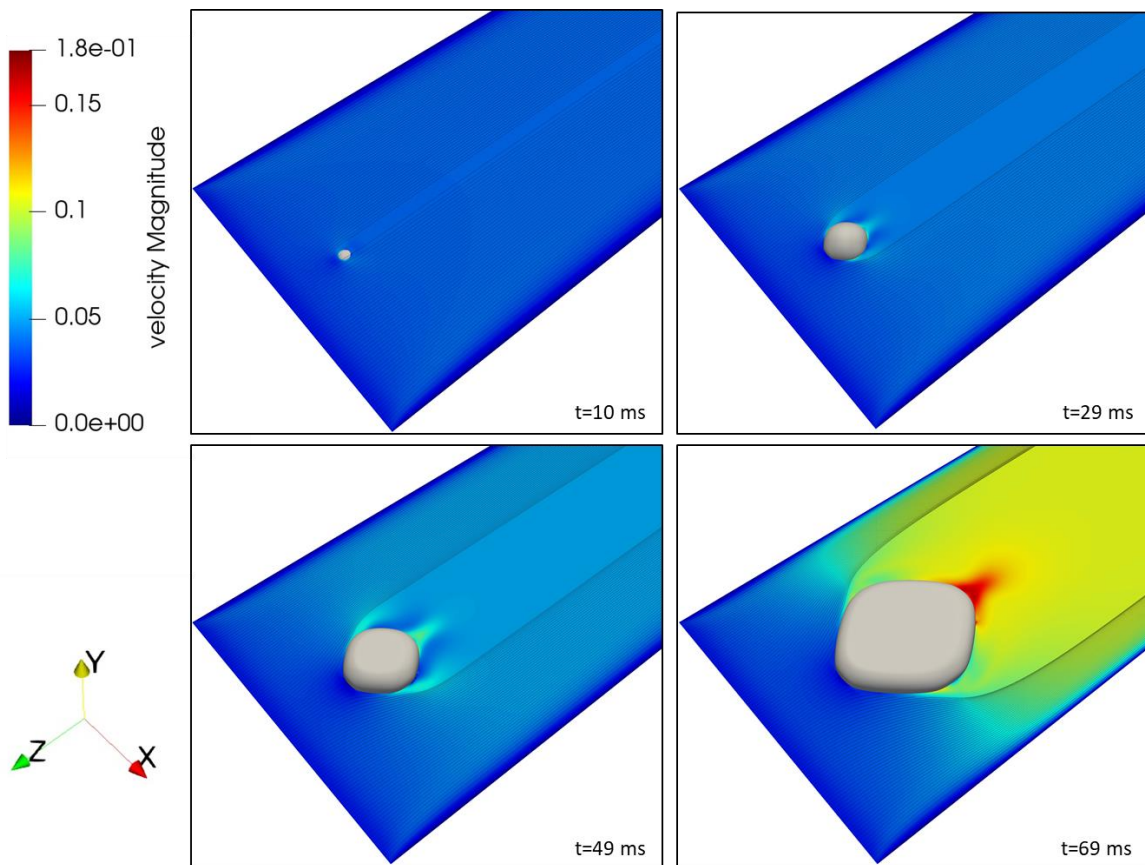
Figure 4-16: Velocity contours and streamlines of the bottom-heated case

During the first 10 ms, the flow is affected very little for the bottom-heated case. However, as the bubble grows, the velocity around the sides of the bubble increases dramatically. The velocity directly adjacent to the side of the bubble increases dramatically due to both the reduced cross-sectional flow area and the expansion of the bubble. As focus is moved towards the front of the bubble, the velocity suddenly decreases due to the increased area before increasing again right at the top of the bubble. The presence of the bubble increases the maximum velocity within the system from 0.04 to 0.18 mm/s, which has some positive implications for the system's thermal characteristics.

Similar phenomena are experienced during the top-heated case. The velocity magnitude contours and streamlines of this case are shown in Figure 4-17. The bubble begins to influence the flow much earlier than in the bottom-heated case, with a large influence already being observed at 7 ms. When one looks at the fourth frame in the bottom- and top-heated cases, the bubbles, which have similar volumes, cause similar disturbance patterns in the streamlines. However, the maximum velocity is much higher in the bottom-heated case, which is 0.18 m/s in comparison to 0.13 m/s.
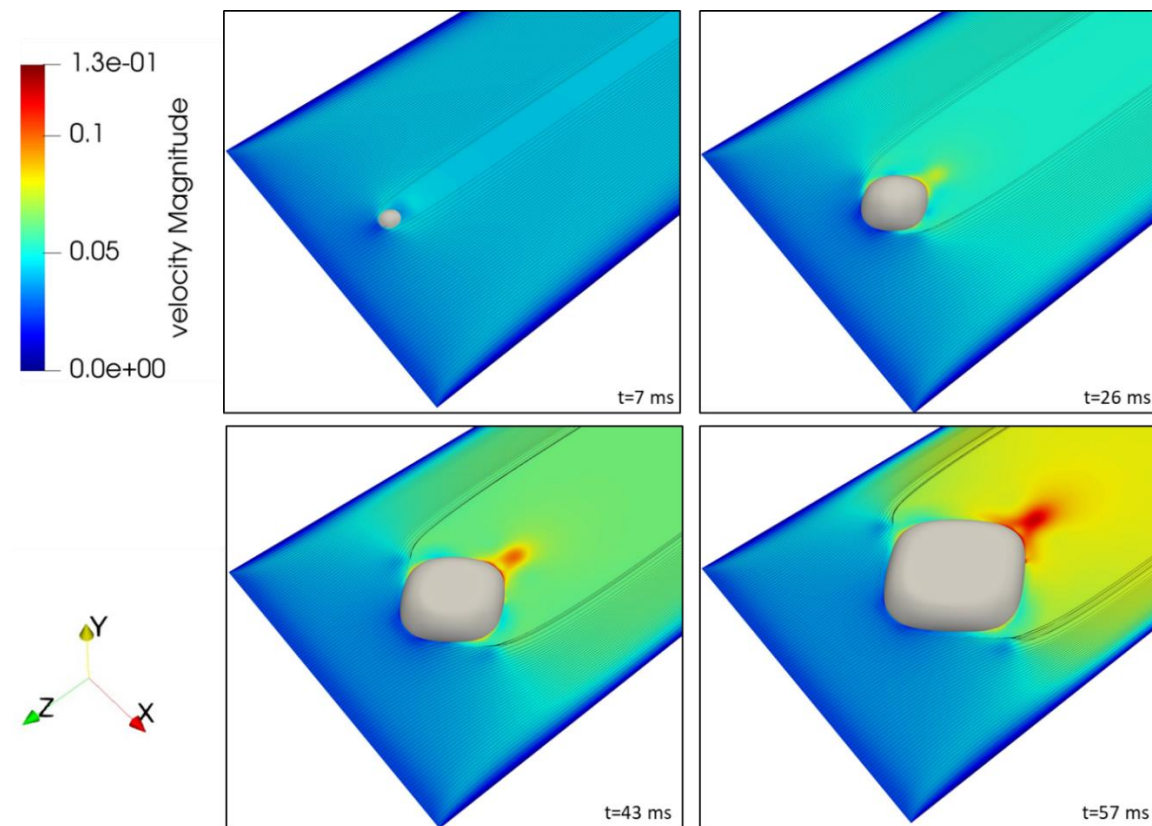
Figure 4-17: Velocity contours and streamlines of the top-heated case (m/s)

The velocity contours and streamlines for the side-heated case, shown in Figure 4-18, are distincly different from those for the bottom- and top-heated cases. This is mostly due to the position of the bubble, which rises to the top of the channel and becomes confined in three dimensions, as opposed to the 2D confinement experienced in the other two cases.

The maximum velocity in relation to the bubble volume is higher for the side-heated case, which can be attributed to the fact that the fluid can only flow around it in one direction when the cross-sectional area is decreased. However, the velocity boundary layers are formed at the top of the channel. Therefore, the presence of the bubble does not interupt the flow as much as it would if the bubble were placed in the centre of the channel.
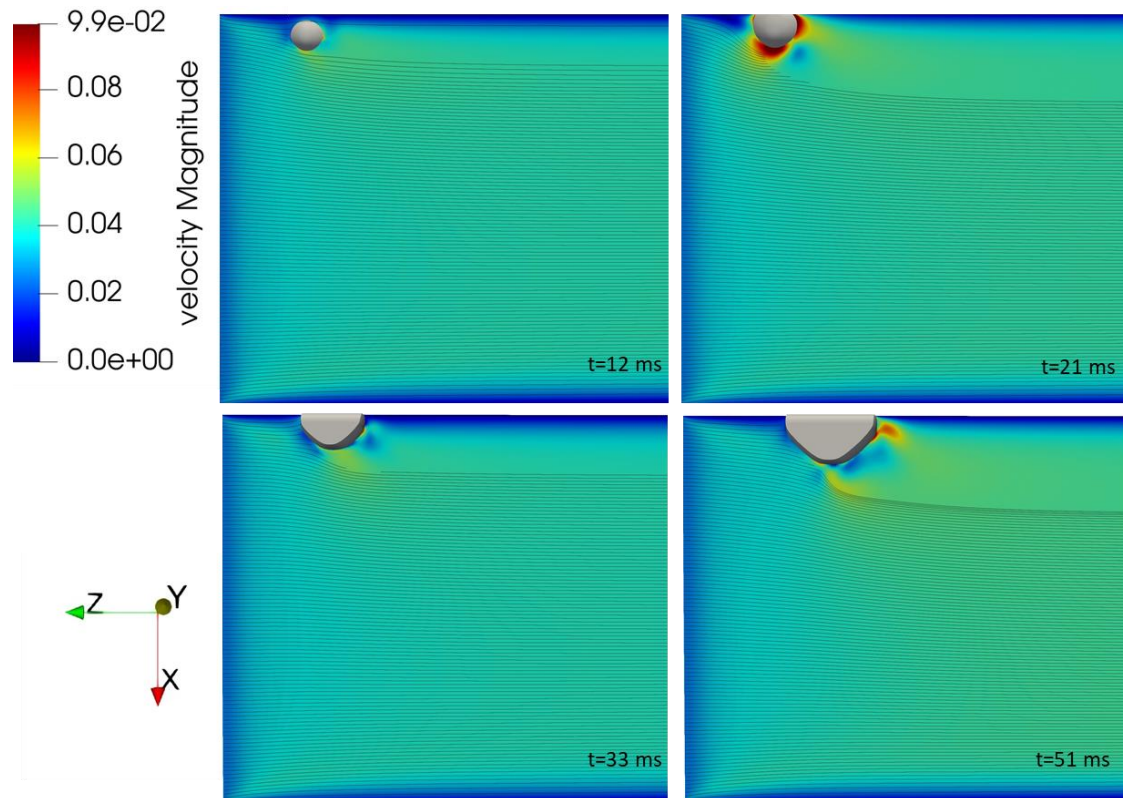
Figure 4-18: Velocity contours and streamlines of the side-heated case (m/s)

The presence of bubbles within the microchannel has been shown to affect the flow of the liquid around it differently for each gravitational orientation. This phenomena is replicated within the bubbles as well. Figure 4-19 shows cross-sections of the bubbles in the top- and bottom-heated cases, while they have similar bubble volumes. Overlayed on the bubbles are velocity vectors, which show the direction of flow. Inner bubble circulation has been shown to increase heat transfer during flow boiling by interupting the thermal boundary layers formed within the bubble (Che et al., 2013). Inner bubble circulation can be seen in both the top- and the bottom-heated cases, albeit in different positions and with different intensities. The top-heated case has a single circulation zone at the front of the bubble close to the heated surface, while the bottom-heated case has two circulation zones at the rear of the bubble.

Figure 4-19 also shows the difference between the bubbles once the bottom-heated bubble has begun to detach from the heated surface. The contact area between the bubble and the wall is much smaller for the bottom-heated case and is situated at the rear of the bubble. It is directly followed by a thin liquid layer between the bubble interface and the heated surface.
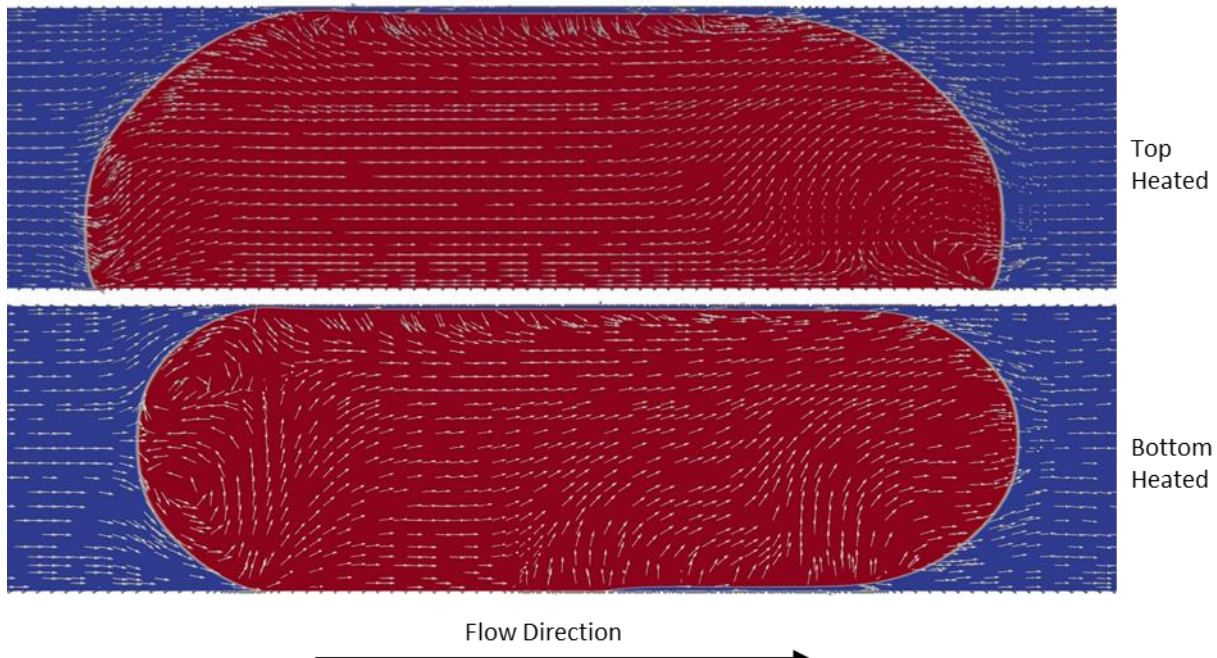
Figure 4-19: Velocity direction vectors of the top-heated (top) and bottom-heated (bottom) cases

The effects of varying gravitational orientations have been shown to have a significant effect on the growth rates, contact area and flow characteristics of a microchannel with a high aspect ratio.

4.5.   3D heat transfer characteristics

The effects of gravitational orientation on the heat transfer characteristics of a microchannel with a high aspect ratio are reported in the following section. Figure 4-20 shows a cross-section of the microchannel that is focused on the bubble for the bottom-heated case. As heat is pumped into the system, the vapour temperature increases, and the thermal gradient transports the heat to the liquid-vapour interface, where evaporation occurs. As the bubble grows, the liquid in front of it is accelerated, which interferes with the thermal boundary layer in front of it, increasing heat transfer in that area. The heat transfer is also increased behind the bubble, because when the bubble moves forward, cooler liquid is sucked in behind it. This is visualised in Figure 4-20. The biggest effect of the bubble on the heat transfer is caused by the thin liquid layer between the bubble and the heated surface. This thin layer creates a high temperature gradient within it, which conducts heat to the bubble interface, increasing the evaporation rate.
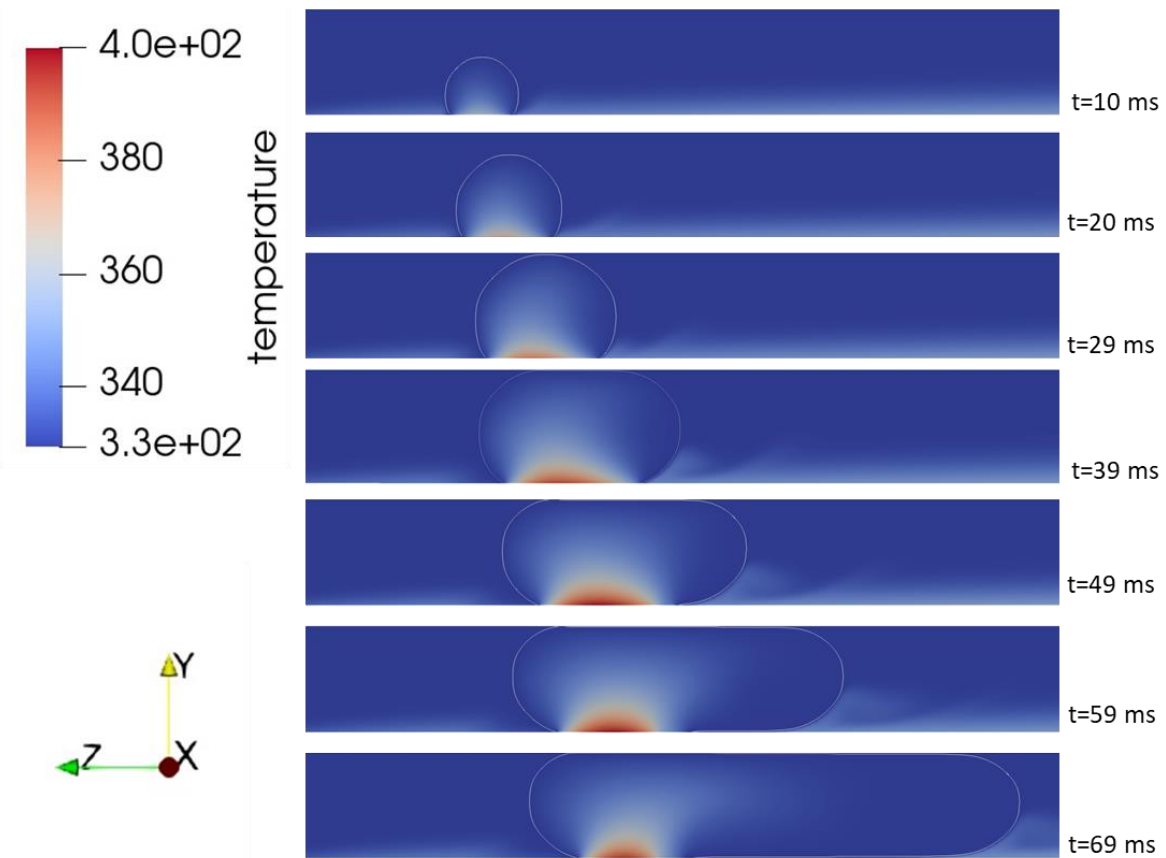
Figure 4-20: Temperature contours of the bottom-heated case (K)

The temperature contours for the top-heated case, which are presented in Figure 4-21, show a similar behaviour to the bottom-heated case until the contact angle is reduced. The interface is always at the saturation temperature, which is a characteristic of the heat transfer model. As the bubble grows, the maximum temperature dramatically increases because the distance from the surface to the bubble interface is so much larger. The fact that the bubble is only confined in one direction means that the interface can spread further away, which causes a high surface temperature and therefore a low HTC.
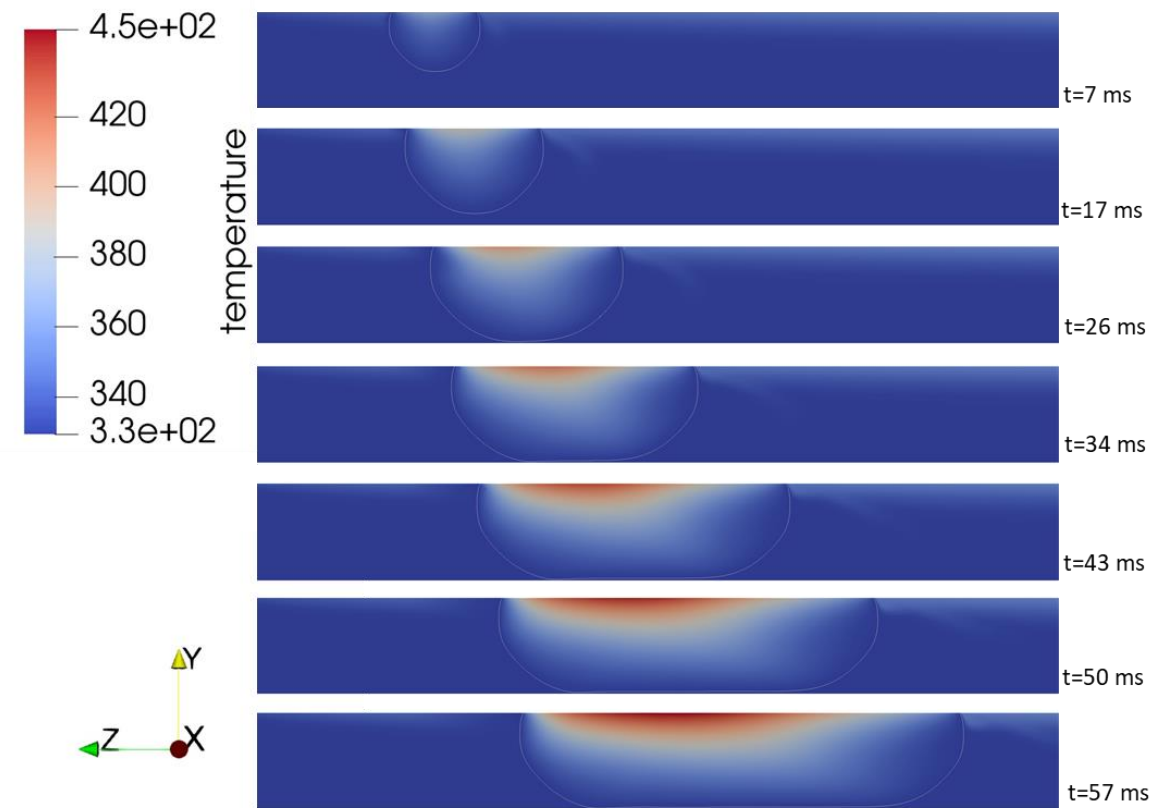
Figure 4-21: Temperature contours of the top-heated case (K)

The side-heated temperature contours, which are presented in Figure 4-22, have a distinctly different behaviour to the other two cases.
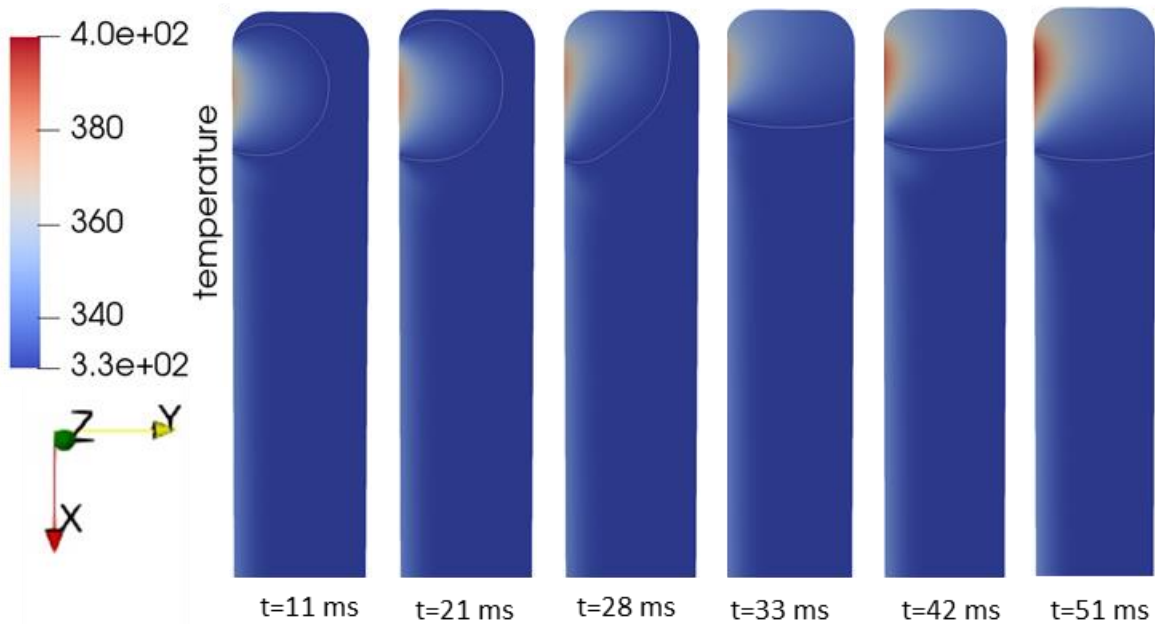
Figure 4-22: Temperature contours of the side-heated case (K)

As the bubble initially increases in volume and the surface area increases, the maximum temperature also increases. However, as the bubble slides up into the top of the channel, the contact area, and therefore the maximum temperature, also decreases. As the bubble oscillates between t = 28 and 42 ms, the maximum temperature displays erratic behaviour, rising and dipping several times. When the oscillations stop and the surface area starts to steadily increase, the maximum temperature increases as well.

The maximum temperature of each of the cases is presented in Figure 4-23. The top-heated case has the highest initial growth rate and the highest temperature during the simulations. The growth rate starts off high, but gradually slows down to 30 ms. At 30 ms, the bubble is prevented from growing radially outwards by the top wall and can only grow in two dimensions. When this happens, the growth rate suddenly increases before gradually decreasing again. The maximum temperature of the side-heated case is erratic. However, if it is compared with the contact area in Figure 4-15, the spikes and dips in the maximum surface temperature correspond with the spikes and dips in the surface area. All three cases show the same correlation, that the maximum temperature in the bubble is proportional to the contact area between the bubble and the heated surface.
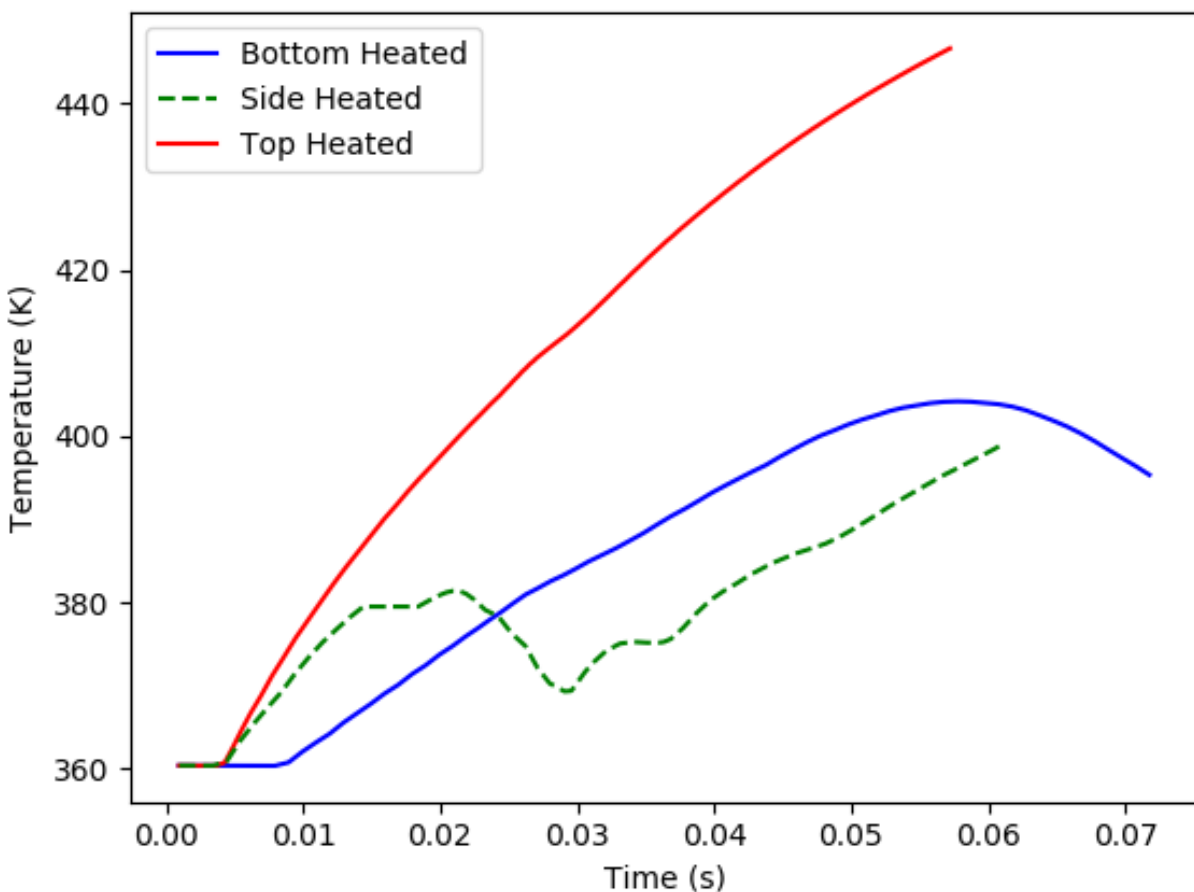
Figure 4-23: Maximum temperature of the heated surface vs time for the 3D cases

The maximum temperature of the top-heated case is roughly 40 °C higher than the side- and bottom-heated cases. However, this trend is not replicated by the average HTC of the heated surface, which is shown in Figure 4-24. The HTC of the top- and side-heated cases increases as the bubble grows within the channel. However, this increase is dwarfed by the growth of the bottom-heated case. The HTC is proportional to the contact area for the first 30 ms. However, after 30 ms, the bottom-heated case begins to increase significantly. As the bubble begins to detach from the wall, cool liquid is sucked beneath it, disrupting the thermal boundary layer and leaving a thin film between the bubble and the wall. This leads to a large area on the heated surface that is close to the saturation temperature of the fluid.
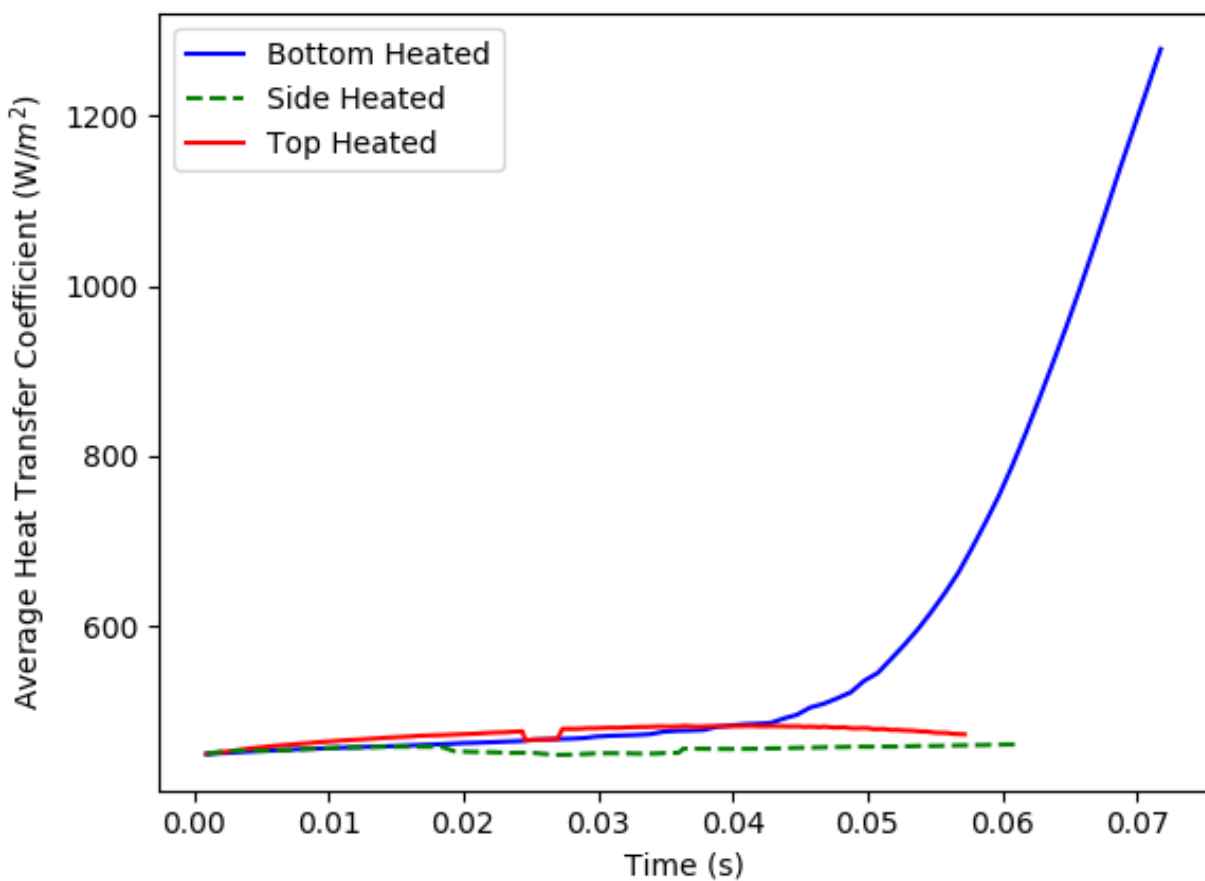
Figure 4-24: Average HTC vs time for the 3D cases

When comparing the HTC of the bottom-heated cases to the top-heated cases at the same bubble volume, which is the maximum volume of the top-heated case (1.6 mm^3), the bottom-heated case is 150% higher. At their respective maximum volumes, the bottom-heated case was 165% higher than the top-heated case.

4.6.   Conclusion

The effects of gravitational orientation, contact angle and non-uniform confinement on bubble growth in a microchannel have been simulated in both a 2D and a 3D domain with a high aspect ratio.

The results have shown that large differences in bubble growth rate, contact area between the vapour phase and the heated surface, the maximum temperature and the average HTC are induced when altering the gravitational orientation. The results also show that the impact of gravitational orientation changes when the contact angle changes, with larger contact angles inducing a stronger gravitational influence. Once non-uniform confinement is implemented, more erratic behaviour is experienced, especially in the side-heated case.

These results show the need for these aspects to be considered when designing CHEs, especially if they could be rotated in a similar position to the side-heated case. While these results have highlighted some of the impacts that these factors can produce, more research is required to entirely understand the interactions that they may have with other flow boiling phenomena.

5. Conclusion

In this study, numerical simulations were performed to investigate the effect of gravitational orientation on the growth of a single bubble with non-uniform heating in a microchannel with a high aspect ratio. A literature study was first performed that covered the basics of heat transfer within microchannels, flow boiling and previous numerical investigations. The applications that could be potentially benefitted by this study were described in the literature study, and several experimental studies that have shown gravitational affects to have a relevant impact on heat transfer during microchannel flow boiling were discussed.

The next section gave a detailed description of the numerical methodology that was utilised. The equations that govern the system were described and the solution procedure was listed. The models that were created for mass transfer, mesh adaption and bubble departure were explained individually. A validation was then performed that investigated the influence of mesh size on the solution, and the results were compared with existing literature.

Ansys Fluent was used to perform the simulations, which were both 2D and 3D, and used the VOF method. The domain of focus was a 0.5 x 5 x 10 mm rectangular microchannel with rounded corners, and FC-72 as the working fluid. Only the base of the channel was heated, and a single bubble was initialised on the base. The bubble was in the centre for the bottom- and top-heated cases, and on the edge of the heated surface for the side-heated case. A mass flux of 40 kg/m^2.s and a heat flux of 10 kW/m^2 were applied to the system. The simulation times ranged from 58 to 72 ms. First, a set of 2D planar simulations was performed to analyse the effect of gravity and the applied contact angle. The results of these 2D cases were then used to determine the initial and operating conditions of the 3D cases that will best represent the experimental investigation of Meyer et al. (2020).

The results were then analysed, and the following conclusions were drawn:

- The major effect of gravitational orientation on flow boiling in microchannels is the location of nucleated bubbles and their tendency to depart from the wall. When bubbles depart, they vacate volume close to the heated surface that is then filled with cooler liquid. As the contact area between the bubble and the heated surface becomes smaller, a thin liquid layer is left between the heated surface and the liquid vapour interface, which causes a high thermal gradient, and therefore more heat conduction.
- Bubbles growing within the channel interrupt the velocity profile, which causes the velocity in certain areas both around the bubble and upstream of it to increase, and the thermal boundary layers in these areas are disrupted.
- The side-heated case has the lowest effect on the velocity streamlines because the bubble floats to the top of the channel, where 3D confinement has reduced the flow of liquid.

- As more vapour comes into contact with the heated surface, the maximum temperature of this surface increases proportionately to the contact area.

- During the first stages of bubble growth, the growth rate is proportional to the contact area between the bubble and the heated surface. Once the bubble begins to depart and a liquid film is formed, this dominates bubble growth.

- Before bubble departure occurs, the average HTC remains relatively steady, because the increase in heat transfer that occurs at the contact region between the liquid-vapour interface and the heated surface is countered by the decrease in heat transfer caused by the vapour region. Once bubble departure begins to occur, the quenching effect, and later slug flow, massively increases the average HTC.

- When one only looks at the 3D cases, the total HTC is highest for the bottom-heated case, which experiences bubble departure. The top-heated case is the second highest, and the side-heated case performs the worst, because the bubble floats to the top of the channel and the contact area between its liquid-vapour interface and the heated surface is reduced.

This study has provided insight into bubble growth during flow boiling in a microchannel, which is difficult to visualise experimentally due to its tiny scale and confined nature. However, many improvements can be made to the current model to investigate different flow regimes, and many more cases are required to better understand the influence of the many dimensionless parameters.

6. Recommendations

The numerical simulations that were performed in this study were idealised cases that were designed to isolate the effects of gravitational orientation and non-uniform confinement. Many assumptions and models were used to recreate physical phenomena, such as the mass transfer and bubble detachment models. However, many aspects can still be improved upon, especially when full-flow boiling, which includes nucleation and coalescence, is simulated. Some of these aspects are the following:

- The detachment of bubbles is a major factor that influences behaviour. However, the model used relied on inducing bubble detachment by manually changing the contact angle. The development and utilisation of a function that varies the contact angle according to bubble volume, pressure, surrounding fluid velocity and confinement criteria will allow for a better physical representation when multiple bubbles are simulated.

- Nucleation sites are dependent on small inconsistencies on the microchannel wall. To replicate full-flow boiling, a function that randomly produces nucleation sites based on the material and heat flux is needed.

- Bubble coalescence and mass transfer involve intermolecular forces that are difficult to replicate using CFD. Therefore, utilising a combination of either molecular dynamics or the Lattice-Boltzmann method could provide a more accurate representation.

- One would need to perform many more cases involving different parameters to gain a better understanding of the phenomena in question. The channel size, aspect ratio, fluid velocity, heat flux, axial orientation, inclination and working fluid can all be varied to create correlations to quantify the effects in proportion to dimensionless parameters such as Re, Bo and Ca numbers.

References

3M-Flourinert 2000. Electronic Liquid FC-72, Product Information.

Agostini, B., Bontemps, A. & Thonon, B. 2006. Effects of Geometrical and Thermophysical Parameters on Heat Transfer Measurements in Small-Diameter Channels. *Heat Transfer Engineering,* 27, 14-24.

ASME, V. V. 2009. Standard for verification and validation in computational fluid dynamics and heat transfer. *American Society of Mechanical Engineers: New York, NY, USA.*

Bar-Cohen, A. 1993. Thermal management of electronic components with dielectric liquids. *JSME International Journal Series B Fluids and Thermal Engineering,* 36, 1-25.

Barber, J., Brutin, D., Sefiane, K., Gardarein, J. & Tadrist, L. 2011. Unsteady-state fluctuations analysis during bubble growth in a "rectangular" microchannel. *International Journal of Heat and Mass Transfer,* 54, 4784-4795.

Barber, J., Sefiane, K., Brutin, D. & Tadrist, L. 2009. Hydrodynamics and heat transfer during flow boiling instabilities in a single microchannel. *Applied Thermal Engineering,* 29, 1299-1308.

Besarati, S. M., Goswami, D. Y. & Stefanakos, E. K. 2015. Development of a solar receiver based on compact heat exchanger technology for supercritical carbon dioxide power cycles. *Journal of Solar Energy Engineering,* 137, 031018.

Bi, J., Christopher, D. M., Zhao, D., Xu, J. & Huang, Y. 2019. Numerical study of bubble growth and merger characteristics during nucleate boiling. *Progress in Nuclear Energy,* 112, 7-19.

Bogojevic, D., Sefiane, K., Walton, A., Lin, H. & Cummins, G. 2009. Two-phase flow instabilities in a silicon microchannels heat sink. *International Journal of Heat and Fluid Flow,* 30, 854-867.

Bordbar, A., Taassob, A., Zarnaghsh, A. & Kamali, R. 2018. Slug flow in microchannels: Numerical simulation and applications. *Journal of industrial and engineering chemistry.*

Brauner, N. & Maron, D. M. 1992. Identification of the range of 'small diameters' conduits, regarding two-phase flow pattern transitions. *International Communications in Heat and Mass Transfer,* 19, 29-39.

Bretherton, F. P. 1961. The motion of long bubbles in tubes. *Journal of Fluid Mechanics,* 10, 166.

Brutin, D., Topin, F. & Tadrist, L. 2003. Experimental study of unsteady convective boiling in heated minichannels. *International Journal of Heat and Mass Transfer,* 46, 2957-2965.

Burk, B. E., Grumstrup, T. P., Bevis, T. A., Kotovsky, J. & Bandhauer, T. M. 2019. Computational examination of two-phase microchannel heat transfer correlations with conjugate heat spreading. *International Journal of Heat and Mass Transfer,* 68-79.

Carlson, A. & Dinh, T.-N. 2007. *NUMERICAL SIMULATIONS OF SLUG FLOW IN A MICRO CHANNEL.* Institutt for energi-og prosessteknikk.

Çengel, Y. A. & Ghajar, A. J. 2015. *Heat and mass transfer : fundamentals & applications,* New York, NY, McGraw Hill Education.

Che, Z., Wong, T. N. & Nguyen, N.-T. 2013. Heat transfer in plug flow in cylindrical microcapillaries with constant surface heat flux. *International Journal of Thermal Sciences,* 64, 204-212.

Cheng, P. & Wu, H. Y. 2006. Mesoscale and Microscale Phase-Change Heat Transfer. *ADVANCES IN HEAT TRANSFER,* 39, 461-564.

Chinnov, E., Ronshin, F. & Kabov, O. 2015. *Features of two-phase flow in a rectangular microchannel with the height of 300 μm*.

Colombo, M. & Fairweather, M. 2016. Accuracy of Eulerian–Eulerian, two-fluid CFD boiling models of subcooled boiling flows. *International Journal of Heat and Mass Transfer,* 103**,** 28-44.

Courant, R., Friedrichs, K. & Lewy, H. 1967. On the partial difference equations of mathematical physics. *IBM journal of Research and Development,* 11**,** 215-234.

Craig, K. J., Moghimi, M. A., Rungasamy, A. E., Marsberg, J. & Meyer, J. P. 2016. Finite-volume ray tracing using Computational Fluid Dynamics in linear focus CSP applications. *Applied Energy,* 183**,** 241-256.

del Río, P., Peñasco, C. & Mir-Artigues, P. 2018. An overview of drivers and barriers to concentrated solar power in the European Union. *Renewable and Sustainable Energy Reviews,* 81**,** 1019-1029.

Ferrari, A., Magnini, M. & Thome, J. R. 2018. Numerical analysis of slug flow boiling in square microchannels. *International Journal of Heat and Mass Transfer,* 123**,** 928-944.

Ferziger, J. H. & Perić, M. 2002. *Computational methods for fluid dynamics,* Berlin ;, Springer.

Fondelli, T., Andreini, A. & Facchini, B. 2015. *Numerical Simulation of Dam-Break Problem Using an Adaptive Meshing Approach*.

Fouilland, T. S., Fletcher, D. F. & Haynes, B. S. 2010. Film and slug behaviour in intermittent slug-annular microchannel flows. *Chemical Engineering Science,* 65**,** 5344-5355.

Freeman, J., E. U, K. & S. R, R. 2014. *Study of the errors influencing heliostats for calibration and control system design*.

Guo, Z., Fletcher, D. F. & Haynes, B. S. 2016. Numerical simulation of annular flow hydrodynamics in microchannels. *Computers & Fluids,* 133**,** 90-102.

Gupta, R., Fletcher, D. F. & Haynes, B. S. 2010. CFD modelling of flow and heat transfer in the Taylor flow regime. *Chemical Engineering Science,* 65**,** 2094-2107.

Hardt, S. & Wondra, F. 2008. Evaporation model for interfacial flows based on a continuum-field representation of the source terms. *Journal of Computational Physics,* 227**,** 5871-5895.

Hassan, I., Phutthavong, P. & Abdelgawad, M. 2004. MICROCHANNEL HEAT SINKS: AN OVERVIEW OF THE STATE-OF-THE-ART. *Microscale Thermophysical Engineering,* 8**,** 183-205.

Hecht, K., Messerschmidt, F., Pfeifer, P., Dittmeyer, R., Kraushaar-Czarnetzki, B. & Hecht, S. 2013. Surface roughness of machined microchannels and its effect on multiphase boundary conditions. *Chemical Engineering Journal,* 227**,** 2-12.

Ho, C. K. 2017. Advances in central receivers for concentrating solar applications. *Solar Energy,* 152**,** 38-56.

Hsu, L.-C., Cion, S.-W., Lin, K.-W. & Wang, C.-C. 2015. An experimental study of inclination on the boiling heat transfer characteristics of a micro-channel heat sink using HFE-7100. *International Communications in Heat and Mass Transfer,* 62**,** 13-17.

Husain, A. & Kwang-Yong, K. 2008. Shape Optimization of Micro-Channel Heat Sink for Micro-Electronic Cooling. *IEEE Transactions on Components and Packaging Technologies,* 31.

IRENA. 2018. *Renewable Energy Technologies* [Online]. Available: http://resourceirena.irena.org/gateway/dashboard/?topic=4&subTopic=19 [Accessed].

Jafari, R. & Okutucu-Özyurt, T. 2016a. 3D numerical modeling of boiling in a microchannel by arbitrary Lagrangian–Eulerian (ALE) method. *Applied Mathematics and Computation,* 272, 593-603.

Jafari, R. & Okutucu-Özyurt, T. 2016b. Numerical simulation of flow boiling from an artificial cavity in a microchannel. *International Journal of Heat and Mass Transfer,* 97, 270-278.

Jesseela, S. & Sobhan, C. 2015. Numerical modeling of annular flow with phase change in a microchannel. *International Journal of Thermal Sciences,* 89, 87-99.

Kandlikar, S., Garimella, S., Li, D., Colin, S. & King, M. R. 2005. *Heat transfer and fluid flow in minichannels and microchannels*, elsevier.

Kandlikar, S. G. 2002. Fundamental issues related to flow boiling in minichannels and microchannels. *Experimental Thermal and Fluid Science,* 26, 389-407.

Kandlikar, S. G. & Balasubramanian, P. 2005. An experimental study on the effect of gravitational orientation on flow boiling of water in 1054× 197μm parallel minichannels. *Journal of Heat Transfer,* 127, 820-829.

Katto, Y. & Ohno, H. 1984. An improved version of the generalized correlation of critical heat flux for the forced convective boiling in uniformly heated vertical tubes. *International Journal of Heat and Mass Transfer,* 27, 1641-1648.

Kew, P. A. & Cornwell, K. 1997. Correlations for the prediction of boiling heat transfer in small-diameter channels. *Applied Thermal Engineering,* 17, 705-715.

Kharangate, C. R. & Mudawar, I. 2017. Review of computational studies on boiling and condensation. *International Journal of Heat and Mass Transfer,* 108, 1164-1196.

Korniliou, S. 2018. Experimental study on local heat transfer coefficients and the effect of aspect ratio on flow boiling in a microchannel.

Kreutzer, M. T., Kapteijn, F., Moulijn, J. A. & Heiszwolf, J. J. 2005. Multiphase monolith reactors: Chemical reaction engineering of segmented flow in microchannels. *Chemical Engineering Science,* 60, 5895-5916.

Kurimoto, R., Hayashi, K., Minagawa, H. & Tomiyama, A. 2018. Numerical investigation of bubble shape and flow filed of gas–liquid slug flow in circular microchannels. *International Journal of Heat and Fluid Flow,* 74, 28-35.

Lei, N., Ortega, A. & Vaidyanathan, R. Modeling and optimization of multilayer minichannel heat sinks in single-phase flow. ASME 2007 InterPACK conference collocated with the ASME/JSME 2007 thermal engineering heat transfer summer conference, 2007. American Society of Mechanical Engineers, 29-43.

Li, J.-M. & Wang, B.-X. 2003. Size effect on two-phase regime for condensation in micro/mini tubes. *Heat Transfer—Asian Research,* 32, 65-71.

Li, L., Coventry, J., Bader, R., Pye, J. & Lipiński, W. 2016. Optics of solar central receiver systems: a review. *Optics Express,* 24, A985-A1007.

Li, W., Chen, Z., Li, J., Sheng, K. & Zhu, J. 2019. Subcooled flow boiling on hydrophilic and super-hydrophilic surfaces in microchannel under different orientations. *International Journal of Heat and Mass Transfer,* 129, 635-649.

Ling, K., Son, G., Sun, D.-L. & Tao, W.-Q. 2015. Three dimensional numerical simulation on bubble growth and merger in microchannel boiling flow. *International Journal of Thermal Sciences,* 98, 135-147.

Liu, J., Wang, G., Zhang, L., Shi, Y., Zhang, H. & Yao, S.-c. 2017a. Numerical simulation of single bubble boiling behavior. *Propulsion and Power Research,* 6, 117-125.

Liu, Q. & Palm, B. 2016. Numerical study of bubbles rising and merging during convective boiling in micro-channels. *Applied Thermal Engineering,* 99, 1141-1151.

Liu, Q., Wang, W. & Palm, B. 2017b. A numerical study of the transition from slug to annular flow in micro-channel convective boiling. *Applied Thermal Engineering,* 112, 73-81.

Liu, Q., Wang, W. & Palm, B. r. 2017c. Numerical study of the interactions and merge of multiple bubbles during convective boiling in micro channels. *International Communications in Heat and Mass Transfer,* 80, 10-17.

Liu, T. L. & Kim, C. C. 2017. Contact Angle Measurement of Small Capillary Length Liquid in Super-repelled State. *Scientific reports,* 7, 740.

Lockhart, R. & Martinelli, R. 1949. Proposed correlation of data for isothermal two-phase, two-component flow in pipes. *Chem. Eng. Prog,* 45, 39-48.

Lorenzini, D. & Joshi, Y. K. 2018. Computational Fluid Dynamics Modeling of Flow Boiling in Microchannels With Nonuniform Heat Flux. *Journal of Heat Transfer,* 140.

Luo, Y., Zhang, J., Li, W., Sokolova, E., Li, Y. & Minkowycz, W. J. 2017. Numerical investigation of the bubble growth in horizontal rectangular microchannels. *Numerical Heat Transfer; Part A: Applications,* 71, 1175-1188.

Ma, H., Cai, W., Chen, J., Yao, Y. & Jiang, Y. 2016. Numerical investigation on saturated boiling and heat transfer correlations in a vertical rectangular minichannel. *International Journal of Thermal Sciences,* 102, 285-299.

Magnini, M., Pulvirenti, B. & Thome, J. 2013a. Numerical investigation of the influence of leading and sequential bubbles on slug flow boiling within a microchannel. *International Journal of Thermal Sciences,* 71, 36-52.

Magnini, M., Pulvirenti, B. & Thome, J. R. 2013b. Numerical investigation of hydrodynamics and heat transfer of elongated bubbles during flow boiling in a microchannel. *International Journal of Heat and Mass Transfer,* 59, 451-471.

Magnini, M. & Thome, J. 2016a. A CFD study of the parameters influencing heat transfer in microchannel slug flow boiling. *International Journal of Thermal Sciences,* 110, 119-136.

Magnini, M. & Thome, J. R. 2016b. Computational Study of Saturated Flow Boiling Within a Microchannel in the Slug Flow Regime. *Journal of Heat Transfer,* 138, 021502.

Mehdizadeh, A., Sherif, S. A. & Lear, W. E. 2011. Numerical simulation of thermofluid characteristics of two-phase slug flow in microchannels. *International Journal of Heat and Mass Transfer,* 54, 3457-3465.

Mehendale, S., Jacobi, A. & Shah, R. 2000. Fluid flow and heat transfer at micro-and meso-scales with application to heat exchanger design. *Applied Mechanics Reviews,* 53, 175-193.

Meyer, J., Moghimi, M. A., Potgieter, J., Sefiane, K., Valluri, P. & Vermaak, M. 2020. The Effect of Gravitational Orientation on Flow Boiling in a High Aspect-Ratio Rectangular Microchannel with Non-Uniform Heating. *Still to be Submitted*.

Moghimi Ardekani, M. 2017. *Optical thermal and economic optimisation of a linear Fresnel collector.* University of Pretoria.

Moghimi, M. A. & Ahmadi, G. 2018. Wind barriers optimization for minimizing collector mirror soiling in a parabolic trough collector plant. *Applied Energy,* 225, 413-423.

Moghimi, M. A., Craig, K. J. & Meyer, J. P. 2015. Optimization of a trapezoidal cavity absorber for the Linear Fresnel Reflector. *Solar Energy,* 119, 343-361.

Moghimi, M. A., Craig, K. J. & Meyer, J. P. 2017. Simulation-based optimisation of a linear Fresnel collector mirror field and receiver for optical, thermal and economic performance. *Solar Energy,* 153, 655-678.

Mohammed, H., Gunnasegaran, P. & Shuaib, N. 2011. Numerical simulation of heat transfer enhancement in wavy microchannel heat sink. *International Communications in Heat and Mass Transfer,* 38, 63-68.

Mukherjee, A. & Kandlikar, S. G. 2007. Numerical study of single bubbles with dynamic contact angle during nucleate pool boiling. *International Journal of Heat and Mass Transfer,* 50, 127-138.

Ong, C. L. & Thome, J. R. 2011. Macro-to-microchannel transition in two-phase flow: Part 1 - Two-phase flow patterns and film thickness measurements. *Experimental Thermal and Fluid Science,* 35, 37-47.

Ortega, J. D., Christian, J. M. & Ho, C. K. Structural analysis of a direct heated tubular solar receiver for supercritical CO2 Brayton cycle. ASME 2015 9th International Conference on Energy Sustainability collocated with the ASME 2015 Power Conference, the ASME 2015 13th International Conference on Fuel Cell Science, Engineering and Technology, and the ASME 2015 Nuclear Forum, 2015a. American Society of Mechanical Engineers, V001T05A015-V001T05A015.

Ortega, J. D., Khivsara, S. D., Christian, J. M., Yellowhair, J. E. & Ho, C. K. Coupled optical-thermal-fluid modeling of a directly heated tubular solar receiver for supercritical CO2 Brayton cycle. ASME 2015 9th International Conference on Energy Sustainability collocated with the ASME 2015 Power Conference, the ASME 2015 13th International Conference on Fuel Cell Science, Engineering and Technology, and the ASME 2015 Nuclear Forum, 2015b. American Society of Mechanical Engineers, V001T05A018-V001T05A018.

Padilla, R. V., Too, Y. C. S., Beath, A., McNaughton, R. & Stein, W. 2015. Effect of pressure drop and reheating on thermal and exergetic performance of supercritical carbon dioxide Brayton cycles integrated with a solar central receiver. *Journal of Solar Energy Engineering,* 137, 051012.

Ribatski, G., Wojtan, L. & Thome, J. R. 2006. An analysis of experimental data and prediction methods for two-phase frictional pressure drop and flow boiling heat transfer in micro-scale channels. *Experimental Thermal and Fluid Science,* 31, 1-19.

Roldán, M. I., Fernández-Reche, J., Power, S. I. C. o. C. S., Chemical Energy Systems, S. I. C. o. C. S. P. & Chemical Energy Systems Cape Town, S. A. 2016. CFD analysis of supercritical CO2 used as HTF in a solar tower receiver. *AIP Conference Proceedings.* Author(s).

Sadeghi, E., Bahrami, M. & Djilali, N. 2010. Estimation of Nusselt Number in Microchannels of Arbitrary Cross Section with Constant Axial Heat Flux. *Heat Transfer Engineering,* 31, 666-674.

Sanna, A., Hutter, C., Lin, H., Sefiane, K., Walton, A., Pavlovic, E., Golobic, I., A Nelson, R., Karayiannis, T. & B R Kenning, D. 2008. *Simulation and experimental investigation of pool boiling on a silicon wafer with artificial nucleation sites*.

Schrage, R. W. 1953. *A theoretical study of interphase mass transfer*, Columbia University Press.

Serizawa, A., Feng, Z. & Kawara, Z. 2002. Two-phase flow in microchannels. *Experimental Thermal and Fluid Science,* 26, 703-714.

Serrano, M. I. R. 2017. Concentrating Solar Thermal Technologies. *Concentrating Solar Thermal Technologies.* Springer.

Simbolotti, G. 2013. Concentrating solar power technology brief. *IEA-ETSAP and IRENA*.

Steinfeld, A. & Schubnell, M. 1993. Optimum aperture size and operating temperature of a solar cavity-receiver. *Solar Energy,* 50, 19-25.

Sui, Y., Teo, C., Lee, P. S., Chew, Y. & Shu, C. 2010. Fluid flow and heat transfer in wavy microchannels. *International Journal of Heat and Mass Transfer,* 53, 2760-2772.

Szczukiewicz, S., Borhani, N. & Thome, J. R. Two-phase flow boiling in a single layer of future high-performance 3D stacked computer chips. Thermal and Thermomechanical Phenomena in Electronic Systems (ITherm), 2012 13th IEEE Intersociety Conference on, 2012. Ieee, 597-605.

Szczukiewicz, S., Magnini, M. & Thome, J. R. 2014. Proposed models, ongoing experiments, and latest numerical simulations of microchannel two-phase flow boiling. *International journal of multiphase flow,* 59, 84-101.

Talimi, V., Muzychka, Y. S. & Kocabiyik, S. 2012. A review on numerical studies of slug flow hydrodynamics and heat transfer in microtubes and microchannels. *International Journal of Multiphase Flow,* 39, 88-104.

Tanasawa, I. 1991. Advances in condensation heat transfer. *Advances in heat transfer.* Elsevier.

Thome, J. R. 2004. Boiling in microchannels: a review of experiment and theory. *International Journal of Heat and Fluid Flow,* 25, 128-139.

Triplett, K. A., Ghiaasiaan, S. M., Abdel-Khalik, S. I. & Sadowski, D. L. 1999. Gas-liquid two-phase flow in microchannels Part I: two-phase flow patterns. *International Journal of Multiphase Flow,* 25, 377-394.

Tuckerman, D. B. & Pease, R. F. W. 1981. High-performance heat sinking for VLSI. *IEEE Electron Device Letters,* 2.

Vivekanand, S. V. B. & Raju, V. R. K. Simulation of Evaporation Heat Transfer in a Rectangular Microchannel. Procedia Engineering, 2015. 309-316.

Wang, Y., Sefiane, K. & Harmand, S. 2012. Flow boiling in high-aspect ratio mini-and micro-channels with FC-72 and ethanol: experimental results and heat transfer correlation assessments. *Experimental Thermal and Fluid Science,* 36, 93-106.

Wojtan, L., Revellin, R., Thome, J. R. & Italia, H. B. L. I.-H. B. L. 2006. Investigation of saturated critical heat flux in a single, uniformly heated microchannel. *Experimental Thermal and Fluid Science,* 30, 765-774.

Yao, S.-C. & Chang, Y. 1983. Pool boiling heat transfer in a confined space. *International Journal of Heat and Mass Transfer,* 26, 841-848.

Yu, W., Desmulliez, M. P. Y., Drufke, A., Leonard, M., Dhariwal, R. S., Flynn, D., Bognar, G., Poppe, A., Horvath, G. & Kohari, Z. 2010. High-aspect-ratio metal microchannel plates for microelectronic cooling applications. *Journal of micromechanics and microengineering : structures, devices, and systems.,* 20, 025004.

Zada, K. R., Hyder, M. B., Drost, M. K. & Fronk, B. M. 2016. Numbering-up of microscale devices for megawatt-scale supercritical carbon dioxide concentrating solar power receivers. *Journal of Solar Energy Engineering,* 138, 061007.

Zhao, D., Xu, E., Wang, Z., Yu, Q., Xu, L. & Zhu, L. 2016. Influences of installation and tracking errors on the optical performance of a solar parabolic trough collector. *Renewable Energy,* 94, 197-212.

Zhao, Y., Chen, G. & Yuan, Q. 2006. Liquid-liquid two-phase flow patterns in a rectangular microchannel. *AIChE journal,* 52, 4052-4060.

Zhuan, R. & Wang, W. 2012. Flow pattern of boiling in micro-channel by numerical simulation. *International journal of heat and mass transfer,* 55, 1741-1753.

Zu, Y. Q., Yan, Y. Y., Gedupudi, S., Karayiannis, T. G. & Kenning, D. B. R. 2011. Confined bubble growth during flow boiling in a mini-/micro-channel of rectangular cross-section part II:

Approximate 3-D numerical simulation. *International Journal of Thermal Sciences,* 50**,** 267-273.

Appendices

Appendix A: Mesh refinement and mass transfer UDF

/*(Hardt and Wondra, 2008) Evaporation Model.*/

```c
#include "udf.h"

#include "prf.h"

#define domain_ID 2

static real NV=0.0;/*Vapour Normalisation Factor*/

static real NL=0.0;/*Liquid Normalisation Factor*/

static real mass_v=0;/*Vapour Creation per Cell*/

static real mass_l=0;/*Liquid Disappearance per Cell*/

static real enrg_s=0.0;/* Energy Change per Cell*/

static real T_SAT = 329.15;/*Saturation Temperature*/

static real ac= 1; /*Accomodation Coefficient*/

static real mgVOF=0.0; /*Magnitude of VOF Gradient*/

static real M=338; /*Molecular Mass*/

static real h=84500.0; /*Latent Heat*/

static real R=8314.0; /*Gas Constant*/

static real pi =3.1415259;/*pi*/

static real m_lg = 0.0;/*Mass Flux*/

static real m_nt=0.0;/*Temporal Gradient of Mass Flux*/

static real m_gr=0.0;/*Source term for Mesh Adaption*/

static real Ntop=0.0;/*Normalisation factor*/

static real Nbot=0.0;/*Normalisation factor denominator*/

static real Ntot=0.0;/*Normalisation factor numerator*/
```

static real RhoG=13.2;/*Vapour Density*/

static real RhoL=1680;/*Liquid Density*/

static real NVbot=0.0;/*Denomenator for Equation 17*/

static real NVLtop=0.0;/*Numerator for Equation 17 and Equation 18/

static real NLbot=0.0;/*Denomenator for Equation 18*/

static real VCutV=1e-3;/*Vapour volume cut-off*/

static real VCutL=1e-1;/*Liquid volume cut-off*/

static real cpl=1052.85; /*Liquid Specific Heat*/

static real cpg=895.2;/*Vapour Specific Heat*/

/*Scalars

uds-scalar-0: Volume Fraction

uds-scalar-1: Initial Mass Source Term Used for Smearing

uds-scalar-2: Smeared Mass Source Term

uds-scalar-3: Initial Mesh Source Term Used for Smearing

uds-scalar-4: Smeared Mesh Source Term

uds-scalar-5: Smeared and Bounded Mass Source Term

uds-scalar-6: Vapour Source Term

uds-scalar-7: Liquid Source Term

uds-scalar-8: Energy Source Term

uds-scalar-9: Gradient of Initial Source Term

*/

/*The purpose of the adjust_gradient function is to assign the volume fraction to a scalar quantity. Ansys Fluent does not automatically calculate the gradient of the volume fraction, but it does calculate it for scalar quantities, so this function forces Ansys Fluent to calculate the gradient of the volume fraction.*/

```
DEFINE_ADJUST(adjust_gradient, domain)

{

  Thread *t;

  cell_t c;

  face_t f;


  domain = Get_Domain(domain_ID);


  /* Fill UDS with the variable. */

  thread_loop_c (t,domain)

    {

      if (THREAD_STORAGE(t,SV_UDS_I(0))!=NULL)

      begin_c_loop (c,t)

        {

          C_UDSI(c,t,0) = (C_VOF(c,t));

        }

      end_c_loop (c,t)

    }


  thread_loop_f (t,domain)

    {

      if (THREAD_STORAGE(t,SV_UDS_I(0))!=NULL)

      begin_f_loop (f,t)

        {

          F_UDSI(f,t,0) = (F_VOF(f,t));
```

```
    }

  end_f_loop (f,t)

  }

}
```

/*The in_s_term function calculates the initial source term that will later be smeared.

First, Ntot, which ensures that the total interfacial area remains constant once the scalar field is

skewed to the liquid side, is calculated.

Next, the initial source term, as well as its gradient, which is used to calculate the gradient of the

energy source term, is calculated.

Finally, the mass flux is multiplied by the interfacial area and the normalisation factor to create the

initial source term. */

```
DEFINE_ADJUST(in_s_term, domain)

{

  Thread *t;

  cell_t c;

  m_lg=0;

  m_gr=0;

  Ntot=0;

  domain = Get_Domain(domain_ID);


  /* Calculate integrals and normalisation factor as N*/

  thread_loop_c(t,domain)

  {

  begin_c_loop(c,t)
```

```
    {

    Ntop += NV_MAG(C_UDSI_G(c,t,0))*C_VOLUME(c,t);

            if (C_VOF(c,t)<0.99 && C_VOF(c,t)>0.01)

    Nbot += C_UDSI(c,t,0)*NV_MAG(C_UDSI_G(c,t,0))*C_VOLUME(c,t);

    }

    end_c_loop(c,t)

    }

    if (PRF_GRSUM1(Nbot)!=0)

    {

                Ntot=PRF_GRSUM1(Ntop)/PRF_GRSUM1(Nbot);

    }


    /* Calculate mass flux. */

    thread_loop_c (t,domain)

    {

        begin_c_loop (c,t)

        {

                mgVOF = NV_MAG(C_UDSI_G(c,t,0));

                if (mgVOF>=1 && C_VOF(c,t)<0.99 && C_VOF(c,t)>0.01)

        {

                    m_lg        =         (2*ac/(2-ac))*sqrt(M/(2*pi*R))*RhoG*h*(C_T(c,t)-
T_SAT)/pow(T_SAT, 1.5);

                    m_gr=(2*ac/(2-ac))*sqrt(M/(2*pi*R))*RhoG*h/pow(T_SAT, 1.5);

        }

        else

        {
```

```
                 m_lg=0;

                              m_gr=0;

       }

                     if (mgVOF>=1)

       {

                     m_nt=(2*ac/(2-ac))*sqrt(M/(2*pi*R))*RhoG*h/pow(T_SAT, 1.5);

       }

       else

       {

                     m_nt=0;

       }


              C_UDSI(c,t,3)=m_nt*mgVOF;

              C_UDSI(c,t,1)=Ntot*C_VOF(c,t)*m_lg*mgVOF;/* Initial Source term P0*/

              C_UDSI(c,t,9)=Ntot*C_VOF(c,t)*m_gr*mgVOF;

           }

      end_c_loop (c,t)

   }

}
```

/*The mass_source and mesh_refine functions are unsteady terms that are used to smear the source terms over a constant distance regardless of the size of the time step. */

```
DEFINE_UDS_UNSTEADY(mass_source,c,t,i,apu,su)

 {

   real physical_dt, vol, rho, phi_old;
```

```
    physical_dt = 4e-9;

    vol = C_VOLUME(c,t);

    rho = C_R(c,t);

    *apu = -rho*vol / physical_dt;/*implicit part*/

    phi_old = C_UDSI(c,t,1);

    *su = rho*vol*phi_old/physical_dt;/*explicit part*/

  }



DEFINE_UDS_UNSTEADY(mesh_refine,c,t,i,apu,su)

{

    real physical_dt, vol, rho, phi_old;

    physical_dt = 4e-9;

    vol = C_VOLUME(c,t);

    rho = C_R(c,t);

    *apu = -rho*vol / physical_dt;/*implicit part*/

    phi_old = C_UDSI(c,t,3);

    *su = rho*vol*phi_old/physical_dt;/*explicit part*/

  }
```

/*The diffuse function takes the mass source term, which has been smeared by the Ansys Fluent solver, and bounds it so that mass transfer will only occur within refined cells*/

```
DEFINE_ADJUST(diffuse, domain)

{

  Thread *t;

  cell_t c;
```

```
domain = Get_Domain(domain_ID);


/* Fill UDS with the variable. */

thread_loop_c (t,domain)

  {


    begin_c_loop (c,t)

     {

                  if (C_UDSI(c,t,4)>=1e5)

                  {

                         C_UDSI(c,t,5) = C_UDSI_M1(c,t,2);

                  }

                  if (C_UDSI(c,t,4)<1e5 || C_UDSI_M1(c,t,2)<0)

                  {

                         C_UDSI(c,t,5) = 0;

                  }

     }

    end_c_loop (c,t)

  }

}


/* The norm_fct function creates normalisation factors by integrating the initial source term, and then

integrating the bounded and smeared source terms to ensure the conservation of total mass transfer*/


DEFINE_ADJUST(norm_fct, domain)
```

```
{

        Thread *t;

        cell_t c;

        NVbot=0.0;

    NVLtop=0.0;

    NLbot=0.0;

        NL=0.0;

        NV=0.0;


        domain = Get_Domain(domain_ID);


        thread_loop_c (t,domain)
    {

      begin_c_loop (c,t)

        {

                        NVLtop += C_UDSI(c,t,1)*C_VOLUME(c,t);

          if (C_VOF(c,t) <= VCutV)

            {

            NVbot += (1-C_VOF(c,t))*C_UDSI(c,t,5)*C_VOLUME(c,t);

            }

          if (C_VOF(c,t) >= (VcutL))

            {

            NLbot += C_VOF(c,t)*C_UDSI(c,t,5)*C_VOLUME(c,t);

            }

        }

          end_c_loop (c,t)
```

113

```
        }

        if (PRF_GRSUM1(NVbot) !=0 && PRF_GRSUM1(NLbot) !=0)

        {

                NV=PRF_GRSUM1(NVLtop)/PRF_GRSUM1(NVbot);

                NL=PRF_GRSUM1(NVLtop)/PRF_GRSUM1(NLbot);

        }


}
```

/*The vap_src function uses the smeared and bounded source terms and the normalisation factor to explicitly create a source term for the vapour domain*/

```
DEFINE_SOURCE(vap_src,c,sec_th,dS,eqn)

{

        mass_v=0;

        Thread *mix_th, *pri_th;

        mix_th = THREAD_SUPER_THREAD(sec_th);

        pri_th = THREAD_SUB_THREAD(mix_th,0);

        if (C_VOF(c,pri_th)<=VCutV)

        {

                mass_v = NV*(1-C_VOF(c,pri_th))*C_UDSI(c,mix_th,5);/*explicit part*/

                dS[eqn] = 0;/*implicit part*/

        }

        else if (C_VOF(c,pri_th)>VCutV)

        {

                mass_v = 0;/*explicit part*/

                dS[eqn] = 0;/*implicit part*/
```

```
        }

        C_UDSI(c,mix_th,6)=mass_v;

        return mass_v;

}

/*The liq_src function uses the smeared and bounded source terms and the normalisation factor to
explicitly create a source term for the liquid domain*/


DEFINE_SOURCE(liq_src,c,pri_th,dS,eqn)

{

        mass_l=0;

        Thread *mix_th, *sec_th;

        mix_th = THREAD_SUPER_THREAD(pri_th);

        if (C_VOF(c,pri_th)>=(VcutL))

        {

                mass_l = -NL*C_VOF(c,pri_th)*C_UDSI(c,mix_th,5);/*explicit part*/

                dS[eqn] = 0.0;/*implicit part*/

        }

        else if (C_VOF(c,pri_th)<(VcutL))

        {

                mass_l = 0;/*explicit part*/

                dS[eqn] = 0;/*implicit part*/

        }

        C_UDSI(c,mix_th,7)=mass_l;

        return mass_l;

}
```

/*The enrg_src funtction uses the initial source term, its gradient and the liquid and vapour source terms, multiplied by their specific heats to implicitly create a source term for the mixture domain*/

DEFINE_SOURCE(enrg_src,c,t,dS,eqn)

{

      real enrg_s=0;

   enrg_s = -C_UDSI(c,t,1)*h+C_UDSI(c,t,7)*cpl*(C_T(c,t)-298.15)+C_UDSI(c,t,6)*cpg*(C_T(c,t)-298.15);/*explicit part*/

      dS[eqn] = -C_UDSI(c,t,9)*h+C_UDSI(c,t,7)*cpl+C_UDSI(c,t,6)*cpg;/*implicit part*/

      C_UDSI(c,t,8)=enrg_s;

      return enrg_s;

}